SPECTRAL RADIATIVE PROPERTIES AND RADIATION HEAT TRANSFER OF BAUXITE AND SiO_2 PARTICLES FOR SOLAR THERMAL APPLICATIONS

A Dissertation
Presented to
The Academic Faculty

by

Chuyang Chen

In Partial Fulfillment
Of the Requirements for the Degree
Doctor of Philosophy in the
G. W. Woodruff School of Mechanical Engineering

Georgia Institute of Technology
May 2022

SPECTRAL RADIATIVE PROPERTIES AND RADIATION HEAT TRANSFER OF BAUXITE AND SiO_2 PARTICLES FOR SOLAR THERMAL APPLICATIONS

Approved by:

Dr. Zhuomin Zhang, Co-advisor
George W. Woodroff School of
Mechanical Engineering
Georgia Institute of Technology

Dr. Andrew F. Peterson
School of Electrical and Computer
Engineering
Georgia Institute of Technology

Dr. Peter G. Loutzenhiser, Co-advisor
George W. Woodroff School of
Mechanical Engineering
Georgia Institute of Technology

Dr. Clifford K. Ho
Sandia National Laboratories

Dr. Devesh Ranjan
George W. Woodroff School of
Mechanical Engineering
Georgia Institute of Technology

Date Approved: April 19, 2022

To my parents

ACKNOWLEDGEMENTS

I would like to take this opportunity to express my sincere gratitude to my advisors Dr. Zhuomin Zhang and Dr. Peter Loutzenhiser. I would never become the person today and this dissertation would not be possible without their support. Throughout the five years, Dr. Zhang has always been able to help me find the right way to make improvements. It was his expertise as a scientist, and dedication as an educator that brought the enlightenment to our daily conversations. His character will always be the beacon that guides me through hardships and challenges. I would also like to express my heartful thanks to Dr. Peter Loutzenhiser, who not only introduced me to the field of solar technology, but also paved the way for me to embrace scholarly conversations with many leaders worldwide. Because of this, I was able to further strengthen my research skills, build confidence, and strive for more. I am also grateful for Dr. Devesh Ranjan, Dr. Andrew Peterson, and Dr. Clifford Ho, for serving in my dissertation reading committee and sharing their knowledge that broaden my horizon. I'd like to thank Department of Energy for supporting Concentrated Solar Power programs, and National Science Foundation for supporting Thermal Transport Processes programs.

My appreciation extends to the current and formal members of Nanoscale Thermal Radiation Laboratory and Solar Fuels and Technology Lab. I would like to thank Dr. Peiyan Yang for the many constructive conversations, sharing of graduate life, and his help during my transition first year; Dr. Bo Zhao for his unique ideas and interpretation of science and technology; Dr. Zhaolong Wang, Dr. Eric Tervo, Dr. Xiaohu Wu, Dr. Shiquan Shan, Dr. Dudong Feng, Dr. Andrew Schrader, Shin Young Jeong, Chiyu Yang, Presten Bohm, Malavika Bagepalli, Tyler Farr, Nhu Nguen, and Shaspreet Singh. My friends and

colleges, professors from my graduate courses, have all offered their helps and suggestions to enrich my graduate experience.

Finally, I would like to thank my parents for their unconditional love and support. Knowing that they will always have my back gives me endless strength to go full speed ahead, with passion, curiosity, and perseverance.

TABLE OF CONTENTS

LIST OF TABLES

LIST OF FIGURES

NOMENCLATURE

a_λ	absorption coefficient, m^{-1}
C	cross-sectional area, m^2
$C_{abs,\lambda}$	absorption cross section, m^2
$C_{sca,\lambda}$	scattering cross section, m^2
d	effective particle diameter, m
E	emissive power, W/m^2
E_λ	spectral emissive power, $W/m^2 \cdot \mu m$
F_C	correction factor
g	asymmetry factor
G_λ	spectral irradiance, $W/m^2 \cdot \mu m$
I	total intensity, $W/m^2 \cdot sr$
$I_{b,\lambda}$	blackbody spectral intensity, $W/m^2 \cdot \mu m \cdot sr$
l	number of type 2 particles
L	particle bed thickness, m
L^*	specific thickness
m	number of type 1 particles
n	real part of the refractive index; total number of particles
$\tilde{n}$	complex refractive index
N	particle number density, $1/m^3$; number of oscillators or constituents

$Q_{\text{abs},\lambda}$ absorption efficiency factor

$Q_{\text{sca},\lambda}$ scattering efficiency factor

r mixing ratio

$\mathbf{r}_0$ center of sphere location based on FCC

$\mathbf{r}_c$ center of sphere location after randomization

R directional-hemispherical reflectance

$\mathbf{s}$ location vector of a photon bundle

S specularity; measured emission signal, arbitrary units

S_0 measured ambient noise signal, arbitrary units

S_j oscillator strength

T directional-hemispherical transmittance; temperature, K

T_{cru} temperature of the crucible, K

$\mathbf{v}$ direction vector of a photon bundle

V total volume of a unit cell, m^3

V_{p} total volume of particles, m^3

Greek symbols

α absorptance

γ half of the clearance for particles between layers, m

γ_j damping coefficient, cm^{-1}

δ step size of a photon bundle, m

ε emittance

$\tilde{\varepsilon}$ complex dielectric function (relative electric permittivity)

ε_∞ high-frequency constant

ζ intercept distance, m

κ imaginary part of the refractive index, or absorption index

λ wavelength, μm

λ_{Ch} Christiansen wavelength, μm

ξ side length of a unit cell, m

ρ reflectivity at the surface

σ the Stefan-Boltzmann constant, 5.670×10^{-8} W/m^2·K^4

σ_λ (isotropic or reduced) scattering coefficient, m^{-1}

$\sigma_{\lambda,\mathrm{true}}$ (true) scattering coefficient, m^{-1}

τ internal transmissivity

τ_d optical thickness over a particle diameter $\tau_d = 4\pi\kappa d / \lambda$

ϕ volume fraction

ϕ_v particle volume fraction

χ uniformly distributed random number between 0 and 1

ω scattering albedo; frequency, cm^{-1}

ω_j resonance frequency, cm^{-1}

Subscripts

b	blackbody
BB	blackbody source
bw	particle bed combined with the backside window
eff	effective
E	extraordinary
h	host
i	incidence
j	index for individual constituent
O	ordinary
p	particle bed
s	sample (particle bed with window)
w	window
λ	spectral

ACRONYMS

AD	adding-doubling
CSP	concentrated solar power
DTGS	deuterated triglycine sulfate
EMA	effective medium approximation
FCC	face-centered cubic
FTIR	Fourier transfer infrared spectrometer
HG	Henyey-Greestein
IAD	inverse adding-doubling
MCT	mercury cadmium telluride, HgCdTe
MG	Maxwell-Garnett
MIR	mid-infrared
NIR	near-infrared
PTFE	polytetrafluoroethylene
RMSD	root means square deviation
RTE	radiative transfer equation
TES	thermal energy storage
UV	ultraviolet
VIS	visible

SUMMARY

This dissertation investigates the spectral radiative properties of various particles used for concentrated solar power by performing the four research tasks. (1) Measurement of radiative properties of particle beds made from a selection of bauxite particles with various particle sizes and distributions, and model the dielectric function of particles using effective medium theory; (2) Measurement of radiative properties of particle beds made from silica at various sizes, and investigation of the significance of dependent and independent scattering by comparing absorption and scattering coefficients; (3) Development of a high-temperature emissometer, measurement of the temperature-dependent emittance of bauxite and silica particle beds, and investigation of infrared phonon modes that change with temperature; and (4) Modeling of the radiative properties of particle mixture, and investigation of the effects of mixing ratio, volume fraction, and spectral dependent refractive index.

Measured spectral radiative properties and the understanding of the radiation transfer in bauxite and silica particle beds are gained through this experimental and theoretical research. A new instrument is developed to facilitate further investigation. The findings of this thesis address current knowledge gaps to characterize radiative properties of polydisperse particle beds more accurately over a wide range of temperatures. The findings can also lead to improved estimations of particle heat transfer and designs of particle-based concentrating solar thermal technologies.

CHAPTER 1

INTRODUCTION

1.1 Motivation

A path toward carbon-neutral society with suitable decarbonization strategies aiming to limit global warming below 2 °C in the 21st century is paved by extensive research on clean renewable energies that facilitate grid-scale power generation competitive to fossil fuel [1]. These alternative energy technologies include but not limit to wind energy, tidal energy, biomass, geothermal energy, hydropower, and solar energy. Rapid developments have been made in solar technology especially in photovoltaics owning to the growth of semiconductor industry and the maturity of conceptualization in device design [2]. The electricity generation based on solar-to-thermal conversion, although being conceptually well accepted as another means for clean energy production from solar energy, is yet to be largely implemented global wise. Therefore, there is a great potential for rapid development.

The current state of solar-to-thermal technology at residential scale is largely dependent on the absorption of natural sunlight by highly absorbing surfaces (black paint, etc.) without further complication (light concentration or energy storage). Examples include rooftop solar water heater and solar distillation. The common drawback is the dependence on daylight exposure and the energy production is relatively small. Developments are made at industrial scale to overcome these challenges by storing solar energy in the form of heat and utilizing concentrated sunlight. Harnessing sunlight by means of concentrated solar radiation and thermal energy storage facilitates advancements

in both the investigation of solar thermal energy storage (TES) materials and the understanding of pertinent energy transfer processes [3-7].

Concentrated solar power (CSP) plants operate at a temperature range of 700 – 1000 °C. The concentration ratio is typically greater than 1000 suns and up to 2000 suns (where 1 sun = 1 kW/m^2) due to the use of heliostats field [6], which consists of highly reflective planar mirrors that redirect sunlight to a central tower. At the top of the central tower, light absorption occurs when TES materials are used. Due to excessive heat flux, different types of TES materials are used. For example: ceramics have high temperature endurance to store the thermal energy in the form of sensible heat; molten salts experience phase change at elevated temperatures and store solar energy in the form of latent; calcium-based perovskites provide thermochemical energy storage cycles via reduction/oxidation processes [3-5, 8-13]. Most CSP plants with grid-scale energy production currently utilize molten salts as the TES material and the nitrate salts in a two-tank configuration is shown to have a working temperature up to 850 °C [6, 8]. However, the associated corrosion effect creates challenges for cost effective operation and maintenance. Alternatively, ceramic particles such as bauxite and SiO_2 do not undergo phase change at high temperatures and are chemically stable, hence are investigated as candidates for newer particle based CSP plants.

Particles made from ceramics are placed in a particle receiver located at the top of central tower, where they are allowed to free fall through an aperture subjected to direct impingement of concentrated solar radiation. The conversion from solar to thermal energy takes place within such granular flow or particle curtain [14-16]. The receiver is designed such that a cavity is placed behind the curtain for minimizing radiative loss. The

temperature-dependent (at room and high temperatures) spectral radiative properties of the particles play an instrumental role in absorbing the solar radiation, and characterizing the particle-to-particle, and particle-to-wall radiative heat exchange. Particles at the focal of concentrated sunlight have a temperature near 1000 °C (1273 K). This corresponds to a wavelength of $\lambda \approx 2$ μm with peak thermal emission according to Wein's displacement law. For particles near room temperature (300 K), the corresponding peak wavelength is $\lambda \approx 10$ μm. However, the spectral dependence is often simplified with gray surface assumption and the temperature independence is assumed when modeling for conjugate heat transfer processes in a particle receiver. For large scale energy production such as a CSP plant using particle receivers, incorrect assumption on the radiative properties may lead to large deviation in the predicted receiver performance.

In the solar-to-thermal conversion process, the light-particle interaction undergoes complex mechanisms of absorption and scattering that impact the energy absorbing efficiency. They also play an important role in the overall heat transfer processes for numerous aerospace and industrial applications [17-24]. These mechanisms are sensitive to the receiver design parameters, such as the thickness of the curtain, particle volume fraction and diameter, and mixing condition when different types of particles present. In general, these applications represent a type of particulate media, where phase discontinuity (solid, gas, liquid) complicates light scattering mechanisms. When treated as an effective continuous medium, light propagation could be described by the integro-differential equation known as the radiative transfer equation (RTE). Previous independent scattering theory predicts that the radiative properties for particulate media can be modeled from superposition of individual particle's radiative properties such as absorption and scattering

coefficients. It is important to investigate the accuracy of such prediction when applied to particle beds that may have polydisperse and mixing condition. On the other hand, when treated as a discontinuous medium, the light propagation is commonly modeled with ray tracing in the geometric optics regime for large particles. Due to excessive computational load associated with modeling in a 3-dimentional domain, ray-tracing algorithms in the field of radiative heat transfer often adapt oversimplified modeling condition such as monodispersing particles and ignoring mixing effect. It is important to seek for advanced modeling scheme with computational efficiency and accurate results.

1.2 Objective

The objective of this dissertation is to experimentally investigate the spectral radiative properties of selected particles in the form of particle beds and perform numerical simulation of radiative heat transfer processes. Bauxite and polycrystalline silica particles are used to form densely packed beds and measured for radiative properties. Interpretations based on qualitative approximation and quantitative comparison are made to elucidate the effect of particle composition, size, dependent scattering, and temperature on radiative properties. A high-temperature emissometer is developed to measure the temperature dependent emittance. A ray-tracing algorithm is developed based on Monte Carlo method to investigate the absorption and scattering mechanisms of radiation transfer in particle beds and to study the impact of particle volume fraction and mixing effect on the radiative properties. The remaining of this dissertation is organized as follows:

- Chapter 2 presents a literature review and theoretical foundation for characterizing the radiative properties of particle beds, radiative heat transfer in

particulate media, obtaining dielectric functions of pure and composite materials, and a discrete-scale Monte Carlo ray tracing algorithm.

- Chapter 3 presents an experimental study of selected bauxite particles to examine the particle size effect and the impact of composition on the measured spectral absorptance using both net radiation and effective medium theory.
- Chapter 4 investigates the relationship between the independent and dependent scattering when polycrystalline silica particle beds are measured for radiative properties at different particle sizes and bed thicknesses.
- Chapter 5 presents a newly developed high-temperature emissometer that is used for measuring the temperature-dependent emittance of bauxite and silica particle beds and analyzing the temperature effect on the optical phonon in the infrared wavelength region.
- Chapter 6 gives assessments to the impact of particle mixture by modeling radiative properties with an advanced Monte Carlo ray tracing algorithm. A parametric study is performed to highlight the effects of mixing ratio, particle volume fraction, and complex refractive index on radiative properties.

Finally, the major findings are summarized and concluded in Chapter 7 with a look towards potential research opportunities and topics for future work.

CHAPTER 2

LITERATURE REVIEW AND THEORETICAL FOUNDATION

The spectral radiative properties of particles and particle beds (or curtain) affect the thermal performance of the particle receiver. It is important to investigate relationships between the particle and the bed such as: the condition that single particle radiative properties can approximate the properties of the bed; the significance of designing parameters including particle volume fraction, mixing ratio, and spectral dependent refractive index. The absorption and scattering mechanisms in such a nonhomogeneous medium differ from the traditional understanding of radiation transfer in homogeneous media.

This chapter gives a literature review of (1) the radiative properties of ceramic particles used for CSP applications; (2) physical models and numerical frameworks pertinent to the analysis of experimental results and simulation of thermal radiative transfer in particle beds. Both the importance of existing experimental results and the validity of classical models are discussed with a focus of addressing the knowledge gaps and potential improvements.

2.1 Radiative Properties of Particle Beds

2.1.1 Bauxite particles

Ceramic particles made from bauxite were previously used in applications such as abrasives, filtration, and mining support. Bauxite is a natural occurring, abundant mineral resource. It primarily consists of Al_2O_3, with a weight fraction over 0.75, along with other

oxides such as SiO_2, Fe_2O_3, and TiO_2 [22, 25]. There is also a small number of other oxides such as mullite ($3Al_2O_3 \cdot 2SiO_2$) [25]. It was found that these materials possess high solar absorptance and thermal capacitance and are chemically stable for temperatures greater than 1000 °C [10], making them ideal candidates for use in solar particle receivers [14-16]. Implementation of bauxite particles in a prototype CSP plant demonstrated a receiver thermal efficiency over 80% [15]. The solar weighted absorptance was also measured to be over 0.9 [14].

Characterization of the thermal and radiative properties of the granular flow formed by the falling particles has been previously carried out [22]. In a comprehensive heat transfer analysis of the falling particle receiver, spectral radiative properties of particles must be included [13, 26, 27]. For a blackbody at 800 °C, the peak intensity according to Wein's displacement law is at a wavelength of $\lambda \approx 2.8$ μm and shifts toward $\lambda \approx 10$ μm when approaching ambient temperature (27 °C or 300 K) [28]. Previous studies of spectral radiative properties have mainly focused on ultraviolet (UV) to near infrared (NIR) ($\lambda <$ 2.0 μm) with limited resolution toward mid-infrared (MIR) region [14, 25]. There is a growing need for a spectrally inclusive experimentation on the radiative properties of bauxite particles for different particle sizes and compositions.

Relatively few experimental works have been performed to examine and quantify the radiative properties of particles or particle beds at elevated temperatures. The total emittance has often been obtained by spectral integration based on the spectral reflectance measured at room temperature [14, 25, 29, 30]. In most of the modeling approaches, a constant emittance was assigned to the particles. Such assumption may potentially result in unrealistic predictions that deviate from experiments when modeling radiative heat

transfer of particle receivers at elevated temperatures [31-33]. Typically, either a direct or an indirect method is used for measuring the spectral emittance of films and bulk materials [34-39]. However, there are daunting challenges for directly measuring the high-temperature emittance of particles or particle beds due to their nonhomogeneous structure, which could result in a large temperature gradient within the measured layer thickness [40-43]. Some researchers have investigated the directional emittance of nonisothermal and isothermal particle beds by considering the relations between the directional emittance and the temperature gradient, porosity, and particle face temperature [44-46]. Wald and Salisbury [47] measured the directional emittance of the powdered quartz considering the exitance angle, particle size, and packing condition. A non-contact measurement technique based on blackbody distribution and directional reflectance was demonstrated by Meneses et al. [48] and used to study thin films and rough surfaces. When the particle diameter is of several millimeters, direct measurement of the total emittance and absorption function of individual particles (Al_2O_3 and SiC) has also been performed [49]. There is an urgent need for direct measurements of the spectral emittance of solid particles at elevated temperatures and in the mid-infrared region.

2.1.2 Polydispersed SiO_2 Particles and Particle Mixture

Most studies of the radiative properties of SiO_2 particle beds are based on numerical simulations and comparisons between different models [50-55]. Experimental investigations have been limited, especially for particle sizes much greater than the wavelengths of interest. Brewster and Tien [56] and Yamada et al. [57] measured light scattering at two visible wavelengths for polymer particle bed with particle diameters of

80 nm, 2 μm, and 11 μm with varying volume fractions. Agarwal and Mengüç [58] gave a summary of earlier experimental researches on light propagation in participating media and performed an extensive theoretical and experimental study of the angle-resolved scattering by mono- and poly-dispersions of suspended particles. Kamiuto et al. [59, 60] measured the extinction coefficient, albedo, and phase function of packed spherical particle beds with both opaque and transparent particles of diameters near 1 mm. Their results provide experimental evidence of dependent scattering due to volume scattering effect for large spheres in the geometric optics regime. A number of studies are based on the inverse solutions to retrieve the absorption and scattering coefficients and/or phase function from experimental measurements for porous ceramics [20, 61-64], open-cell foam insulations [65, 66], aerogels [21], bubbles in fused quartz glass [67], sintered porous plastics [68, 69], and turbid media or biological skins and tissues [70, 71]. The inverse methods include the simple two-flux model, three-flux model, the discrete-ordinates method (DOM), the adding–doubling (AD) method, among others [28, 70, 72, 73]. The experimental measurements that are most frequently used are the spectral, directional–hemispherical reflectance and transmittance of the specified media in a flat plate or disk geometry [64, 69]. Researchers have also used collimated transmittance and/or angle-resolved scattering properties [56, 58, 68, 74-76].

Radiative properties of particle beds with configurations that facilitate practical applications with polydispersed, mixture types, and irregular shapes have also been investigated [77-80]. Lipiński et al. [77] and Jäger et al. [78] measured the transmittance of polydispersed packed beds with a mixture of SiO_2, ZnO, and C particles of different sizes and volume fractions at a wavelength of 632.8 nm. As more ZnO and C contents are

added into the SiO_2 bed, the measured transmittance reduces rapidly, and the absorption is expected to increase. To determine the scattering phase function, Coray et al [79] and Marti et al. [80] performed spectral, angle-resolved measurements of packed beds of ZnO particles and SiC particles, respectively. The effect of hosting medium was examined by embedding the SiC particles in an epoxy resin.

Further investigation of the radiative properties of polydispersed particle beds is necessary, especially in the semitransparent region and at mid-infrared wavelengths. Outstanding questions remain as to whether simplified models are adequate to explain the measured spectral, directional–hemispherical transmittance and reflectance, whether isotropic scattering model can be used in the continuous-scale modeling, and whether it is appropriate to use spherical particles with an average diameter to represent the packed bed with irregularly shaped particles for prediction of the hemispherical radiative properties. The impact of dependent scattering on the radiative properties for semitransparent particles and the influence of impurity on the absorption need to be further analyzed based on experimental findings.

2.2 Radiation Transfer in Particulate Media

Radiative properties of a bulk material strictly follow the spectral dependent Fresnel reflection and refraction, and the refractive index. For semitransparent media and simple geometry (*i.e.*, slab), the reflectance can be decomposed into reflected rays that form a geometric series due to multiple reflections at the interface. In a particulate media, the overall radiative properties of the media are different from that of the particles. Thus, it is

necessary to evaluate the significance of dependent scattering and identify suitable regions where independent approach gives satisfactory approximation.

2.2.1 Radiative Transfer Equation

For continuous media, including dispersed media containing small particles, an energy balance over an infinitesimal control volume leads to the radiative transfer equation that governs the light transport without considering polarization state of the wave. At the steady state, the spectral intensity, *I*, can be written as:

$$\frac{\mathrm{d}I_\lambda(\hat{\mathbf{s}})}{\mathrm{d}s} = a_\lambda I_{\lambda\mathrm{b}} - (a_\lambda + \sigma_{\lambda,\mathrm{true}})I_\lambda + \sigma_{\lambda,\mathrm{true}}\int_{4\pi} I_\lambda(\hat{\mathbf{s}}_\mathrm{i})\Phi_\lambda(\hat{\mathbf{s}}_\mathrm{i},\hat{\mathbf{s}})\mathrm{d}\Omega_\mathrm{i} \tag{2.1}$$

where a_λ and $\sigma_{\lambda,\mathrm{true}}$ are the absorption and true scattering coefficients (to be distinguished from the reduced scattering coefficient), respectively. The quantity $I_{\lambda\mathrm{b}}$ is the blackbody intensity that can be described by Planck's law. Φ_λ is the scattering phase function, which essentially describes the probability of an incident ray, $\hat{\mathbf{s}}_\mathrm{i}$, that scatters into the direction $\hat{\mathbf{s}}$ (in-scattering). The integration of Φ_λ over all angles is 1, sharing the feature of a standard probability density function. Hence, the energy balance considers the augmentation of the intensity by thermal emission ($a_\lambda I_{\lambda\mathrm{b}}$), and in-scattering contribution, as well as the attenuation by absorption and out-scattering ($a_\lambda + \sigma_{\lambda,\mathrm{true}}$).

With knowledge of absorption and scattering properties, and under specific assumptions, the RTE can be solved using simplified solution models such as a diffusion approximation [81], two-flux model [28, 82-84], discrete ordinates method [28, 85], Forward adding-doubling (AD) method [86, 87], and Monte Carlo method [51-53, 55, 88, 89]. The last two methods are used in this dissertation. In this dissertation, the AD method

is considered to numerically solve the RTE and obtain the radiative properties of the particulate media, where the scattering phase function is also determined the via Monte Carlo method. Detailed description is found in Chapter 4.

2.2.2 Dependent and Independent Scattering by Particles

The physical understanding of a_λ and $\sigma_{\lambda,\text{true}}$ facilitates the recognition of scatterers in a dispersed medium, and it is caused by the refractive index mismatch between the suspended particles in a medium that can be fully transparent (with no attenuation) or lossy (with little attenuation).

For relatively small particles in a dilute suspension, the continuous-scale radiative transfer equation is often applied to the participating medium (involving absorption, scattering, and emission) without considering inhomogeneity [28, 85]. a_λ and $\sigma_{\lambda,\text{true}}$ of individual particles (*i.e.*, point scatters) are captured by the Mie theory, considering diffraction effects and then superimposed to obtain the properties of the medium according to the independent scattering theory [58, 72, 73]. When the particles are placed in close proximity, dependent scattering due to wave interference and near-field effects becomes important such that the simple superposition approach breaks down [56, 57, 90].

Particle beds and porous media with particle/pore sizes from several tens to hundreds of micrometers are of great significance to contemporary technologies [50, 67, 73, 91-95]. For relatively large particles or pores with dimensions much greater than the visible or infrared wavelengths, geometric optics is valid, and the radiative properties can be modeled using the ray-tracing approach. The discrete-scale Monte Carlo method based on a stochastic sampling process is commonly applied to trace a large number of photon

bundles (considering reflection/refraction at the interface and absorption inside an individual phase) to obtain the radiative properties of particulate media [51, 88, 96]. More complicated models have been developed to include absorption by the hosting matrix (or semitransparent medium) [52-55, 89]. The RTE is frequently applied to model the radiative properties by treating the particulate media as homogeneous with effective absorption and scattering properties.

For spherical particles, the absorption and scattering cross sections as well as the scattering phase function of a single particle are commonly estimated by a Monte Carlo ray-tracing method. Then, the absorption and reduced scattering coefficients of the particle beds are calculated using the independent scattering theory, similar to the situation with small particles [97, 98]. However, even in the geometric-optics regime, multiple scattering or volume scattering due to the geometric proximity effect can also give rise to strong dependent scattering [51, 59, 99-101]. Some scaling factors have been suggested for the extinction coefficient or scattering albedo of particle beds with opaque spheres; however, no correlations or a clear trend exist for semitransparent spheres [59, 99, 100]. Hence, spatial or volume averaging techniques are often necessary to account for the dependent scattering effect for dense and complex structures [97, 98, 102-105]. Researchers have also used computer-assisted x-ray tomography to obtain 3D images of the microstructures in order to retrieve the effective absorption and scattering properties of an element volume [50, 103].

The independent scattering approach conveniently provide radiative properties of particulate media when the dependent scattering effect is negligible [14, 25, 30]. For

particles of sizes much greater than the wavelength, the effective a_λ and $\sigma_{\lambda,\text{true}}$ follows the simple summation rule:

$$a_\lambda = \frac{1}{V}\sum_{j=1}^{n} C_{\text{abs},\lambda,j} = \frac{n}{V} C_{\text{abs},\lambda} = N C_{\text{abs},\lambda} \tag{2.2}$$

$$\sigma_{\lambda,\text{true}} = \frac{1}{V}\sum_{j=1}^{n} C_{\text{sca},\lambda,j} = \frac{n}{V} C_{\text{sca},\lambda} = N C_{\text{sca},\lambda} \tag{2.3}$$

where n is the number of particles present in a control volume V . The particles occupy the volume fraction of ϕ_v and $N = n/V = 6\phi_v/(\pi d^3)$ is the number density. $C_{\text{abs},\lambda}$ and $C_{\text{sca},\lambda}$ are the absorption and scattering cross sections of the particle, respectively. They can be obtained from measurements of the spectral reflectance and transmittance [76] or performing ray-tracing simulation on a particle. It is assumed that the particles in the medium equally contribute to the absorption and scattering of light.

When there are dissimilar particles, the summation of cross sections of particles is slightly adapted to account for the mixing effect. The derivation for a mixture containing two types of particles is shown as:

$$a_\lambda = \frac{1}{V}\sum_{j=1}^{n} C_{\text{abs},\lambda,j} = \frac{1}{V}\sum_{j=1}^{m} C_{1,\text{abs},\lambda,j} + \frac{1}{V}\sum_{j=1}^{l} C_{2,\text{abs},\lambda,j} \tag{2.4}$$

$$\sigma_{\lambda,\text{true}} = \frac{1}{V}\sum_{j=1}^{n} C_{\text{sca},\lambda,j} = \frac{1}{V}\sum_{j=1}^{m} C_{1,\text{sca},\lambda,j} + \frac{1}{V}\sum_{j=1}^{l} C_{2,\text{sca},\lambda,j} \tag{2.5}$$

where the subscripts 1 and 2 denote particle type 1 and 2, m and l are the number of particles for type 1 and 2, respectively, and $m + l = n$. Simplification to the above equations leads to the final form:

$$a_\lambda = NrC_{1,\text{abs},\lambda} + N(1-r)C_{2,\text{abs},\lambda} \tag{2.6}$$

$$\sigma_{\lambda,\text{true}} = NrC_{1,\text{sca},\lambda} + N(1-r)C_{2,\text{sca},\lambda} \tag{2.7}$$

where $r = m / n$ is the mixing ratio defined by the type 1 particle.

2.2.3 Simplification by Net Radiation Method

For non-scattering media with smooth surface, the directional-hemispherical radiative properties can be deduced by means of geometric optics when the thickness is much greater than the wavelength. Multiple reflections are summed to form geometric series, and the directional-hemispherical reflectance and transmittance can be expressed, respectively, as:

$$R_\lambda = \rho_\lambda + \frac{\rho_\lambda \left(1-\rho_\lambda\right)^2 \tau_\lambda^2}{1-\rho_\lambda^2 \tau_\lambda^2} \tag{2.8}$$

and

$$T_\lambda = \frac{\left(1-\rho_\lambda\right)^2 \tau_\lambda^2}{1-\rho_\lambda^2 \tau_\lambda^2} \tag{2.9}$$

where ρ_λ is the interface reflectivity between air and a semi-infinite slab, and τ_λ is the internal transmissivity that can be expressed as $\tau_\lambda = \exp(-a_\lambda L)$ at normal incidence. a_λ is the absorption coefficient and κ is the absorption index or the imaginary part of the refractive index. The complex refractive index is expressed as $\tilde{n} = n + \mathrm{i}\kappa$. The real part and imaginary part of the complex refractive index are the optical constants, which are functions of wavelength though the subscript λ is omitted for brevity [97, 106]. The surface reflectivity for a smooth interface for incidence from air (or vacuum) can be calculated from Fresnel's coefficients and is expressed in the following at normal incidence

$$\rho_\lambda = \frac{(n-1)^2 + \kappa^2}{(n+1)^2 + \kappa^2} \tag{2.10}$$

Note that the incidence is assumed normal (0° incidence angle) for the above equations, which are simplified from the general form that can be found in Zhang [106]. The measured radiative properties in this thesis have an incidence angle between 7° and 8°. At such small angles of incidence, the values of ρ_λ and τ_λ change little from those with normal incidence angles.

2.3 Dielectric Function of Crystalline and Composite Materials

The complex refractive index $\tilde{n} = (n + \mathrm{i}\kappa)^2$ is an intrinsic optical property of materials. The optical constants are spectrally dependent and are sensitive to bandgap transition, optical phonon excitation, interband transition, and electronic contribution [106]. It is further complicated when dealing with composites of different oxides. Individual contributions are reflected to the effective optical properties of the bulk material. When there are multiple phonon modes present, they contribute to the bulk property collectively.

2.3.1 Lorentz Model

The n and κ used in Eq. (2.10) are a function of wavelength and describe the dispersion of electromagnetic waves when propagating in a medium. For thin film samples, the measured reflectance can be fitted with the Lorentz oscillator model to determine the oscillator parameters [64, 107, 108]. The general expression of the dielectric function, $\tilde{\varepsilon} = \tilde{n}^2 = (n + \mathrm{i}\kappa)^2$, can be expressed as:

$$\tilde{\varepsilon}(\omega) = \varepsilon_\infty + \sum_{j=1}^{N} \frac{S_j \omega_j^2}{\omega_j^2 - i\gamma_j \omega - \omega^2} \tag{2.11}$$

where ε_∞ is a high-frequency constant, and S_j, ω_j, and γ_j are the oscillator strength, resonance frequency, and damping coefficient of the j^{th} oscillator in a total of N oscillators, respectively. The Lorenz model is an implementation of the equation of motion for lattice vibration considering bonded electrons [106].

2.3.2 Effective Medium Theory

For composite materials such as bauxite ceramics, the dielectric function is sensitive to the individual components, namely metal oxides, that contribute to the overall dielectric function. It is insightful to approximate the dielectric function by homogenizing the composite and consider the contribution of constituents using volume fractions.

Maxwell-Garnett (MG) theory [109, 110] considers one constituent as the host matrix, then the effective dielectric function can be written as:

$$\frac{\tilde{\varepsilon}_{\text{eff}} - \tilde{\varepsilon}_1}{\tilde{\varepsilon}_{\text{eff}} + 2\tilde{\varepsilon}_1} = \sum_{j=2}^{N} \phi_j \frac{\tilde{\varepsilon}_j - \tilde{\varepsilon}_1}{\tilde{\varepsilon}_j + 2\tilde{\varepsilon}_1} \tag{2.12}$$

where $\tilde{\varepsilon}_{\text{h}}$ is the dielectric function of the host matrix, while the remaining constituents are considered as fillers that are embedded in the host matrix. $\tilde{\varepsilon}_j$ is the dielectric function and ϕ_j is the volume fraction of the jth constituent. In practice, one may choose $j = 1$ as the host material $\tilde{\varepsilon}_{\text{h}} = \tilde{\varepsilon}_1$ with the highest volume fraction ϕ_1. If the shape of all the fillers is assumed to be spherical, the effective dielectric function of the composite $\tilde{\varepsilon}_{\text{eff}}$ can be related to the dielectric function and volume fraction of the individual constituents by the

explicit relation [111]. Note that $\phi_1 + \phi_2 + ... + \phi_N = 1$. Eq. (2.12) can be solved explicitly to obtain $\tilde{\varepsilon}_{\text{eff}}$. The MG theory generally requires that the volume fraction of the host exceed ≈70%, *i.e.*, higher than the sum of all the rest components by [111, 112]

Besides MG, another commonly used effective medium approach is the Bruggeman effective medium approximation (EMA) [111, 113], which does not consider a host matrix by rather equalize all constituents. The implicit expression of dielectric function follows [111, 112]:

$$\sum_{j=1}^{N} \phi_j \frac{\tilde{\varepsilon}_j - \tilde{\varepsilon}_{\text{eff}}}{\tilde{\varepsilon}_j + 2\tilde{\varepsilon}_{\text{eff}}} = 0 \tag{2.13}$$

The EMA is usually considered more general compared to MG, particularly for inhomogeneous materials [114]. The solution to Eq. (2.13) is nonunique, hence requiring the consideration of determining the physically meaningful $\tilde{\varepsilon}_{\text{eff}}$ at each wavelength. This can be done by ensuring the imaginary part of the dielectric function, $\text{Im}(\tilde{\varepsilon}_{\text{eff}}) \geq 0$, along with observation of continuity and physical meaningfulness.

2.4 Direct Discrete-Scale Modeling of Radiation Transfer in Particle Beds

For modeling radiation transport in non-homogenous media, care must be taken to account for the scattering due to interfacial reflection and refraction. A continuous medium promotes light scattering from a volumetric effect that is associated with light interaction with grain boundaries, embedded pores and particles (sizes that are comparable to the wavelength), and impurities. The scattering mechanism may be captured using appropriate scattering phase functions such as the Henyey-Greestein (HG) phase function [28, 76] and can also be experimentally determined [76]. In a non-homogenous medium containing

large particles, the scattering mechanism is affected due to the change of refractive index when exiting from or entering a dissimilar medium. Examples include suspending particles in liquid or air [80], large bubbles in glass [67], porous ceramics [20, 61-64], and particle beds [11, 95]. Boundaries at which the change of refractive index takes place and the surface condition greatly affect the scattered direction.

2.4.1 Particle Bed Generation and Randomization

Modeling radiation transfer in particle beds in the geometric optics regime based on Monte Carlo Method facilitates numerical representation of spatial coordinates of the particles and ray tracing in a 3-dimentional environment. The scale of the modeling domain directly impacts the complexity of the simulation and the results rendering time. The numerical representation of particles beds can be developed either by rigorous formulations based on established understanding of particle packing behavior [51, 100], or using dedicated programs (*i.e.*, LIGGGHTS) with their specific particle-generating scheme [115, 116]. The later method was more preferred in modern studies to avoid complex mathematical relations for spatially distributed particles but suffers from inefficient computing power and long results rendering time.

Both the dimensional representation with finite width, length, and thickness and a repeating-unit representation of particle beds are tested in this dissertation. The fundamental building block that allows for accurate characterization dictates to a face-centered cubic (FCC) [106] whose arrangement is shown in Figure 2.1.

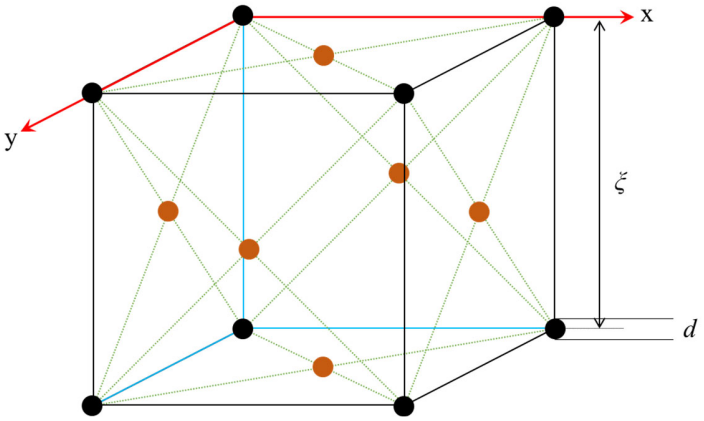

Figure 2.1. Schematic of a face-centered cubic with 8 spheres colored in black placed at each corner and 6 spheres colored in orange placed at the center of each face.

By default, the spheres have the location vector $\mathbf{r}_0 = \langle x_0, y_0, z_0 \rangle$ at the center. The z-direction is set as the direction of thickness. The particle volume fraction is given by

$$\phi_v = \frac{2\pi}{3}\left(\frac{d}{\xi}\right)^3 \tag{2.14}$$

where ξ is the length of a unit cell that contains four spheres, d is the particle diameter, and ϕ_v is the particle volume fraction. The adjacent particles (or spheres) in a standard FCC arrangement touch each other, resulting in ϕ_v = 74%. The particles no longer touch, and the volume fraction decreases when ξ is extended. By stacking the unit cells layer by layer until the prescribed bed thickness, a unit column is formed, so as the representation to the particle bed. In a repeating unit representation of particle bed, the unit column repeats itself in x- and y-direction and extends to infinity, while the thickness in z-direction is finite. For a dimensional representation, this repetition ends at a prescribed width (x-direction) and length (y-direction). Care must be taken then tracing photon bundles in beds using dimensional representation as there could be side leaking that may cause inaccuracy in simulation results. The subtle difference between the two particle bed generation methods

becomes more significant when the d is small and ϕ_v is high, causing large computation load when using the dimensional representation. Nevertheless, the dimensional method is more popular in fluid dynamic simulations of granular flow coupled with radiation heat transfer models [115, 116]. To avoid above issues, the repeating unit representation is used in this dissertation.

To account for the randomness of allocated particles in an actual particle bed, the center of each sphere is randomly shifted in the *x*-*y* plane within the margins for a bed that is not closely packed. The new central location $\mathbf{r}_c = \langle x_c, y_c, z_c \rangle$ is calculated by

$$\begin{cases} x_c = x_0 + \gamma(2\chi - 1) \\ y_c = y_0 + \gamma(2\chi - 1) \\ z_c = z_0 \end{cases} \tag{2.15}$$

where χ denotes a random number from 0 to 1, and γ is half of the clearance between particles in adjacent layers from an FCC arrangement to ensure no overlapping of particles. The randomization is applied simultaneously for all particles on one layer with different random numbers for each direction, and a new set of random numbers is regenerated for each subsequent layer to ensure no overlapping particles along with a certain degree of randomness. Without randomization, even beds of high particle volume fraction permit direct light transmission in regular FCC arrangement. To further ensure the randomness of the bed, after a certain number of photon bundles been traced, say 10, the random bed is regenerated according to Eq. (2.15).

2.4.2 Ray Tracing in Particle Beds

The photon bundles are launched above the unit column (analogy to particle bed when viewed as periodic structure) with 7° incidence along *z*-axis at a random location on the *x*-*y* plane confined by the cell side length ξ. This angle is chosen to be consistent with the experimental conditions. The results for incidence angles from 0° to 10° are essentially the same (within the statistical uncertainty). The gas medium (air) is assumed non-participating. Photon bundles travel within the bed and are subject to interception by particles or side boundaries of the unit column. The path of a photon bundle is described by the starting point with coordinates $\mathbf{s} = \langle s_x, s_y, s_z \rangle$ and a direction unit vector $\mathbf{v} = \langle v_x, v_y, v_z \rangle$. A flow chart describes the ray-tracing process as shown in Figure 2.2.

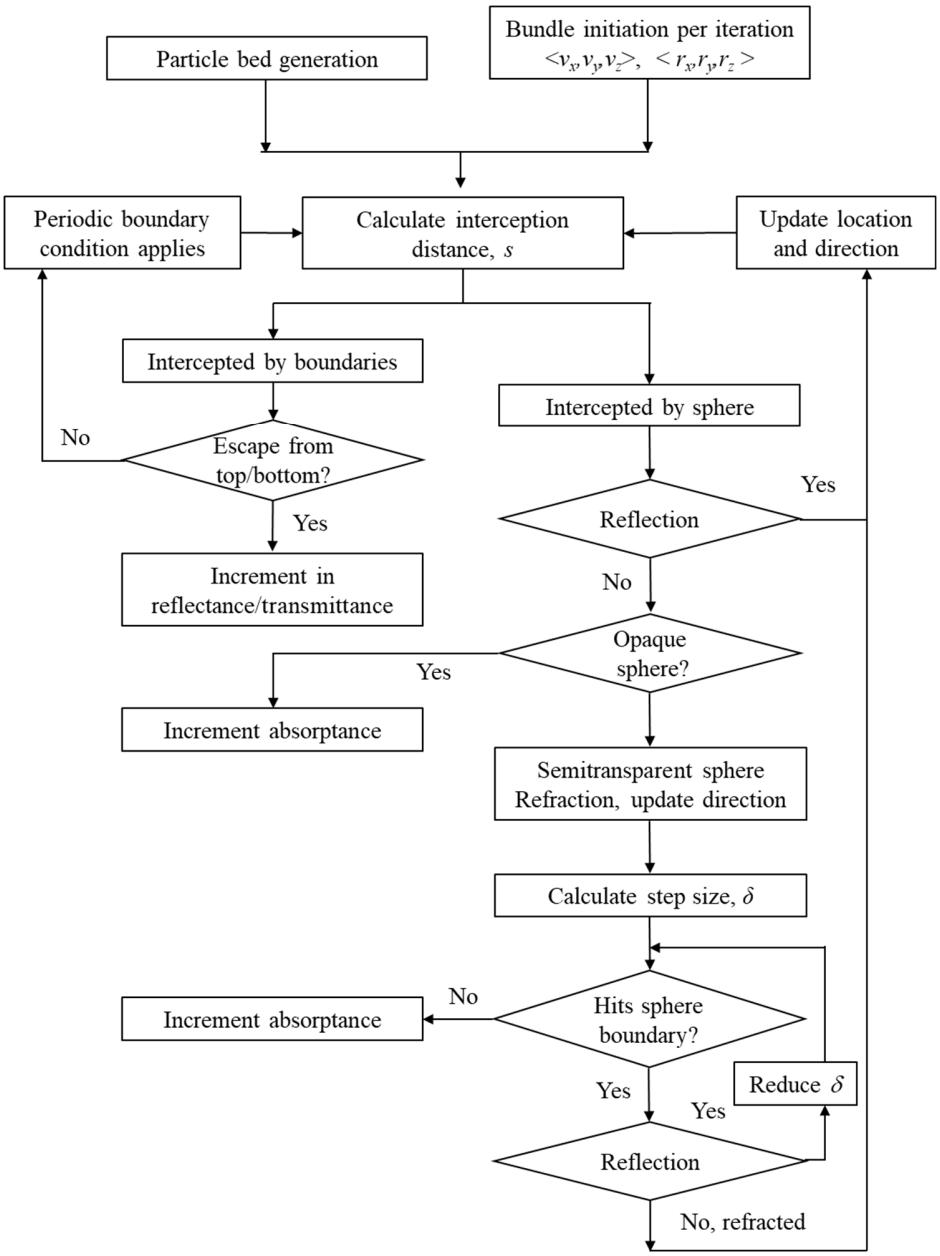

Figure 2.2. Flow chart of the Monte Carlo ray tracing simulation in a particle bed with unit-column representation.

Interception by a side boundary, $(x, y) = (0, 0)$, $(0, \xi)$, $(\xi, 0)$, or (ξ, ξ) triggers periodic boundary condition. Interceptions by particles (spherical surface) are modeled by reflection or refraction at the interface. The determination whether the photon bundle is reflected or refracted is realized by calculating the surface reflectivity, ρ, averaged from

two polarizations based on the Fresnel equations using the complex refractive index of the particle ($\tilde{n} = n + i\kappa$) [106]. A newly generated χ is compared with ρ such that reflection occurs when $\chi < \rho$ and otherwise refraction occurs. For refracted photon bundles that enter the particle, a similar process is followed with the next interception on the spherical surface. The attenuation is governed by the absorption index (κ) and the step size of a photon bundle is calculated from

$$\delta = \frac{\lambda}{4\pi\kappa}\ln(\chi) \tag{2.16}$$

where δ denotes a step size that a photon bundle may travel during each sub-level iteration within the sphere, and χ is a newly generated random number. When absorption is negligible (*i.e.*, $\kappa \approx 0$ and $\delta \to \infty$), the photon bundle may experience multiple reflections within the sphere but will eventually escape the sphere.

When tracing photon bundles outside of a particle (while still in the particle bed), the interception distance to a specific particle is calculated as:

$$\left(s_{x,\text{new}} - r_{x,\text{c}}\right)^2 + \left(s_{y,\text{new}} - r_{y,\text{c}}\right)^2 + \left(s_{z,\text{new}} - r_{z,\text{c}}\right)^2 = \left(d/2\right)^2 \tag{2.17}$$

$$s_{x,\text{new}} = s_x + v_x\zeta\,,\ s_{y,\text{new}} = s_y + v_y\zeta\,,\text{ and } s_{z,\text{new}} = s_z + v_z\zeta \tag{2.18}$$

where ζ is an intercept distance, and $\left\langle s_{x,\text{new}}, s_{y,\text{new}}, s_{z,\text{new}} \right\rangle$ denotes the new location vector. These relations reduce to a quadratic equation with two solutions (including the complex numbers and negative numbers) of ζ for each sphere in the unit column. Since ζ must be a real positive number, the smallest value corresponds to the closest particle that intercepts the photon bundle along the direction of propagation. The photon bundle may be intercepted by the side of the unit column before reaching a sphere; in such case, the

periodic boundary condition is applied to redirect the photon bundle to the unit column. This is to say that $0 \le s_x$ (or $s_{x,\text{new}}$) $\le \xi$ and $0 \le s_y$ (or $s_{y,\text{new}}$) $\le \xi$, regardless of their actual location in the global coordinates.

Tracing rays in a highly absorbing sphere (*e.g.*, near a phonon mode) becomes difficult as the refracted wavevector has significant imaginary component and the refraction angle becomes complex. Therefore, an optical thickness based on the diameter is defined as $\tau_d = 4\pi\kappa d/\lambda$ to determine whether the particle medium is regarded as opaque or semitransparent since the internal transmissivity is $\exp(-\tau_d)$ for a path length of d. For $\tau_d \gg 1$, the particle is considered as opaque and refraction is treated as absorption without further tracing. The surface reflectivity is calculated using the complex refractive index. For $\tau_d < 1$, in general, $\kappa \ll n$; hence, only n is used when calculating the surface reflectivity and the refraction angle. The real refraction angle enables further raytracing inside the particle following Eq. (2.16) to account for internal absorption.

2.4.3 Surface Irregularity and Particle Mixture

To compensate the effect of irregular shapes of particles and polydispersed nature of the particle bed, a specularity parameter $S \in [0,1]$ is introduced by allowing the photon bundles to specularly or diffusely reflect. A random number is compared with S to determine specular ($\chi < S$) or diffuse ($\chi > S$) reflection and refraction when launching a photon bundle. The surface condition is then regarded as perfectly specular or diffuse until the next photon bundle is generated.

When the mixing effect is present, ray tracing in particle beds is complicated by the material properties that may change per particle. For a dimensional representation of particle bed with finite length, width, and thickness, the center coordinates of all particles are stored such that it is possible to "color code" each particle with a specific material property, as shown in Figure 2.3.

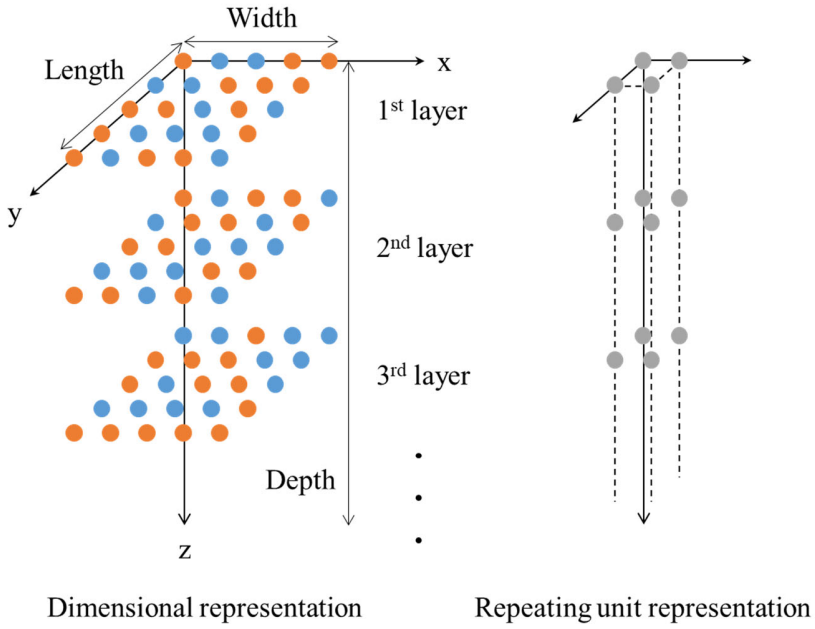

Figure 2.3. Schematics of particle beds that demonstrates mixing effect: a bed using dimensional representation with color coded spheres, and a bed using repeating unit (column) representation with optical properties of spheres determined by probability.

Upon the incidence by a photon bundle, the corresponding material property (*e.g.* complex refractive index) is invoked to proceed to the calculation of reflection and refraction. For particle beds based on repeating unit column with periodic boundary conditions, color coding is not possible. In this case, the particles are not assumed to have any material property until the incidence of a bundle that triggers the generation of another random number, χ, that is compared with the mixing ratio, r. The property of the particle

is then determined as either type 1 ($\chi < r$) or type 2 ($\chi > r$). Both methods are tested to be equivalent in Monte Carlo ray-tracing simulation and yield identical results.

The total number of photon bundles used in this dissertation is 10^5. It takes 10 runs to obtain the average and standard deviation in order to check the statistical variation and ensure reasonable outcome. In the semitransparent spectral region, it takes a much longer time to perform the ray tracing for each photon bundle. Therefore, the total number of photon bundles is reduced to improve the calculation speed without significantly reducing the computational accuracy.

CHAPTER 3

SPECTRAL RADIATIVE PROPERTIES OF CERAMIC PARTICLES FOR CONCENTRATED SOLAR THERMAL ENERGY STORAGE APPLICATIONS

This chapter provides an experimental and theoretical study on the radiative properties of particle beds made from bauxite ceramic particles. The measured spectral absorptance on an opaque particle bed is used to obtain solar absorptance from weighted integration. By assuming temperature independent properties, the overall emittance at high temperatures is calculated by integration over Planck's distribution. Two models from effective medium theory are used to approximate the dielectric function of the particles. Using the modeled results in a net radiation model, spectral absorptance is calculated and compared with the measurement. This work facilitates the characterization of radiative properties of particles with a windowed method and provides a modeling scheme for approximating the radiative properties of composite ceramic materials.

3.1 Particle Characterization

Selected ceramic particles from CARBO Ceramics, Inc. were analyzed for both CP and HSP types of particles in the Carbobead family. Three sizes are chosen from each type: CP 30/60, 40/100, and 50/140; HSP 16/30, 20/40, and 30/60. Here, the double numbers correspond to the upper and lower limits for the mesh grading, where each number inversely relates to the filtered particle size. The measured median product diameter (D50) and absolute density from the manufacturer and information about the constituents are given in Table 3.1.

Table 3.1. Information of Carbobead CP and HSP particles.

		Median diameter (μm)	Absolute density (kg/m^3)	Weight fraction (%wt)				
				Al_2O_3	SiO_2	Fe_2O_3	TiO_2	Others
CP particles	30/60	453	3.27	75	14	7	3	1
	40/100	270						
	50/140	194						
HSP particles	16/30	956	3.61	78	7	12	2	1
	20/40	697						
	30/60	495						

The weight fraction listed is subject to 5% uncertainty according to the manufacturer. Both CP and HSP particles have similar chemical compositions, except that the HSP has more Fe_2O_3 and less SiO_2 weight as well as higher density than the CP. All the measured radiative properties are for as-received particles without thermal exposure or treatment.

Microscope images of particles were taken from a Leica DVM6 digital microscope. Figure 3.1 shows the images for a set of CP 30/60 and HSP 30/60 particles at different resolutions.

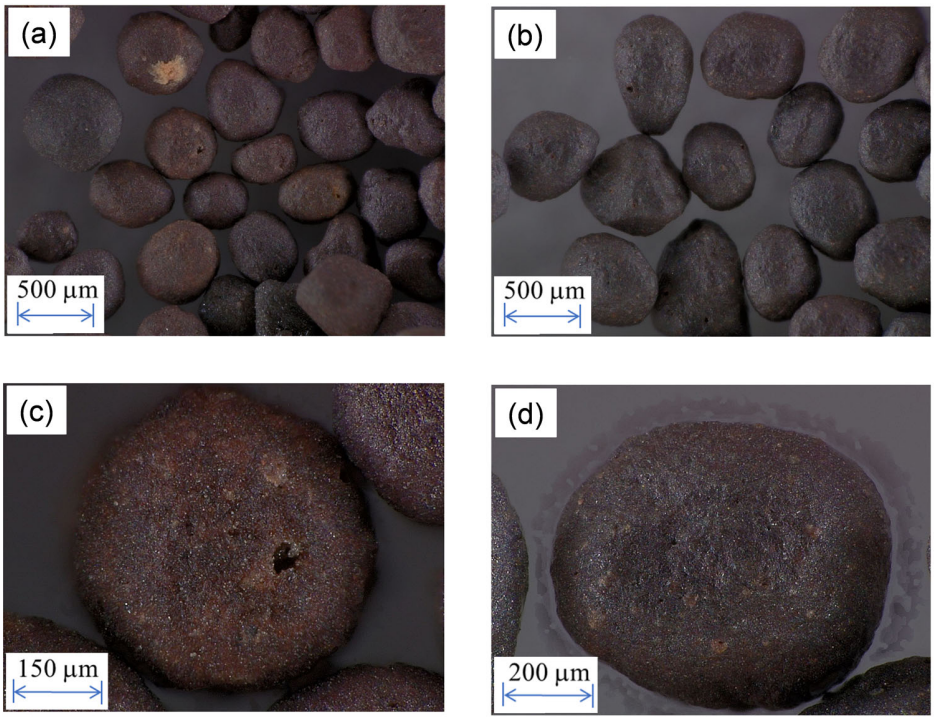

Figure 3.1. Digital microscope images of Carbobead particles: (a) CP 30/60 with a lower magnification (66×); (b) HSP 30/60 with a lower magnification; (c) CP 30/60 with a higher magnification (262×); (d) HSP 30/60 with a higher magnification.

It can be seen from Figs. 1a and 1b that the particles are distributed in a range of sizes and roundness, as discussed in [115]. The high-resolution images of individual particles (Figs. 1c and 1d) show that the particle surfaces are inhomogeneous with distinct color patches and surface roughness on the micrometer level. Surface morphology varies among particles with small dents present in some particles but not in others. The front part of the particles looks flat in the 2D images, while the actual particle shapes are nearly round [115]. Although both CP and HSP particles appear dark, CP particles seem brownish, suggesting more red light is reflected. This is confirmed from the spectrometric measurements (to be shown later): the absorptance of CP particles decreases toward the red end of the visible region, while the absorptance spectrum of HSP particles is slightly higher and flatter.

3.2 Instrumentation for Spectral Radiative Properties

A monochromator with an integrating sphere was used to measure the directional-hemispherical reflectance of samples in the visible (VIS) and NIR regions at an incidence angle of approximately 7.6° with a tilted sample holder. The light source is a tungsten-halogen lamp with a power stability of 1% [117]. Si and Ge photodetectors were used in conjunction with bandpass optical filters and metal diffraction gratings to provide a spectral coverage for 0.38 μm < λ < 1.8 μm [69, 118]. A 10-mm-thick polytetrafluoroethylene (PTFE) plate, made by pressed PTFE powder, was used as the standard reference due to its high diffuse reflectance [119]. To reduce measurement noise, 30 points were averaged over the sampling period. The measurement has an estimated uncertainty of 0.01 at 95% confidence level [117]. The signal-to-noise ratio is reduced near the spectral ends at the UV ($\lambda = 0.38$ μm) and NIR ($\lambda = 1.8$ μm) due to the detector noise and low transmittance of the optical filter, resulting in an increased uncertainty [118].

A Fourier-transform infrared spectrometer (FTIR) with a gold-coated integrating sphere was used to measure directional-hemispherical reflectance of the samples from NIR to the MIR region, at an incidence angle of approximately 7.7°. A liquid N_2 cooled HgCdTe (MCT) detector was used for the wavelength region from about 1.6 μm to 15 μm. A gold-plated reference with a diffuse reflectance of 0.95 was used to obtain the sample reflectance by interchanging the sample and reference [69, 118]. Each measurement was performed with a wavenumber resolution of 8 cm^{-1} and averaged over 1024 scans to improve the signal-to-noise ratio. In addition, several measurements were taken and averaged to reduce the uncertainty caused by repeatability. Post-processing was done by performing piecewise average as done previously to make the spectrum smoother [69, 118]. The uncertainty of

the FTIR reflectance measurements was estimated to be 0.02 with 95% confidence. The optical path after exiting the interferometer of the FTIR, including the integrating sphere and detector assembly, was purged with a N_2 gas. Near the H_2O vapor and CO_2 gas absorption bands (around 3 μm, 4.2 μm, and 6 μm), some fluctuations often show up in the measured spectrum due to the variation of the purge conditions from the sample measurement to the reference measurement. Repeated measurements also help to diminish the effect caused by vapor and gas absorption.

3.3 Windowed Method

A packed particle bed with controlled bed thickness was employed to overcome the difficulties in performing spectral measurements with individual single particles. The geometry of the "windowed method" is illustrated in Figure 3.2, where the particles are almost closely packed within the gap created by the spacer ring.

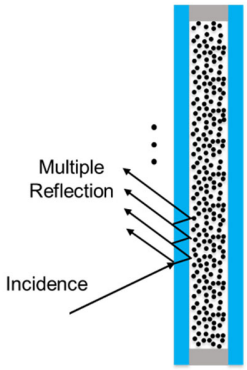

Figure 3.2. Schematic of a particle bed sandwiched between two transparent window materials, and the ray-tracing diagram showing multiple reflections by the window and particle bed (which is thick enough to be opaque).

A net-radiation model based on ray tracing is used to determine the particle bed reflectance by accounting for the reflection by the window as well as multiple reflections.

Due to the small contact area between the particles and the window, an air gap is assumed to exist between the window and the particle bed for ray-tracing calculations, as shown in Figure 3.2. The reflectance of the windowed particle bed, or simply "sample", is be expressed as follows [28, 106]

$$R_{\mathrm{s},\lambda} = R_{\mathrm{w},\lambda} + T_{\mathrm{w},\lambda}^2 \left(\frac{R_{\mathrm{p},\lambda}}{1 - R_{\mathrm{p},\lambda} R_{\mathrm{w},\lambda}} \right) \tag{3.1}$$

where R and T denote the reflectance and transmittance, respectively, and the subscript λ signifies a spectral property. The subscripts p, s, and w indicate, correspondingly, the particle bed, sample (particle bed + window), and window only. In order to deduce the particle bed reflectance from Eq. (3.1), the radiative properties of the windows must be predetermined. The transmittance and reflectance of the window can be calculated from the optical constants of the window material (Sec. 2.2.3), or directly measured using the spectrometer. Both methods are used in this study and compared to validate the experiments. When the window thickness is much greater than the wavelength, only multiple reflections need to be considered and interference effects are negligible [106].

When radiation is reflected by the particle bed, the reflected beam is not specular due to surface roughness, curvature, as well as cavities formed between the particles. However, since a nearly transparent window is chosen, τ_λ is very close to 1. Besides, when the average of the two polarizations is applied, the calculated ρ_λ does not change much with the angle of incidence until near the grazing angle. Since the integrating sphere measures the directional-hemispherical reflectance of the sample $R_{\mathrm{s},\lambda}$, the value $R_{\mathrm{p},\lambda}$ obtained from Eq. (3.1) is indeed the directional-hemispherical reflectance of the particle

bed. Since the particle bed is opaque, the spectral absorptance of the particle bed is calculated by

$$\alpha_{p,\lambda} = 1 - R_{p,\lambda} \tag{3.2}$$

The main advantage of this windowed method is that it enables the optical characterization of particle samples that are otherwise loose and hard to measure if not gathered as aggregates.

3.4 Measured Radiative Properties of the Particle Beds

The validation of the windowed method can be found in [95]. The particle bed reflectance is determined using the two spectrometers as discussed previously with the windowed method. Since the particle bed is opaque, the near-normal absorptance is calculated from Eq. (3.2) and shown in Figure 3.3 for three sets of CP and HSP particles, respectively, from 0.38 μm to 15 μm (Note: the minimum of the vertical axis is 0.6).

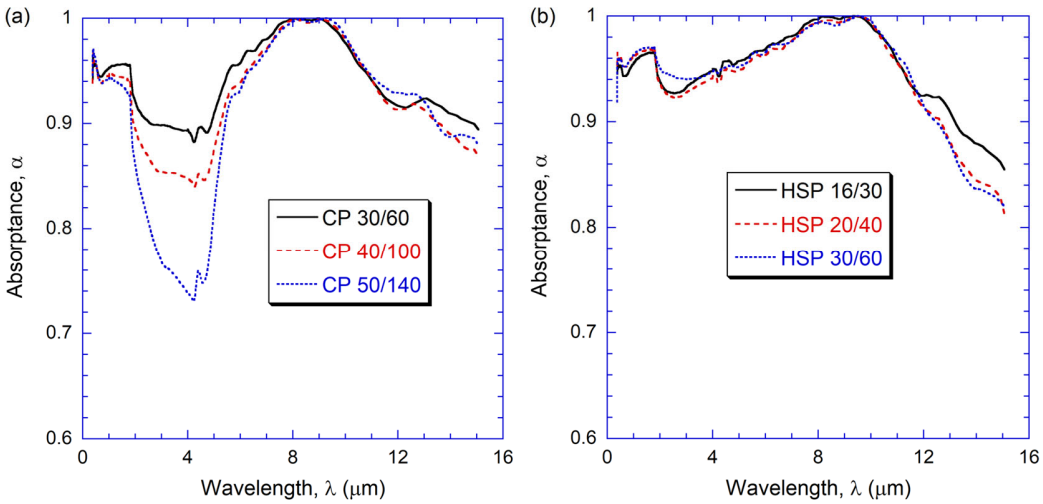

Figure 3.3. Spectral absorptance of particle beds in the wavelength region from 0.38–15 μm: (a) CP particles with sizes 30/60, 40/100, and 50/140; (b) HSP particles with sizes 16/30, 20/40 and 30/60.

There is some disagreement in the overlapping region from 1.6 μm to 1.8 μm, where the noise in the FTIR measurement is high. Since the dispersive spectrometer measurement has a smaller uncertainty, especially with the glass window, the measurements from 0.38 μm to 1.8 μm are based on the grating spectrometer. The FTIR results are directly used from 1.9 μm to 15 μm, while a linear interpolation is performed from 1.8–1.9 μm to merge the spectra smoothly. In general, the particle bed has a very high absorptance that approaches unity in the region from 8.0 μm < λ < 9.5 μm due to the combination of infrared phonons in the constituent materials (to be discussed in the next section). A dip in absorptance is observed in the CP particles for 2 μm < λ < 5 μm and becomes deeper for smaller particle sizes, possibly due to lower Fe_2O_3 fraction and the effective radiative penetration depth.

All six absorptance spectra are replotted at wavelengths up to 4 μm in Figure 3.4, along with the solar irradiance spectrum for air mass (AM) 1.5 [120], with a minimum in the vertical axis for the absorptance of 0.75. Due to the higher Fe_2O_3 fraction in the HSP than in CP particles, the NIR absorptance in general is higher for the HSP than for CP particle beds. For λ < 0.5 μm, the absorptance for the CP and HSP particle beds is similar, though CP particles often possess a higher absorptance than HSP particles. The reason is explained in Sec. 4.3 considering the competing effects of absorption and surface reflection.

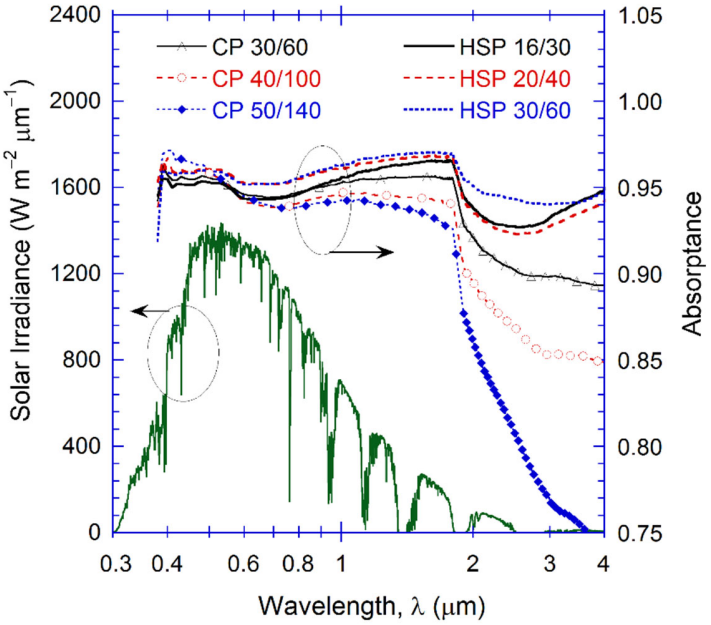

Figure 3.4. Solar irradiance and particle bed absorptance spectra up to $\lambda = 4$ μm

Comparing CP 30/60 and HSP 30/60, the VIS reflectance of the CP increases from approximately 0.045 at λ = 0.45 μm to 0.056 at λ = 0.68 μm, while that of the HSP increases from approximately 0.042 at $\lambda = 0.45$ μm to 0.048 at $\lambda = 0.68$ μm. This suggests that for similar particle size 30/60 (with slightly different averaging particle diameters), the CP is more reflecting than the HSP, especially in the red end (longer wavelengths) of the VIS spectrum. The spectrometric measurements provide quantitative evidence for the color appearance in the microscopic images shown in Figure 3.1, though the difference is not very significant.

The solar weighted absorptance or simply solar absorptance is determined as

$$\alpha_{\text{solar}} = \frac{\int_{\lambda_1}^{\lambda_2} \alpha_\lambda(\lambda) G_{\lambda,\text{solar}}(\lambda) d\lambda}{\int_{\lambda_1}^{\lambda_2} G_{\lambda,\text{solar}}(\lambda) d\lambda} \tag{3.3}$$

where $G_{\lambda,\text{solar}}$ is the direct solar irradiation according to AM1.5 [120], and the integration limit is set to $\lambda_1 = 0.28$ μm and $\lambda_2 = 4.0$ μm. For $\lambda < 0.38$ μm, the spectral absorptance is assumed to be the same as that at $\lambda = 0.38$ μm. The obtained absorptance has similar trend as the previous measured results for CARBOHSP and ACCUCAST particles [14, 25]. However, the absorptance obtained from the present study is nearly 3% higher than the previously reported value; the reason may be due to the variation of the particle group, batch, and composition.

The spectral emittance is determined from the spectral absorptance by applying Kirchhoff's law [106]: $\varepsilon_\lambda(\lambda) = \alpha_\lambda(\lambda)$ for normal incidence. The highly absorbing particle bed is assumed as a diffuse surface such that the normal emittance is the same as the hemispherical emittance. The spectral emittance is assumed to have negligible temperature dependency. Hence, the total hemispherical emittance at a given temperature T is calculated by performing the weighted integration over Planck's blackbody distribution [28]:

$$\varepsilon(T) = \frac{E(T)}{E_\text{b}(T)} = \frac{1}{\sigma T^4}\int_0^\infty \varepsilon_\lambda(\lambda) E_{\text{b},\lambda}(\lambda, T)\, d\lambda \tag{3.4}$$

where E denotes the total emissive power, $E_{\text{b},\lambda}(\lambda, T)$ denotes the spectral emissive power of a blackbody, and σ is the Stefan-Boltzmann constant.

Both solar absorptance and total emittance at T = 1000 K were calculated using the spectral absorptance as listed in Table 3.2. The integration bounds are from 0.38 μm to 200 μm by taking the spectral absorptance beyond λ = 15 μm as a constant. The error caused by such extrapolation is negligibly small since only about 3% of the blackbody radiation at 1000 K falls at λ > 15 μm.

Table 3.2. Solar absorptance and total hemispherical emittance evaluated at 1000 K for CP and HSP particles.

	CP			HSP		
	30/60	40/100	50/140	16/30	20/40	30/60
Solar absorptance, α_{solar}	0.949	0.943	0.940	0.951	0.957	0.957
Total emittance at 1000 K, ε	0.922	0.893	0.843	0.949	0.942	0.950

The solar absorptance for HSP particles averaged 0.955, which is slightly higher than that for the CP particles (averaged 0.944). The infrared emittance of the three types of HSP particles are all higher than 0.95. Due to the dip in the absorptance around 4 μm, the overall emittance of the CP particles is somewhat lower, especially for CP 50/140, which is 0.843. The spectral and integrated absorptance and emittance provide needed information for the design of CSP using particle receivers. The underlying mechanisms for the spectral absorptance are further elucidated by analyzing the optical properties of individual constituents and then using effective medium models, as discussed next.

3.5 Effective Medium Modeling Results and Comparison with Experiments

To apply either of the effective medium formulation discussed in Sec. 2.3.2, the dielectric functions of individual constituents must be determined beforehand. X-ray diffraction analysis reveals that the particles from CARBO Ceramics Inc. contain crystalline components, such as α-Al_2O_3 (corundum), α-Fe_2O_3 (hematite), α-SiO_2 (a crystalline quartz), and TiO_2 (rutile) [115]. Although more complicated compound can also

form, such as mullite ($3Al_2O_3 \cdot 2SiO_2$), Fe_2TiO_5, etc. [25], for simplicity, only the simple oxides are used in the effective medium modeling. These materials are uniaxial whose dielectric response can be described by a diagonal tensor such that $\overline{\overline{\tilde{\varepsilon}}} = \mathrm{diag}(\tilde{\varepsilon}_\mathrm{O}, \tilde{\varepsilon}_\mathrm{O}, \tilde{\varepsilon}_\mathrm{E})$ when the optic axis is parallel to the *z*-axis [106, 121]. Here, the subscript O represents the ordinary dielectric function for electric field parallel to the *x*-*y* plane, while the subscript E represents the extraordinary dielectric function for electric field parallel to the *z*-axis (optic axis). Since the grains of the constitutes are polycrystalline and randomly oriented, a weighted average of the dielectric functions may be used such that [122]

$$\tilde{\varepsilon}_j = \frac{2}{3}\tilde{\varepsilon}_{j,\mathrm{O}} + \frac{1}{3}\tilde{\varepsilon}_{j,\mathrm{E}} \tag{3.5}$$

An alternative approach is to treat each constituent using the EMA formulation [110]:

$$2\frac{\tilde{\varepsilon}_{j,\mathrm{O}} - \tilde{\varepsilon}_j}{\tilde{\varepsilon}_{j,\mathrm{O}} + 2\tilde{\varepsilon}_j} + \frac{\tilde{\varepsilon}_{j,\mathrm{E}} - \tilde{\varepsilon}_j}{\tilde{\varepsilon}_{j,\mathrm{E}} + 2\tilde{\varepsilon}_j} = 0, \;\; j = 1,\; 2,\; \ldots N \tag{3.6}$$

While both Equations yield very similar results, Eq. (3.6) is more logical since EMA is based on the spatially averaged field [112, 114]. For this reason, Eq. (3.6) is used in the present study to evaluate the dielectric function of each individual oxide using the ordinary and extraordinary optical constants obtained from the literature. Both the MB theory and EMA are used to calculate the effective dielectric function and compared as discussed in Sec. 4.3.

As shown in Table 3.1, the particles consist mainly of corundum, hematite, crystalline quartz, and rutile. The volume fraction of Al_2O_3 is calculated to be over 60% for CP particles and 70% for HSP particles. In addition, there are about 1%wt of other materials. Calculation of the weighted density suggests that the volume fraction of air pores

is about 13% for CP particles and 9% for HSP particles. For heterogeneous materials as such the ceramic particles used here, the effective medium approaches are not expected to provide accurate results, due to internal scattering effects, but may offer physical insights into the absorption mechanisms.

The optical properties of each metal oxide are taken from the literature. For α-Al_2O_3, α-SiO_2, and TiO_2, the optical constants are obtained from Palik [123] and then the average dielectric function was calculated from Eq. (3.6). The absorption coefficients for α-SiO_2 at wavelengths from 2.6 μm to 6.5 μm were taken from Wood [124] to extend the region where Palik's compilation [123] did not include the absorption index. Note that the absorption peak near 3 μm is attributed to defects containing water [124]. Glasscock et al. [125] measured the optical properties of α-Fe_2O_3 films and identified the direct and indirect band gaps located at wavelengths near 0.46 μm and 0.65 μm, respectively. The bandgap absorption causes strong VIS/NIR absorption in α-Fe_2O_3 extending to 1.5 μm. In the MIR region, Onari et al. [126] studied lattice vibrations and obtained dielectric functions of α-Fe_2O_3 for both polarizations. Their results are combined to give the optical constants used in the present work. The refractive index from [125] at λ = 2 μm connects well to that calculated from the expression from [126]; however, there is a large gap in the absorption index. A linear interpolation is used for κ in the wavelength region from 1.5 μm [47] to 3 μm [126].

The refractive index, absorption coefficient, are shown in Figure 3.5 for each oxide material for 0.3 μm < λ < 16 μm.

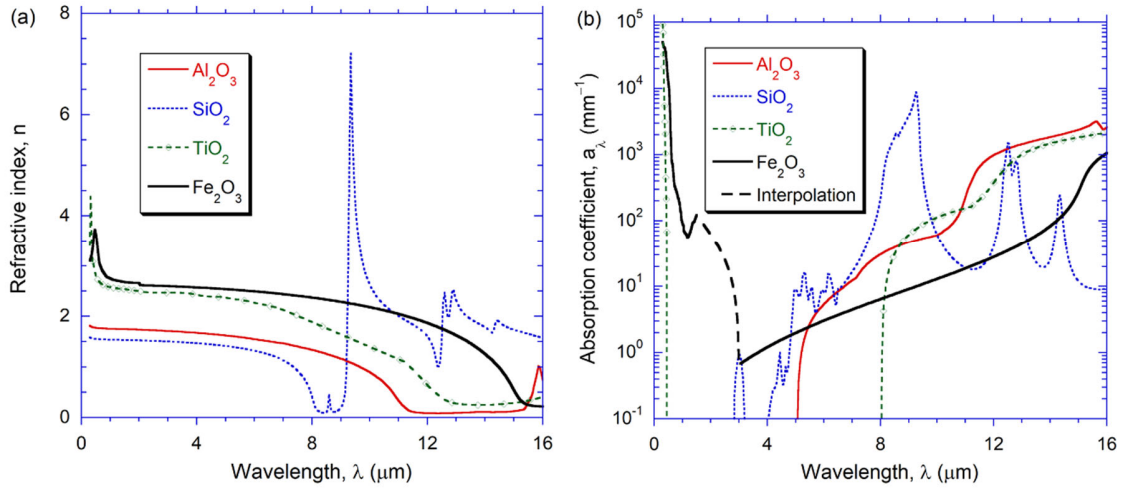

Figure 3.5. Average spectral properties of individual constituent material from 0.3–16 μm: (a) refractive index; (b) absorption coefficient.

The phonon features are clearly seen at $\lambda > 8$ μm, causing rapid changes in the refractive index down to nearly zero in some regions, as well as reststrahlen bands with strong absorption and high reflection [106]. The Christiansen wavelengths are 7.35 μm, 9.65 μm, 11.3 μm, and 14.4 μm for SiO_2, Al_2O_3, TiO_2, and Fe_2O_3, respectively. The absorption coefficient for $0.5\ \mu m < \lambda < 5\ \mu m$ is very small except for Fe_2O_3. Although the wavelength corresponding to rutile's bandgap is near 0.41 μm, making it highly absorbing at $\lambda < 0.45$ μm, the small concentration makes the contribution of TiO_2 insignificant. Hence, Fe_2O_3 is expected to contribute most to the solar absorptance of the particles. The volume fractions of Fe_2O_3 for CP and HSP particles are 4% and 8%, respectively. Therefore, HSP particles are expected to be more absorbing in the UV/VIS/NIR regions. Since Fe_2O_3 has a high refractive index in the VIS/NIR region compared with other oxides as shown Figure 3.5a, the surface reflectivity is also the highest at $\lambda > 0.5$ μm.

Both the MG theory and EMA are used to calculate the effective refractive index and absorption index for the two types of particles, as shown in Figure 3.6 for $0.3\ \mu m < \lambda$

< 16 μm. The difference between the two models is small at wavelengths of $\lambda < 8$ μm. Due to high volume fraction of Fe_2O_3 in HSP particles compared to CP particles, n of HSP particles is greater than that of CP particles at $\lambda < 8$ μm and κ of HSP particles is slightly greater than that of CP particles at $\lambda < 4$ μm. The relatively small volume fraction of air also contributes to the larger refractive index in HSP particles. The absorption index increases rapidly toward decreasing wavelength when $\lambda < 1$ μm. At $\lambda > 8$ μm, MG model generally gives more oscillations with higher variations in the optical constants than EMA, suggesting that MG is more sensitive to the phonon features of individual oxide than EMA.

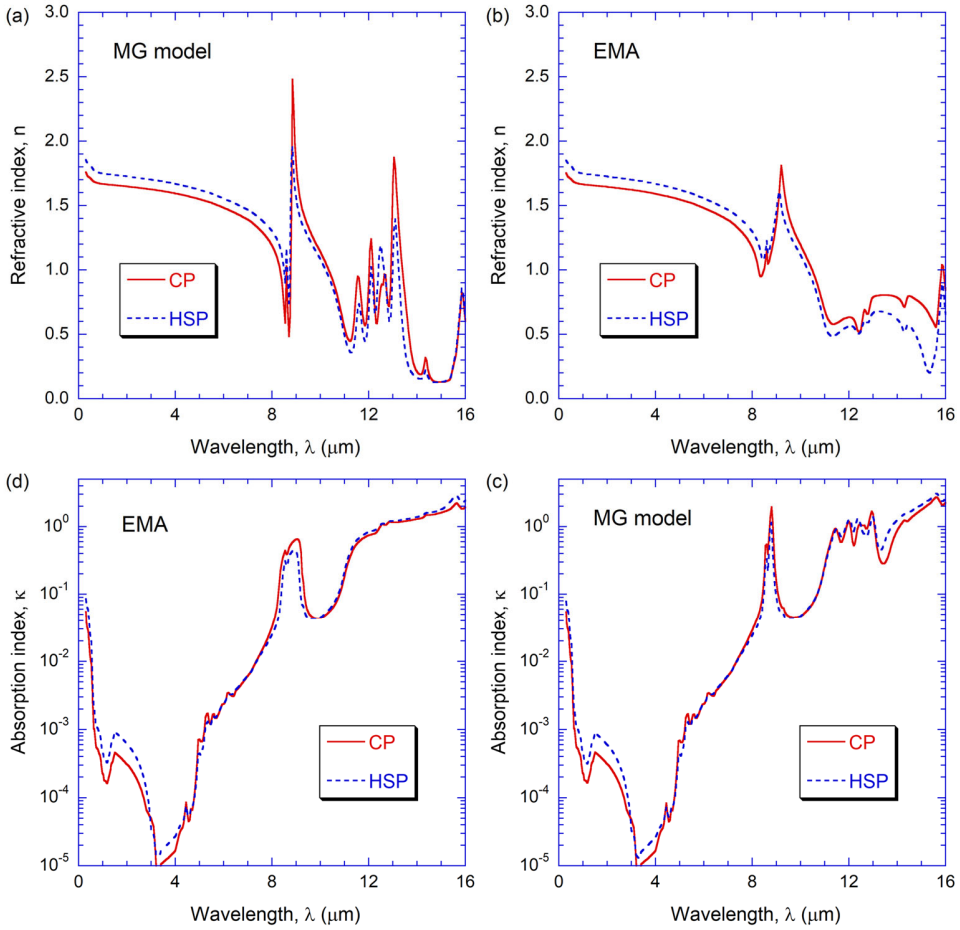

Figure 3.6. Calculated effective refractive index and absorption index of the CP and HSP solid particles: refractive index from (a) MG model and (b) Bruggeman's EMA; absorption index from (c) MG model and (d) EMA.

The optical constants obtained from both effective medium approaches are used to calculate the reflectivity of a smooth surface using Eq. (2.10), then the absorptance is calculated from $\alpha_\lambda = 1 - \rho_\lambda$. The absorptance spectra for CP and HSP particle surfaces are plotted in Figure 3.7 and compared with those of CP 30/60 and HSP 30/60 particle beds obtained using the windowed method.

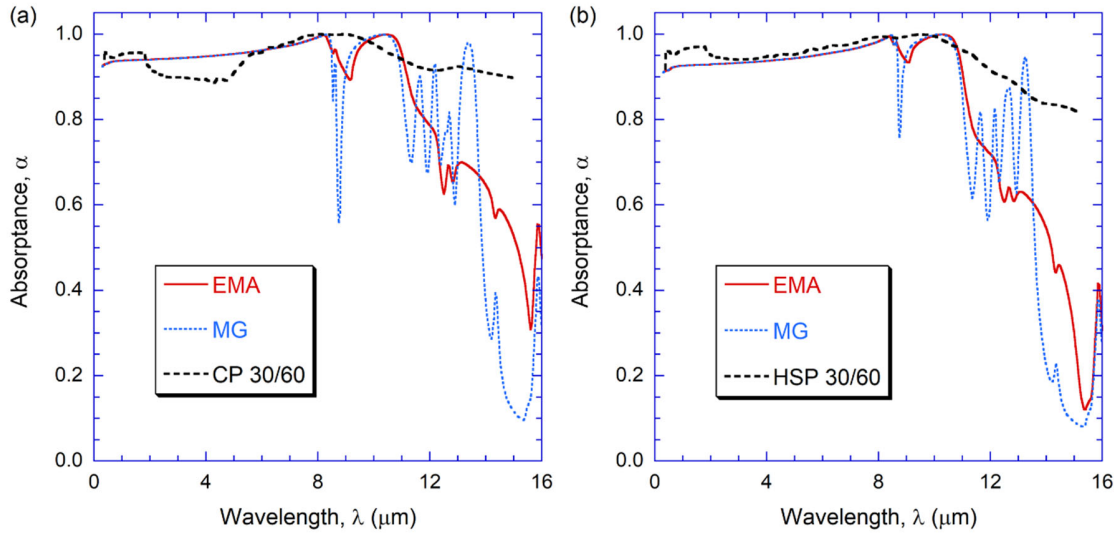

Figure 3.7. Comparison of the modeled absorptance for a plate with that measured for a particle bed with sizes 30/60: (a) CP particles; (b) HSP particles.

As expected, the absorptance spectrum calculated using the MG model contains multiple resonances that are not observable in the measurements. The EMA better captures the general trend, especially the high absorptance in the region of 8 μm < λ < 11 μm, and the reduced absorptance toward longer wavelengths. A quantitative comparison suggests that the calculated absorptance from EMA is more than 0.015 higher for the CP particles shown in Figure 3.7 (a) than for the HSP particles shown in Figure 3.7 (b) at λ < 0.55 μm. This is due to the lower refractive index of the CP particles as shown in Figure 3.6 (c). As the wavelength increases to the red end of the VIS spectrum and NIR region, the surface

reflectance effect becomes weaker whereas higher absorption coefficient of the HSP particles start to dominate, resulting in a higher absorptance in the NIR region as seen in Figure 3.4. The measured absorptance of the particle beds at $\lambda > 8$ μm is higher than the EMA calculation; this is mostly likely due to multiple reflections since the particle bed contains cavities and the actual particle surface is not smooth. Multiple reflections may also be responsible to the high absorptance of the HSP 30/60 particle beds at shorter wavelengths; however, the dips in the absorptance spectra for HSP 16/30 and 20/40 in the region 2 μm < λ < 4 μm as shown in Figure 3.3 and 3.4. cannot be explained. Note that the average particle diameters for all particles are much greater than the wavelength, so interference and diffraction effects are negligible. Surface morphology variations may also affect the reflectance in this region since the effective absorption index is relatively small. Experimental uncertainty due to the H_2O(v) absorption in this region may also contribute to the absorptance dip. Further investigation is necessary to determine the exact reasons.

Attention is now turned to the particle size dependent dips in the absorptance for the CP particles shown in Figure 3.3 (a) in the wavelength region from 2 μm to 5 μm. Clearly, these features cannot be explained by the calculations given in Figure 3.7 (a). Based on the effective absorption indices shown in Figure 3.6 (d), the radiation penetration depth calculated by $\delta_\lambda = 1/a_\lambda = \lambda/(4\pi\kappa)$ is several tens of centimeters near $\lambda = 4$ μm, though the actual penetration depth is expected to be much lower due to scattering. Since the penetration depth is greater than the average particle diameter, refraction and multiple reflections can increase diffuse reflection from the particle bed, causing the lower absorptance of the particle bed near $\lambda = 4$ μm, especially with CP particles. Smaller particles are more transparent, resulting in stronger multiple reflection and scattering

effects. Subsequently, the reflectance becomes higher and absorptance becomes lower for particle bed with smaller particles. This is why the absorptance is the smallest for the CP 50/140 particle bed around 4 μm as shown in Figure 3.3 (a). For HSP particles, the reduction of absorptance and distinction between different particles are insignificant. This suggests that there may exist additional impurities or chemical compositions that give rise to a stronger absorption in HSP particles for $2.5\ \mu m < \lambda < 5\ \mu m$.

Other materials, though with only 1%wt fraction, may also attribute to the NIR absorption. Furthermore, the effective medium models neglect volume scattering effects inside the particle by the pores and between different oxides. Surface roughness and inhomogeneity may cause additional scattering effects. Nevertheless, the EMA model provides valuable insights on the observed absorptance mechanisms by considering contributions from the individual constituents. Further modeling studies using Monte Carlo method are needed to help explain the observed surface scattering, volume scattering, and multiple reflections between particles [64, 69, 79, 127].

CHAPTER 4

SPECTRAL RADIATIVE PROPERTIES OF POLYDISPERSED SILICA PARTICLE BEDS

This chapter provides an experimental investigation of the radiative properties of polydispersed silica particle beds by measuring the spectral directional-hemispherical reflectance and transmittance from visible to MIR region. The absorption and reduced scattering coefficients of beds with various thicknesses are retrieved from an inverse adding-doubling model (IAD). The effect of dependent scattering is assessed from forward analysis utilizing independent scattering theory. A Monte Carlo model is used to also simulate the measured radiative properties considering surface roughness and internal absorption by particles.

4.1 Experimentation

4.1.1 Particle Characterization

Polycrystalline SiO_2 particles of different sizes are used to form the packed bed samples with different thicknesses. Three types of particles are chosen based on their average diameters: (1) Type A (d = 222 μm), (2) Type B (d = 150 μm), and (3) Type C (d = 40 μm). Type A particles are round grain silica sand manufactured by Wedron Silica Co. (Wedron 410), with ~ 99.65% purity. The Wedron 410 particles are jet milled to produce power with an average diameter of ~ 40 μm, which are identified as Type C in this study. Type B particles are obtained from US Research Nanomaterials, Inc. They were

manufactured the airflow crushing method from large quartz particles with a purity > 99.5%. The microscopic images of these particles are shown in Figure 4.1.

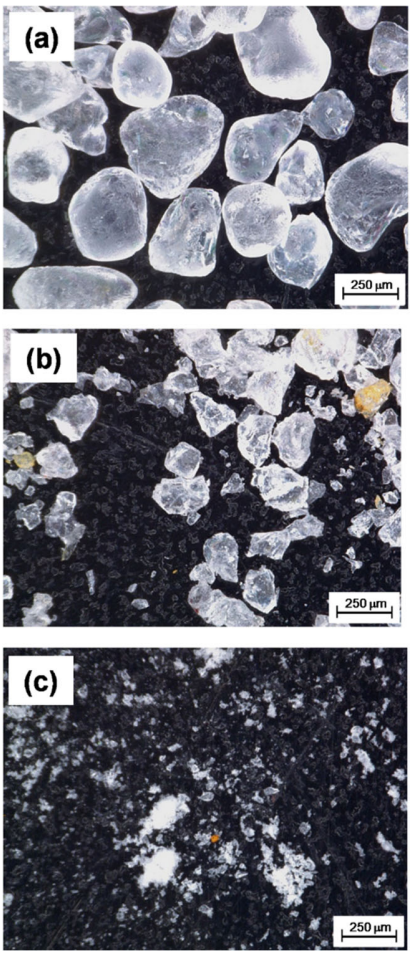

Figure 4.1. Digital microscope images of the three types of SiO_2 particles: a) Type A with d = 222 µm; b) Type B with d = 150 µm; c) Type C with d = 40 µm.

The Type A particles are more uniform and spherical, Type B particles exhibit more irregularities and contain additional impurities, and Type C particles are powder-like with irregular fragments and flakes. The diameters for Type A or B particles are determined by volume averaging using the sieve filtration method. A nominal diameter based on microscopic images is used for Type C particles. A small fraction of other oxides (*i.e.*,

Al_2O_3, TiO_2, and Fe_2O_3) is present, resulting in weak absorption in the visible and near-infrared regions.

4.1.2 Experimental Setup

The particles are encased in a windowed sample holder, consisting of two transparent layers (front and back) and a spacer ring of various thicknesses, as shown in Figure 4.2 (a) with fused quartz windows for measurements from 0.38 μm to 1.8 μm using a monochromator. For mid-infrared measurements using a Fourier-transform infrared spectrometer (FTIR), ZnSe windows are used to hold the particles.

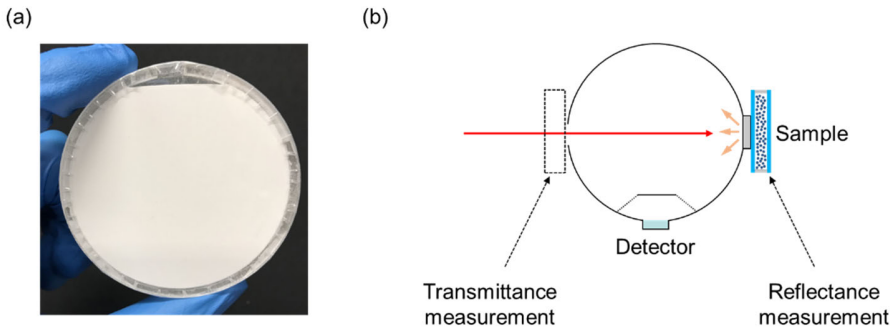

Figure 4.2. Measurement of windowed particle bed: a) a picture of particles in a windowed sample holder; b) schematic illustration of the integrating sphere measurement of directional–hemispherical transmittance and reflectance of the sample.

The directional–hemispherical transmittance or reflectance is measured by placing the sample at the front or back of an integrating sphere, as shown in Figure 4.2 (b), with suitable references. Detailed description of the measurement procedure based on net radiation method is found in [30]. Once the sample holder is filled with particles, the particle bed has the same thickness as the spacer ring with nominal thicknesses: L = 1.0 mm, 1.6 mm, 3.4 mm, and 6.2 mm. The actual spacer thicknesses are 0.97±0.01 mm, 1.61±0.02 mm, 3.37±0.03 mm, and 6.23±0.03 mm as measured with a caliper. Only

nominal thicknesses are referred to hereafter for clarity. The particle volume fractions (ϕ_v) are measured and averaged over all thicknesses for each type of particles and the results are tabulated in Table 4.1.

Table 4.1. Particle information and polynomial fitting parameters.

Sample identification	Type A		Type B		Type C	
Average diameter, d (μm)	222		150		40	
Particle volume fraction, ϕ_v	0.68		0.60		0.72	
Polynomial fitting of absorption and reduced scattering coefficients						
$a_\lambda \left(\text{or } \sigma_\lambda\right) = b_0 + b_1\lambda + b_2\lambda^2 + \ldots \quad \left(\lambda \text{ in } \mu\text{m}\right)$						
Fitted parameter, mm^{-1}	a_λ	σ_λ	a_λ	σ_λ	a_λ	σ_λ
Degree of polynomial	4	4	6	4	6	2
b_0	0.90700	3.395	12.726	10.739	8.5780	80.624
b_1	–2.4610	–2.440	–64.934	–9.8200	–43.566	–43.224
b_2	2.6400	2.736	137.47	11.507	93.325	11.449
b_3	–1.2650	–1.399	–152.68	–6.2870	–105.98	
b_4	0.22600	0.2700	93.631	1.2910	66.818	
b_5			–30.057		–22.107	
b_6			3.9480		2.9950	

Due to irregular shapes, polydispersed condition and different sample fabrication processes, no apparent relation between ϕ_v and d is observed. Nevertheless, the particles are densely packed and a validation by Monte Carlo ray-tracing method showed a very small impact for the range of ϕ_v studied in this work. Reflectance and transmittance measurements are performed on multiple spots of the sample and the averaged results are used to mitigate the impact of localized packing unevenness

.

4.2 Measurement Results, Analysis, and Comparison with Modeling

4.2.1 Measured Reflectance

The reflectance in the spectral region 0.4 μm < λ < 15 μm of the particle bed with L = 6.2 mm is shown in Figure 4.3 for all three types of particles, identified by the average particle diameter.

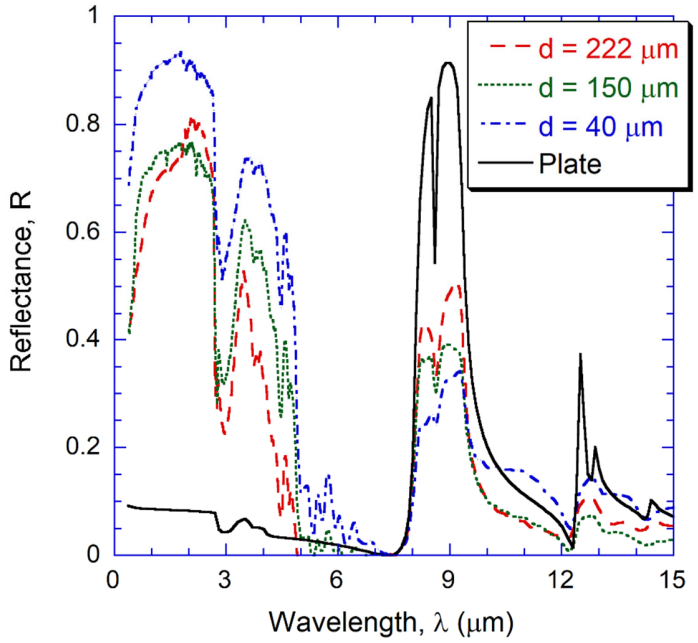

Figure 4.3. Measured reflectance spectra of SiO_2 particle beds at L = 6.2 mm, and the calculated reflectance spectrum for a flat plate having the same thickness.

The particle beds are essentially opaque for these thicknesses. Note that R is deduced from the measured windowed sample reflectance considering properties of the fused quartz or ZnSe windows in different spectral region [95]. Due to the difference in measurement uncertainty and decreased signal-to-noise ratio near the spectral limits of the instruments, the results for 0.4 μm < λ < 1.8 μm are based on monochromator measurements, and results for 1.9 μm < λ < 15 μm are based on the FTIR measurements. A linear interpolation is used for 1.8 μm < λ < 1.9 μm to smoothly merge the two spectra. For comparison purpose, the calculated R for a 6.2-mm-thick flat SiO_2 plate is also shown, considering the ordinary and extraordinary effective dielectric functions of α-quartz [95, 106]. The optical constants are mainly taken from Philipp [128] with some modifications on κ from 2.7 μm to 5.0 μm, considering absorption due to impurity [124, 129, 130].

In the region for 0.4 μm < λ < 5 μm, the plate sample is transparent or semitransparent with a low R (< 10%) because of the small refractive index of the polycrystalline silica (n < 1.6). When n decreases to unity at λ ≈ 7.3 μm, R = 0 (*i.e.*, the Christiansen effect) [106]. Particle scattering causes significant enhancement in R at short wavelengths, especially with Type C particles (d = 40 μm). This is a well-known phenomenon: a high reflectance (≈99%) has been demonstrated using micron-sized glass spheres for daytime radiative cooling purpose [131]. Due to impurity absorption, R for the particle beds drops quickly toward shorter wavelengths when λ < 1 μm. This is not observed for pure α-quartz plate samples. There is a dip for 2.7 μm < λ < 3.4 μm in R

due to OH stretching [124]. Scattering causes high R for 3 μm < λ < 5 μm and even near the Christiansen wavelength for Type C particles.

Near the phonon reststrahlen absorption band (8 μm < λ < 10 μm), $\kappa > n$ and surface reflectivity becomes very high. All particles and plate samples are considered as opaque in this region since the photon penetration depth, $\lambda/(4\pi\kappa)$, is less than 1 μm. The opaque particles form cavity structures that traps the incoming photons, enhancing absorption [106]. Smaller particles with more irregularities effectively trap more photons. In addition, wave effects also potentially play a role at longer wavelengths. This provides a qualitative explanation of the reduction of reflectance with the particle bed, especially for smaller sized particles. The features at λ > 10 μm are more complicated and not easily explainable. For the plate sample, additional phonon resonances exist and the effects appear to be evened out with the particle beds. Wave effects cannot be neglected, and the reflectance does not vary monotonically as a function of the particle size.

4.2.2 Absorption and Scattering Coefficients by IAD

Both R and T are measured from 0.4 μm to 1.8 μm to further characterize the particle beds of different thicknesses. The effective absorption and reduced scattering coefficients (*i.e.*, a_λ and σ_λ) are retrieved from the measured R and T for a given thickness using IAD as described previously. For Type A particles, the obtained a_λ and σ_λ are averaged at each wavelength for L = 1.0 mm, 1.6 mm, and 3.4 mm, and then fitted to a polynomial function to obtain smooth functions. Due to the low transmittance at shorter wavelengths, the results for L = 6.2 mm is excluded. For Type B particles, T is measured only for L = 1.0 mm since it is very low for other thicknesses and completely opaque when

L = 6.2 mm. For Type C particle, T is negligibly small when $L \geq 1.6$ mm. Therefore, the IAD is only applied to the packed beds with L = 1.0 mm for Type B and C particles to obtain a_λ and σ_λ. The polynomial coefficients obtained from fitting are listed in Table 4.1 for all samples.

The measured R and T for Type A particles are shown (dashed lines) in Figure 4.4, and the results calculated with AD using the fitted a_λ and σ_λ are also shown (solid lines).

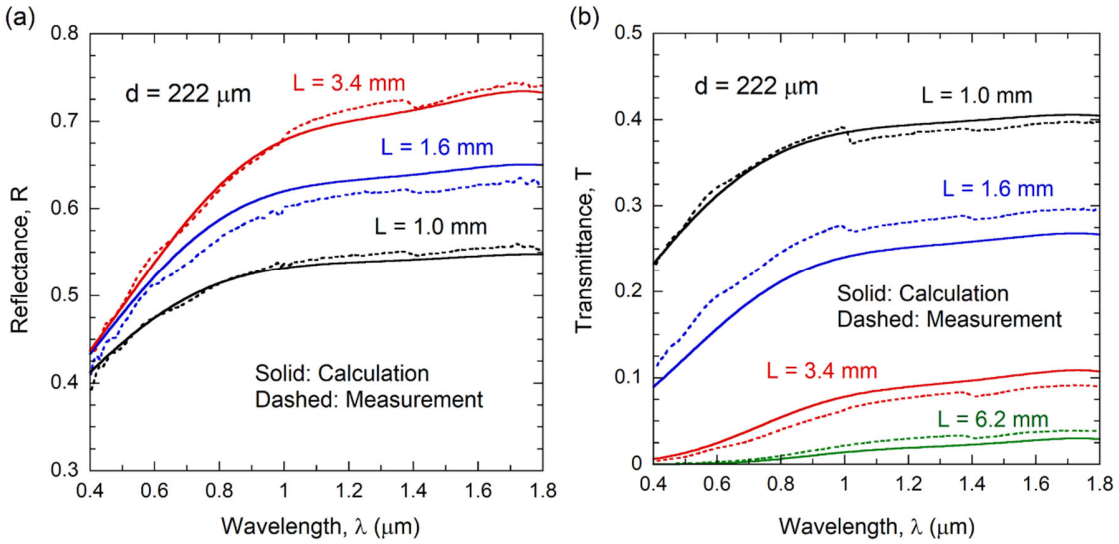

Figure 4.4. Measured and modeled radiative properties of packed beds for Type A particles (d = 222 μm) with different thicknesses: a) reflectance; b) transmittance.

The measurements exhibit some discontinuities about λ = 1 μm due to the switching between the Si and Ge photodetectors and associated filter and grating sets. A dip is observed near λ = 1.4 μm in both T and R, presumably due to defect absorption of these particles. Deviations between the measured and calculated results are mainly attributed to sample-to-sample variations, experimental uncertainties, and regression errors. The root-mean-square deviations (RMSD) between the measurement and calculation are 0.031 in T with L = 1.6 mm, and 0.016 if the R and T for all thicknesses are considered. In general,

both R and T decrease towards shorter wavelengths, indicating a strong absorption by impurity especially for $\lambda < 1$ μm. The R for $L = 6.2$ mm is very close to that for $L = 3.4$ mm and is, therefore, not shown in Figure 4.4 (a). As shown in Figure 4.4 (b), T for the $L = 6.2$ mm bed is negligibly small in the visible region and less than 8% for λ up to 1.8 μm. For $L = 1$ mm at $\lambda = 0.4$ μm, $R \sim 0.41$ and $T \sim 0.23$, resulting in an absorptance ($1 - T - R$) of 0.36. In the visible region, increasing L gives rise to an increase in R with a faster decrease in T. The net result is an increase in the absorptance as L increases until the packed bed becomes opaque.

Similar results for Type B and C particles are shown in Figure 4.5.

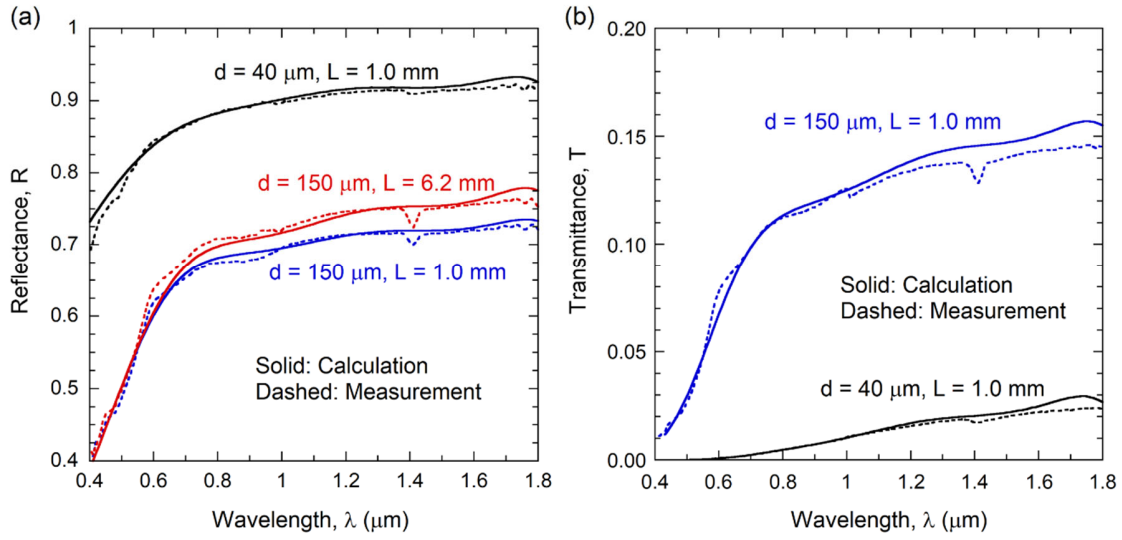

Figure 4.5. Measured and modeled radiative properties of packed beds for Type B and C particles ($d = 150$ μm and 40 μm): a) reflectance; b) transmittance.

For Type B, R slightly increases from $L = 1$ mm to $L = 6.2$ mm, as shown in Figure 4.5 (a). For Type C particles, R is only shown for $L = 1.0$ mm because it is essentially the same for $L = 6.2$ mm. For smaller sized particles, T is very low even with $L = 1$ mm, as shown in Figure 4.5 (b). Both R and T increase quickly from $\lambda = 0.4$ μm to 0.8 μm. Note

that *R* for Type C is much higher than that for Type A and B due to the stronger scattering effect with smaller particles. The RMSD is ≤ 0.01 with Type B and C particles.

The absorption and reduced scattering coefficients calculated using the polynomial coefficients listed in Table 4.1 are plotted in Figure 4.6 (a) and 4.6 (b), respectively.

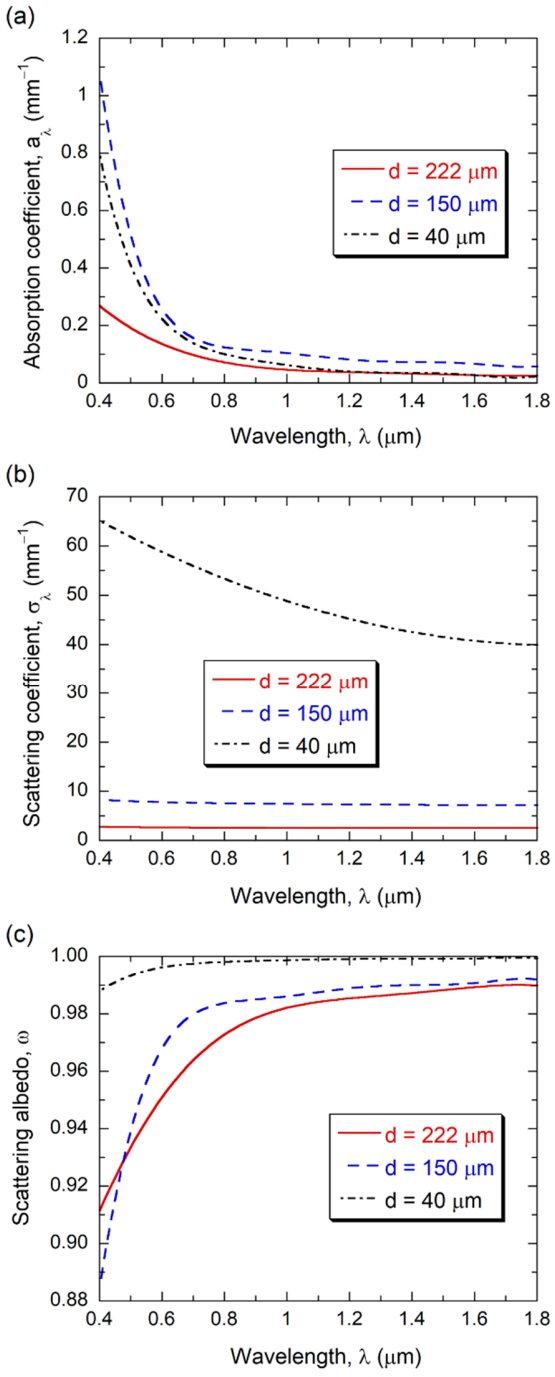

Figure 4.6. Parameters retrieved from the IAD method for the three types of particles: a) absorption coefficient; b) reduced scattering coefficient; c) scattering albedo.

For all three types of particles, a_λ increases rapidly towards shorter wavelengths. The relatively large values for Type B particles (d = 150 μm) indicate that Type B particles possess more impurities than Type A and C particles. The absorption coefficient for Type C particles is almost the same as for Type A particles for 1.2 μm < λ < 1.8 μm but much larger towards the shorter wavelengths. At λ = 0.4 μm, a_λ = 0.28 mm^{-1} and 0.8 mm^{-1} for Type A and C particles, respectively, even though the intrinsic properties of the particles for Type A and C are the same. As seen from Figure 4.6 (b), σ_λ is almost independent of the wavelength for Type A and B; however, it increases towards shorter wavelengths for Type C and is much larger than those of Type A and B. The IAD solutions inherently account for any dependent scattering effects or wave effects, though it does not treat them separately. The effect of dependent scattering will be addressed in Sec. IV.

The magnitude of σ_λ is 2 to 3 orders of magnitude higher than a_λ. The scattering albedo $\omega = \sigma_\lambda / (a_\lambda + \sigma_\lambda)$ is shown in Figure 4.6 (c) with a scale minimum of 0.88. ω increases towards longer wavelengths and reaches 0.98 with Type A and B particles. With Type C particles, $\omega \approx$ 0.99 at λ = 0.4 μm and increases to 0.999 at λ = 1.8 μm. The implication of the effective absorption and scattering properties is that a forward calculation may be employed to model radiative transfer in packed beds of similar particle type and volume fractions for the calculation of solar absorptance and effective conductivity of densely packed beds [22-24].

4.2.3 Monte Carlo Simulation

Comparison results are shown in Figure 4.7 for all samples with the Monte Carlo simulation (model) shown as solid lines and experiments as dashed lines.

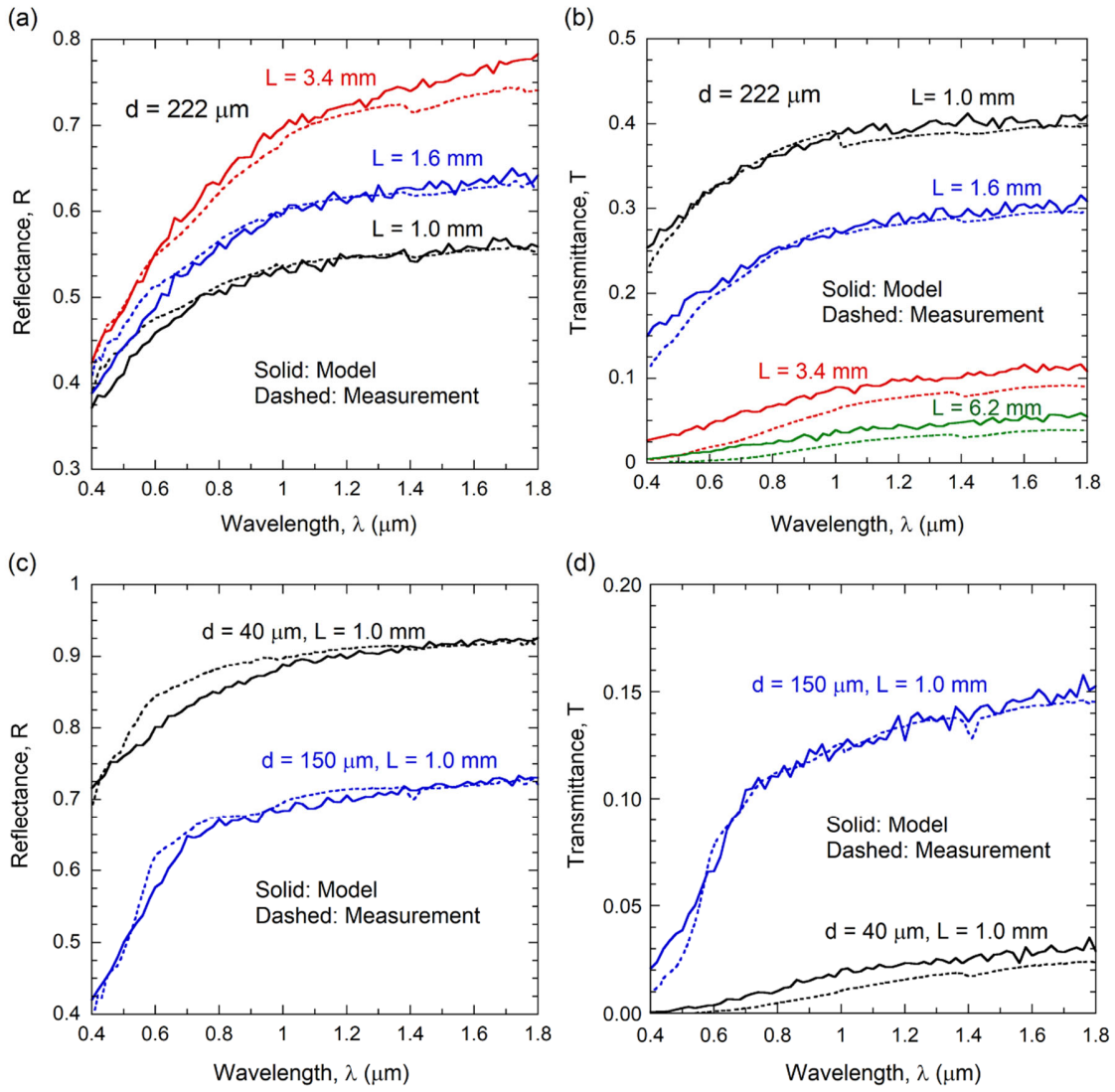

Figure 4.7. Measured and modeled radiative properties of the particle beds using the Monte Carlo method for L = 1.0 mm: a) reflectance for Type A; b) transmittance for Type A; c) reflectance for Type B and C; d) transmittance for Type B and C.

Since R for L = 6.2 mm with Type A is very close to that for L = 3.4 mm, it is not shown. Some fluctuations is observed in the model due to statistical noise. The RMSD between the model and experiment is typically ~ 0.02, which is comparable with the

experimental and numerical uncertainties. However, the model overpredicts T when the measured transmittance is relatively low. The reason is attributed to the blockage and additional scattering by polydispersed particles with shape irregularities in the actual packed bed that is not fully captured by the Monte Carlo model. Despite the simplifications, the discrete-scale Monte Carlo model allows quantitative prediction of the radiative properties in the visible and near-infrared region.

The Monte Carlo method is also used to model R up to $\lambda \approx 15$ μm using the previously obtained S. Only the cases of $L = 6.2$ mm are measured with FTIR at longer wavelengths. The measurement and model are compared in Figure 4.8. As previously seen from Fig. 3, due to the competing effect of absorption and scattering by particles of different sizes, R is similar for Type A and B when $\lambda < 1.8$ μm. Whereas smaller particles tend to scatter more and produce higher reflectance, the absorption in Type B particles are stronger due presumably to the additional impurities. For $2.7\ \mu\text{m} < \lambda < 5\ \mu\text{m}$, the absorption bands of α-quartz are rather complicated [124, 129]. For this reason, the value of κ is slightly adjusted for Type A to achieve a better agreement in R between the model and measurement. These values are used for Type B and C due to insufficient information or reasoning necessary to fine tune the parameters for matching. The trend correlates well between the model and measurement as shown in Figure 4.8 (b) and (c).

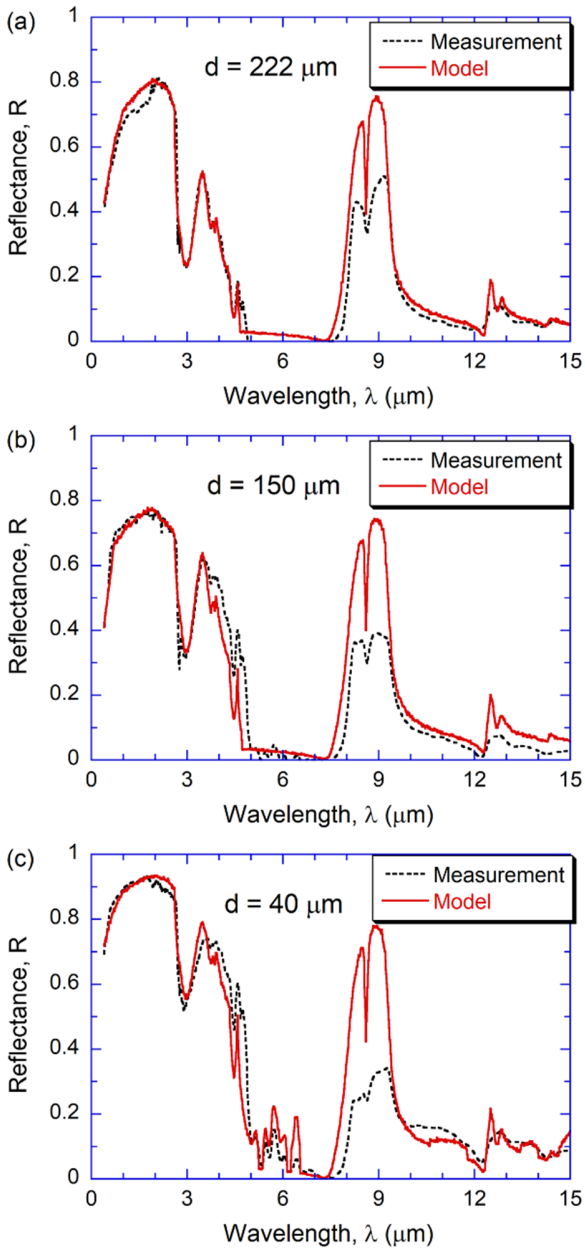

Figure 4.8. Measured and modeled reflectance of SiO_2 particle beds using the Monte Carlo method for L = 6.2 mm: a) Type A; b) Type B; c) Type C.

Another notable feature is that, in the phonon resonance band between 8 μm and 10 μm, the model produces a much higher R that is almost independent of the particle size. Based on the geometric optics, because the SiO_2 particle is opaque in this region (the photon penetration depth is less than 2 μm), scattering occurs by surface reflection in the

top few layers until the beam is completely blocked. Multiple reflections occur on rough or curved surfaces that enhance absorption via the cavity effect [28, 85, 106]. The monodispersed spheres used in the Monte Carlo model do not represent the actual geometry very well. Other effects (*e.g.*, the effective graded index near the surface and wave interference) are not included in the Monte Carlo model [64]. Some of the features beyond $\lambda > 10$ μm observed in the experiments are similar to the model. For Type C, the diameter is comparable to wavelength where Mie scattering plays an integral role. In general, due to irregular shapes of particles and polydispersed packing condition, the simple Monte Carlo model only achieves qualitative agreement in the mid-infrared. Nevertheless, it helps explain the absorption effect and trend of reflectance in this region. Note that the effect of poly-dispersion on the radiative transfer has recently been considered by a multiphase radiative transfer model in which particle groups within specified size intervals are treated as individual components [132].

4.3 Effect of Dependent Scattering

While the Monte Carlo method is a direct approach to obtain radiative properties of particle beds, it requires much computational resources that could be hard to meet especially when dealing with conjugated heat transfer problems. In addition, the physical representation of the particle bed in a Monte Carlo model is usually simplified to obtain qualitative results. The IAD calculation provides an easy access to the absorption and scattering characteristics, which is favored by available forward solutions of RTE. However, the experimental results (reflectance and transmittance) that are the inputs to IAD are not always available. Therefore, it is useful to examine whether single particle

properties, which are generally available in various literatures or are relatively easy to calculate, can be used to approximate overall absorption and scattering characteristics of the packed bed. The absorption and scattering properties, including phase function, of a single particle can be obtained via the Monte Carlo method [76]. By summing up forward scattered and backscattered rays, the scattering efficiency can be calculated, and the absorption efficiency is obtained by subtracting it from unity.

Following the independent theory (Sec. 2.2.2), the a_λ and σ_λ are calculated for particle beds based on their volume fraction and particle size. The phase function is also determined from the Monte Carlo method using the angular information of scattered photon bundles and fitted to an HG phase function to obtain the asymmetry factor *g*. To compare with the IAD, the anisotropic (or true) scattering coefficient is multiplied by (1 – *g*) to obtain the reduced (isotropic equivalent) scattering coefficient, as listed in Table 4.2. The absorption coefficient from the model is obtained from Eq. (2.2) and listed in Table 4.2 at three wavelengths. The model gives results for independent scattering while the IAD takes into consideration any dependent scattering effect

Table 4.2. Absorption coefficient and reduced scattering coefficient obtained from independent scattering model and from experiments using IAD, along with the calculated transmittance and reflectance using AD for a 1.0 mm thickness particle bed.

Type	λ (μm)		a_λ (mm^{-1})	σ_λ (mm^{-1})	R	T
A	0.7	Model	1.15E-01	2.61	0.485	0.329
		IAD	9.78E-02	2.61	0.498	0.341
	1	Model	4.77E-02	2.64	0.538	0.377
		IAD	4.65E-02	2.56	0.532	0.385
	1.7	Model	2.01E-02	2.63	0.561	0.401
		IAD	2.55E-02	2.54	0.547	0.406
B	0.7	Model	1.76E-01	5.31	0.587	0.145
		IAD	1.57E-01	7.66	0.660	0.099
	1	Model	1.24E-01	5.35	0.625	0.168
		IAD	1.04E-01	7.43	0.695	0.125
	1.7	Model	7.16E-02	5.40	0.671	0.197
		IAD	5.87E-02	7.19	0.732	0.156
C	0.7	Model	1.53E-01	24.48	0.798	0.015
		IAD	1.39E-01	55.98	0.867	0.002
	1	Model	6.65E-02	24.54	0.858	0.032
		IAD	6.25E-02	48.85	0.902	0.010
	1.7	Model	2.64E-02	24.52	0.898	0.049
		IAD	1.97E-02	40.23	0.932	0.029

In addition to comparing the values of a_λ and σ_λ, the resulting T and R for L = 1.0 mm with different particle sizes are calculated and compared in Table 2 at λ = 0.7 μm, 1.0 μm, and 1.7 μm. The agreement is very good for Type A albeit some differences in a_λ, indicating that dependent scattering effect is negligible and independent scattering model can produce reasonable results. For Type B, the model overpredicts 10-20% in a_λ and underpredicts 30-40% in σ_λ, resulting in an absolute error of about –0.07 in R and +0.04 in T. At λ = 1 μm, the relative error in T is 34%. For Type C, the model overpredicts 10-25% in a_λ and underpredicts 60-130% in σ_λ. At λ = 1 μm, the model yields a σ_λ that is nearly half of the IAD. However, for L = 1 mm, the measured T is nearly zero and R exceed 0.86, the model yield a lower reflectance with a relative error of 4-9% and a much higher transmittance. The ratio of transmittances calculated by AD using a_λ and σ_λ from the model and from the IAD is 7.5, 3.2, and 1.7 at λ = 0.7 μm, 1.0 μm, and 1.7 μm, respectively. It becomes clear that dependent scattering is significant for Type B particles and even stronger for Type C. The impact of dependent scattering in Type B particles mainly results from the geometric multiple scattering. For Type C, the modeled σ_λ is only a weak function of λ, while the σ_λ obtained from IAD tends to increase rapidly toward shorter wavelength; this is a wave scattering effect which generally predicts a stronger scattering toward short wavelengths. As shown in Figure 4.1 (c), Type C particles contains smaller sized fragments or voids that could give rise to such wave scattering effect.

CHAPTER 5

TEMPERATURE-DEPENDENT SPECTRAL EMITTANCE OF BAUXITE AND SILICA PARTICLE BEDS

This chapter provides an experimental investigation of the temperature-dependent emittance of bauxite and silica particle beds. A high-temperature emissometer is developed and tested with a fused silica disc and compared with literature to ensure accuracy. A Lorentz oscillator model is used to fit the emittance and the temperature-dependent damping effect of the infrared phonon modes are investigated. The measured emittance for bauxite particle beds is integrated over Planck's distribution to obtain the overall emittance at corresponding temperatures.

5.1 Metrology and Validation

5.1.1 Emissometer Setup

The measurement apparatus consists of a sample chamber, a blackbody cavity, several windows and mirrors, and an ABB FTLA2000 Fourier-transform infrared spectrometer (FTIR), as shown in Figure 5.1 (a). A side view of the sample chamber is shown in Figure 5.1 (b), and a photo of the setup is shown in Figure 5.2. This setup is a modified design of the previous setup for measuring the emittance of flat plate samples [37]. The particles in the packed bed are positioned horizontally placed to directly measure the emission signal from the heated particles. A quartz plate covers a horizontally placed electric heater, which is embedded in the refractory insulation with a cylindrical opening pocket. A flat Cu crucible sits in the pocket on the quartz plate. A side hole was drilled into

the base of the crucible and a thermocouple was inserted through the insulation all the way to the center of the crucible without toughing the particles.

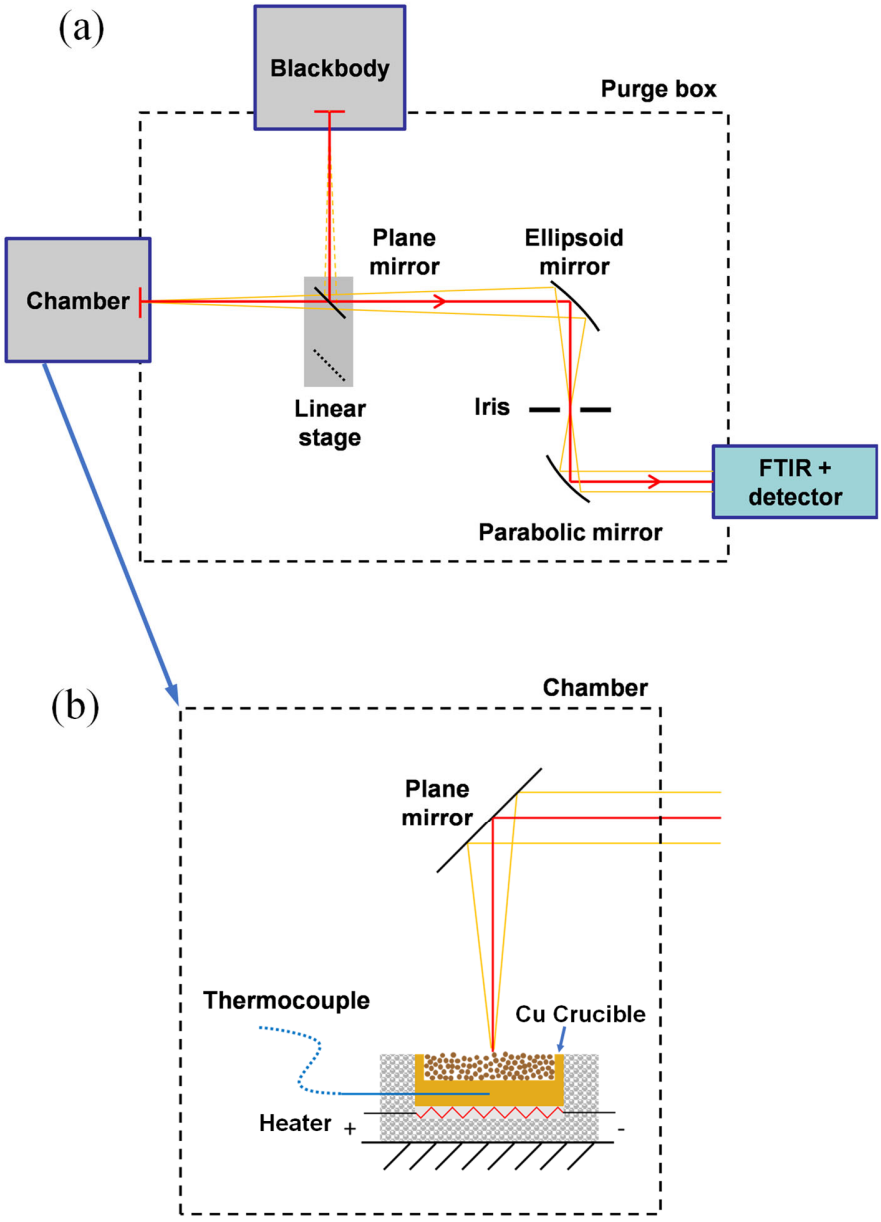

Figure 5.1. Schematic of the high-temperature emissometer setup (not to scale). (a) Top view of the optical layout; (b) side view of the sample chamber.

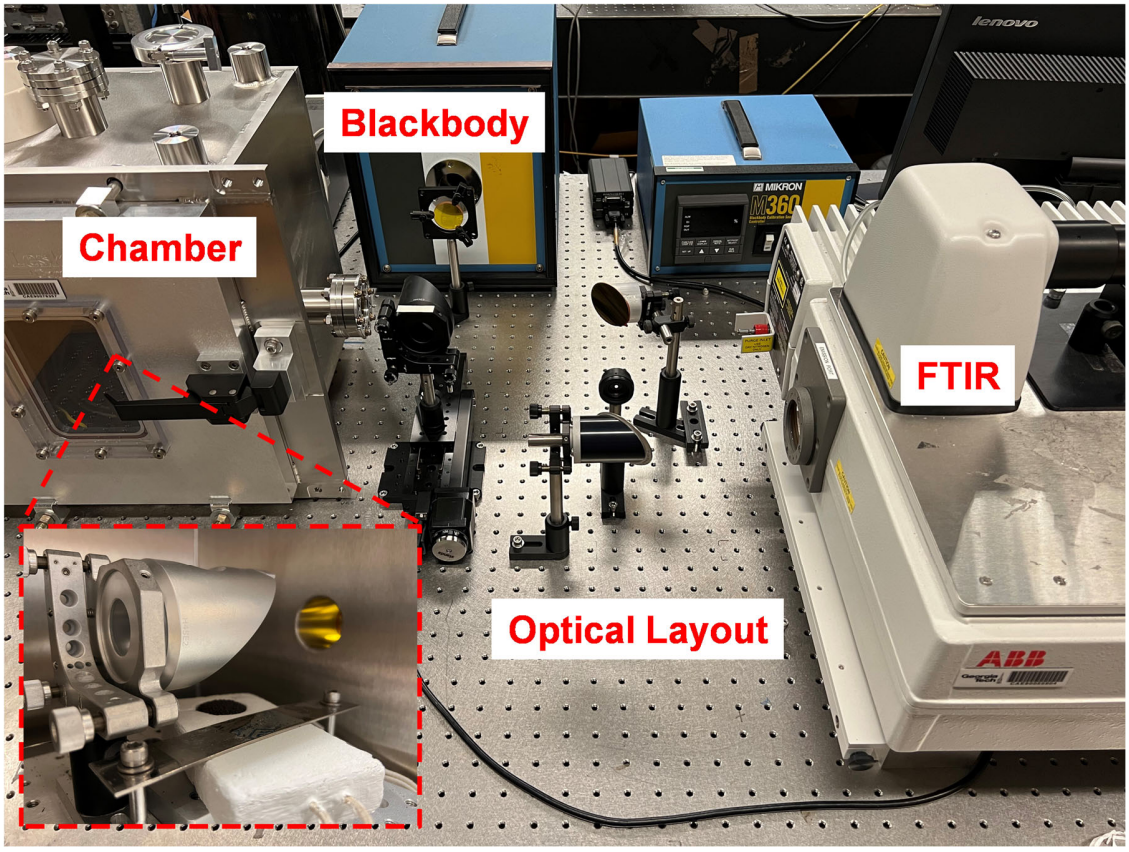

Figure 5.2. Photo of the high-temperature emissometer setup.

The crucible holds either the particle beds or a bulk disc with a diameter of approximately 25 mm and a depth of 2–5 mm. The particles in the bed were lightly compressed by a flat surface to remove any unevenness. The sample stage is enclosed in a stainless-steel chamber with a transparent ZnSe window for emission output. For optical equivalency, a ZnSe window was also placed in front of the blackbody box (not shown in Figure 5.1 (a). The chamber shields the sample from air current disturbances and provides a stable environment. The normal thermal emission signal (with a half cone angle of 3°) is reflected by the 45° angle plane mirror atop the sample to form a horizontal beam, which is then sent through the ZnSe window to the elliptical mirror. The second focus of the elliptical mirror is at the iris. The beam expands after the iris to the parabolic mirror and is

reflected as a collimated beam into the FTIR through a build-in ZnSe window on the side (emission) port.

The optical components are enclosed by an acrylic box and purged with nitrogen gas to diminish the effect of spectral absorption lines by $H_2O(v)$ and CO_2. A plane mirror is mounted on a motorized linear translation stage, which moves the mirror in and out of the optical path to switch the emission source between the blackbody and the sample when needed. The optical path from the sample to the FTIR and that from the blackbody to the FTIR were designed to be equal with identical number of transmissions and reflections. The various mirrors in the optical path were coated with Au film to achieve high infrared reflectance and long-term stability. The iris placed between the ellipsoid mirror and the parabolic mirror eliminates out-of-focus irradiation. The spectral range of the FTIR measurements is 1 μm < λ < 19 μm with a deuterated triglycine sulfate (DTGS) detector and ZnSe windows.

The optical system was aligned with a laser pointer placed horizontally. It sends a red light reversely through the parabolic mirror, iris, ellipsoidal mirror, and then to the sample surface (or the blackbody opening). The plane mirrors mounted on the linear stage and above the heated sample merely alter the irradiation direction, while maintaining the same total path length and optical efficiency from the sample (or the opening of the blackbody) to the ellipsoid mirror. When the laser sends a collimated beam to the parabolic mirror, a small spot is expected to show at the location of the sample surface (or the blackbody opening) and is visible by blocking the light path with a white paper. Despite carefully design and alignment efforts, imperfect positioning of the mirrors, FTIR, sample holder, and the blackbody may result in some optical inequivalence. In addition, there is a

relatively large temperature gradient within the sample, especially with the particle bed. The emission signal comes from not only the top layer of the particles but also the adjacent particle layers due to light scattering. This also causes optical inequivalence as the optical design shown in Figure 5.1 (a) presumes that the emission is from the sample surface. The aperture size of the iris may also influence the measurements. A large aperture improves the signal-to-noise ratio but at the same time gives rise to misalignment that deteriorates the optical equivalence. A trade-off must be made and the final aperture diameter is approximately 3 mm. Overall, a 10–15% inequivalence should be expected. A post-processing method that uses a correction factor is developed and will be explained in the data analysis section.

A Mikron M360 blackbody with a 25 mm aperture diameter was used as the reference source with a temperature accuracy of $\pm$ 1 K and a stability of $\pm$ 0.5 K. A PID controller regulates the blackbody temperature. The system produces thermal emission with nearly 99.99% of the blackbody limit. An example of the measured blackbody spectra, $S_{\mathrm{BB}}(\lambda,T)$ at T = 473 K, 673 K, and 873 K (200 °C, 400 °C, and 600 °C), respectively, is shown in Figure 5.3.

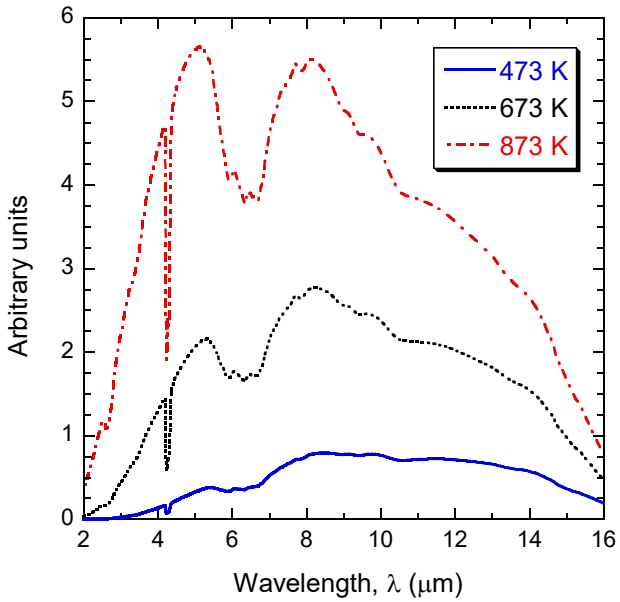

Figure 5.3. Measured blackbody signal spectrum at blackbody temperatures of 473, 673, and 873 K.

The spectral resolution of the FTIR was set to 4 cm^{-1}. The results were averaged for 512 scans with additional piecewise data smoothing process to remove noise. The signal strength is very low for $\lambda < 2$ μm and $\lambda > 16$ μm, especially at relatively low temperatures. Therefore, the measured spectrum was truncated to 2 μm ≤ λ ≤ 16 μm with reasonable spectral response. The signal unit is arbitrary and it does not affect the final result because the emittance is obtained from the ratio of the sample signal to the blackbody signal at the same temperature. Due to the wavelength dependence of the detector response, optics, and signal processing method in the FTIR measurements, the peak wavelength in the measured spectra does not correspond to the prediction by Wein's displacement law. A broadband $H_2O(v)$ absorption in the region 5 μm < λ < 8 μm is observed and becomes more significant at elevated temperatures. There appears to be a narrowband absorption line about 4.3 μm due to the presence of CO_2, causing significant signal drop. When reporting the measured

emittance, the artifact associated with the spectral absorption line near 4.3 μm was removed through post-processing.

The crucible temperature, T_{cru}, measured by the inserted thermocouple is always higher than the surface temperature of the particle bed due to the low thermal conductivity of the particles and contact resistances [24]. Nevertheless, T_{cru} provides an indication of the sample temperature and was used as a set point to control the heater with a PID temperature controller using LabView. During the measurement, the crucible was set to T_{cru} = 200 °C, 400 °C, and 600 °C. Because the exact emission location and temperature profile of the sample are unknown, an effective sample temperature T needs to be determined so that the spectral emittance of the sample is calculated from the ratio of the sample signal to the blackbody signal at the wavelength and same temperature. The details are to be discussed in the Sec. 5.1.2. The stainless-steel sample chamber may operate under evacuated condition with a pressure below 10^{-4} Pa to minimize convective heat loss. However, it was found that free convection helps improve temperature uniformity in the particle beds. Therefore, all measurements were performed at ambient pressure condition to obtain the sample emission signal, $S(\lambda,T)$.

The FTIR was also used for measuring the specular reflectance (at 10° incidence) of the fused silica disc at room temperature when using the internal Globar (SiC) source with proper accessories [133]. For the particle beds, an integrating sphere was used to measure the room-temperature directional-hemispherical reflectance with the FTIR [95, 118]. The emittance at room temperature was calculated from the reflectance in the opaque region. The uncertainty in emittance at room temperature was estimated based on the reflectance measurements to be 0.02 for silica disc and 0.03 for particle beds. The lab

temperature is typically 22–25 °C. It is expected that a small temperature change will not affect the radiative properties of the sample. Hence, the room temperature is indicated as 300 K throughout this paper.

5.1.2 Data Analysis

The normal emittance of the sample is determined from the measured quantities using the following equation:

$$\varepsilon(\lambda,T)=\frac{1}{F_{\mathrm{C}}}\frac{S(\lambda,T)-S_0(\lambda)}{S_{\mathrm{BB}}(\lambda,T)-S_{\mathrm{BB},0}(\lambda)} \tag{5.1}$$

where, $S(\lambda,T)$ and $S_{\mathrm{BB}}(\lambda,T)$ are the sample and blackbody emission signals at the same temperature, respectively, $S_0(\lambda)$ and $S_{\mathrm{BB},0}(\lambda)$ are the background signals when the sample and blackbody are at the ambient temperature, and F_{C} is a correction factor to account for the inequivalence between the optical paths during the measurements. Ideally, F = 1; however, due to imperfect alignment and varying properties of the mirrors and windows, an inequivalence exists between the optical paths that must be considered. In practical situations with the room-temperature DTGS detector, S_0 and $S_{\mathrm{BB},0}$ are negligibly small compared with the emission signals at T > 450 K and hence are ignored hereafter.

As mentioned previously, due to low thermal conductivity of the particle beds (0.25–0.50 W/m·K) [24] and the contact thermal resistance between the particles and the Cu crucible, a relatively large temperature gradient is present in the particle bed. Furthermore, the temperature near the surface of the particle bed cannot be accurately measured by attaching the thermocouple to the particles. Due to the unknown emittance of

the particle bed surface, pyrometer measurements also yield a large uncertainty. Therefore, the effective sample temperature T is determined using the following procedure.

Because the temperature of the sample is treated as an unknown, this presents some challenges in setting the blackbody to be at the same temperature. In the measurements, the blackbody emission spectra are taken at several discrete temperatures. Interpolation is needed to determine the blackbody spectrum at a given temperature T using the measured emission spectra at T_1 and T_2. with $T_1 < T < T_2$. However, a simple linear interpolation results in a large uncertainty and even changed the spectral characteristics. Assume $S_{\mathrm{BB}}(\lambda,T)$ is proportional to the spectral intensity $I_{\mathrm{b},\lambda}(\lambda,T)$ given by Planck's distribution. A proper interpolation formula reads:

$$\frac{S_{\mathrm{BB}}(\lambda,T)-S_{\mathrm{BB}}(\lambda,T_1)}{S_{\mathrm{BB}}(\lambda,T_2)-S_{\mathrm{BB}}(\lambda,T_1)}=\frac{I_{\mathrm{b},\lambda}(\lambda,T)-I_{\mathrm{b},\lambda}(\lambda,T_1)}{I_{\mathrm{b},\lambda}(\lambda,T_2)-I_{\mathrm{b},\lambda}(\lambda,T_1)} \tag{5.2}$$

This relationship holds as long as the detector spectral response is linear and consistent. Eq. (5.2) was validated by measuring the blackbody emission spectra at three different temperatures. If the right-hand side of Eq. (5.2) were replaced by $(T-T_2)/(T_1-T_2)$, the result would not be acceptable.

For oxide materials, the emittance (or absorptance) is very close to 1 at the Christiansen wavelength, λ_{Ch}, which is typically in the mid-infrared where the refractive index is approximately equal to 1 [106]. Based on Eq. (5.1), if the background signals are neglected and $\varepsilon(\lambda_{\mathrm{Ch}},T)=1$, then,

$$S(\lambda_{\mathrm{Ch}},T)=F_{\mathrm{C}}S_{\mathrm{BB}}(\lambda_{\mathrm{Ch}},T) \tag{5.3}$$

In Eq. (5.3), $S_{\mathrm{BB}}\left(\lambda_{\mathrm{Ch}}, T\right)$ is evaluated using Eq. (5.2) and taken as a known quantity at prescribed temperature. If F_{C} is known, Eq. (5.3) enables the determination of the sample temperature *T*. In the setup used, F_{C} varies from 1.10 to 1.15 and is somewhat sample dependent. Additional information about the spectral shape or multiple peaks was used to evaluate F_{C}. An iterative procedure is used to determine both F_{C} and *T*. F_{C} was guessed and used as the trial value. Then *T* is determined from Eq. (5.3) by solving the combined equations. The spectral shape or peaks were analyzed to further tuning F_{C} until satisfactory agreement is achieved. For the fused silica disc and silica particle bed, the Christiansen wavelength is at λ_{Ch} = 7.30 μm. $F_{\mathrm{C}} = 1.15$ was obtained by comparison of the measured spectra with the literature for fused silica [34]. For the bauxite particles, based on both room-temperature and high-temperature measurements, the emittance is close to 1 in a broad spectral region due to multiple phonon oscillators in the composite material [95]. $F_{\mathrm{C}} = 1.11$ was obtained from the broadband emittance peak observed for one type of particles, specifically, Carbobead CP 30/60 at room temperature. Once determined, F_{C} is kept constant throughout the measurements for other bauxite particle beds. Due to the temperature nonuniformity and inequivalence, the overall uncertainty of the direct emittance measurements was estimated to be 0.03 for fused silica disc and 0.05 for all particle beds.

5.1.3 Validation with a Fused Silica Disc

A fused silica disc was chosen to test the emissometer and the method of temperature determination and alignment correction. The disc is 25 mm in diameter and 3

mm in thickness. The room-temperature reflectance and transmittance of the disc were measured using the FTIR with its internal emission source. The normal-normal transmittance and specular reflectance at 10° were measured. Since the disc is smooth, the measured properties are essentially directional-hemispherical. The measured room-temperature reflectance R and transmittance T are used to determine the room-temperature emittance from $\varepsilon = 1 - R - T$. The Christiansen wavelength is determined as λ_{Ch} = 7.30 μm.

For high-temperature emittance measurements, with λ_{Ch} = 7.30 μm and $F_{\mathrm{C}} = 1.15$, the surface temperature of the fused silica disc is obtained as T = 446 K, 610 K, and 769 K at the set point of the crucible T_{cru} = 473 K, 673 K, and 873 K, respectively. The large temperature difference is principally caused by the contact resistance, in addition to the temperature gradient in the fused silica. The measured emittance spectra are shown in Figure 5.4 (a) at $\lambda > 5$ μm.

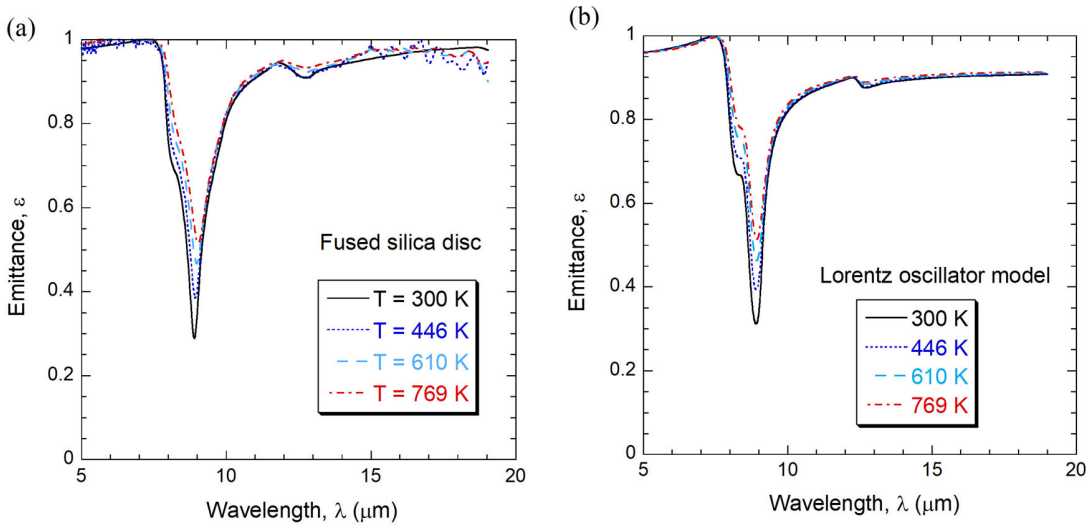

Figure 5.4. Temperature-dependent emittance of a 3-mm-thick fused silica disc compared with predictions using optical constants from Lorentz oscillator model for T = 300, 446, 610, and 769 K. (a) measurement; (b) modeling results.

Because the fused silica is semitransparent at $\lambda < 5$ μm, the emission signal in short wavelength region is dominated by thermal emission from the Cu crucible surface. The emittance for 300 K is calculated from the room-temperature reflectance based on Kirchhoff's law using $\varepsilon = 1 - R$, where $(1 - R)$ is the absorptance since only the opaque region is of interest. The temperature-dependent phonon structure yields an increase of emittance as the temperature is increased. This effect was observed by Rozenbaum et al. [34] and explained by the associated increase in the damping coefficient of the phonon with a resonance frequency of 1100 cm^{-1} (9.1 μm). To quantify such effect, the measured emittance spectra were fitted to a Lorentz oscillator model (Sec. 2.3.1) using Eq. 2.11 with three oscillators in the present study.

Table 5.1. Parameters in the Lorentz oscillator model obtained by fitting the emittance of fused silica disc. The sample temperature is in parentheses. Note that $\varepsilon_\infty = 2.568$.

	Ambient (300 K)	T_{cru} = 473 K (T = 446 K)	T_{cru} = 673 K (T = 610 K)	T_{cru} = 873 K (T = 769 K)
ω_1	799.1	799.1	799.1	799.1
S_1	0.034	0.031	0.026	0.020
γ_1	34.49	32.48	35.90	32.48
ω_2	1100	1100	1100	1100
S_2	0.585	0.553	0.513	0.483
γ_2	22.95	30.07	36.02	41.06
ω_3	1188	1188	1188	1188
S_3	0.099	0.105	0.111	0.103
γ_3	87.82	89.59	94.68	92.30

It is difficult to model the dielectric function of SiO_2 in the mid-infrared due to multiple resonances [130], though a simple Lorentz model with only two oscillators was used to capture the resonance feature at 1100 cm^{-1} and 460 cm^{-1}, respectively [134]. In the present study, since the spectral region of interest is 5 μm < λ < 18 μm, three oscillators with $\omega_1 =$ 779.1 cm^{-1}, $\omega_2 = 1100$ cm^{-1}, and $\omega_3 = 1188$ cm^{-1} were used based on the least-squares fitting at room temperature. $\varepsilon_\infty = 2.568$ was also obtained from fitting the room-temperature result. This is slightly higher than those based on n^2 of fused silica, which is near 2.1 at λ < 1 μm [128]. The resonance frequencies and ε_∞ are assumed to be independent of temperature. Only the strength and damping coefficients of the three oscillators are tuned to fit the emittance at elevated temperatures. The best-fitted parameters are listed in Table 5.1, and the predicted emittance spectra are displayed in Figure 5.4 (b) at the corresponding temperatures. Although the fitting has uncertainties associated with the experiments and the model itself, the Lorentz model captures the main features and the temperature dependence of emittance when comparing Figure 5.4 (a) and (b). As expected, the main change in the oscillator parameters comes from the damping coefficient γ_2, which has a nearly twofold increase from T = 300 K to 769 K. This is the main reason for the reduction of emittance in the region $8\ \mu m < \lambda < 10\ \mu m$ as temperature increases. The trend and magnitude of measured emittance of fused silica are in qualitatively agreement with those reported in [34] at high temperatures.

5.2 Results and Discussion

5.2.1 Particle Sample Description

Two types of particles were investigated, and their microscopic images are shown in Figure 5.5.

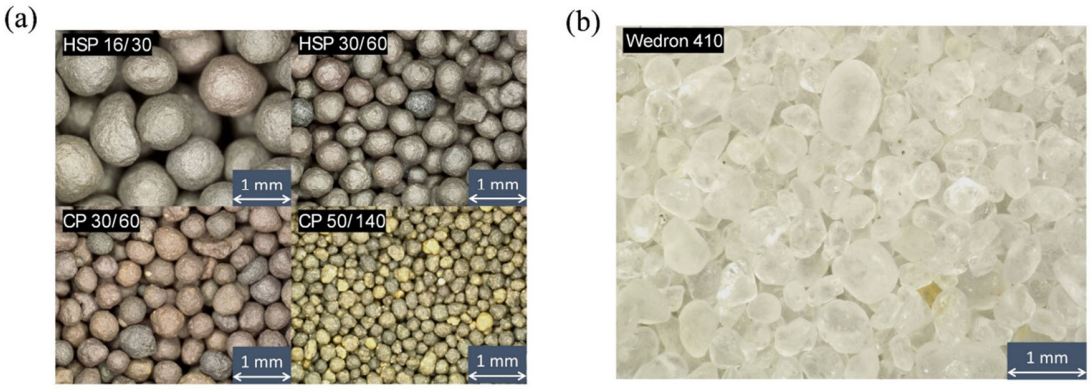

Figure 5.5. Microscopic images of the particle beds used in the present study. (a) Four types of bauxite particles; (b) Wedron 410 polycrystalline silica particles.

All particles are nearly spherical with some surface irregularities and size variation. The polycrystalline silica particles (Wedron 410 from Wedron Co.) have an average diameter d = 222 μm and a purity of 99.65% [76]. The silica particles appear to be clear and transparent with impurities that affect the absorption in the visible and semitransparent region [30]. The bauxite or alumina-silica particles are Carbobead manufactured by Carbo Ceramic Co. They are composed of Al_2O_3, TiO_2, SiO_2 and Fe_2O_3 with somewhat different mass fractions and porosity. The average diameters of CP 30/60 and CP 50/140 are 453 μm and 194 μm, respectively, and those of HSP 30/60 and HSP 16/30 are 495 μm and 956 μm, respectively. The Carbobead particles appear dark to the naked eye under regular lighting conditions, unlike what the images from the microscope show. Detailed description and the measurement of the radiative properties of the bauxite particles are

available in [95]. The thickness of the packed bed is approximately 3 mm for all particles contained in the Cu crucible. Test measurements were also performed for certain particles with varying thicknesses, and it was found that 3 mm thickness is sufficient to achieve complete opacity.

5.2.2 Emittance of the Silica Bed

In a recent work [30], the room-temperature radiative properties for several types of silica particles were measured and modeled. Polycrystalline silica materials are expected to have similar transparent windows like fused silica [128, 135]. The spectral emittance of the Wedron 410 particle bed at various temperatures is shown in Figure 5.6 for $\lambda > 5$ μm, where the packed bed is opaque. Again, the emittance at 300 K was calculated from $1 - R$. Since the MCT detector was used for the room-temperature reflectance measurements, the cutoff wavelength is ~15 μm. For the high-temperature measurements with the DTGS detector, the spectra extend to 16 μm (beyond which the noise is very high). Note that the ordinate begins at $\varepsilon = 0.4$. For the same setting crucible temperatures, the "surface" temperature of the particle bed is 435 K, 583 K, and 713 K, much lower than that with the fused silica disc especially at the highest temperature setting due to the low effective thermal conductivity of the particle bed. There are some fluctuations in the spectra at elevated temperatures, especially for $T = 435$ K due to the low signal-to-noise ratio.

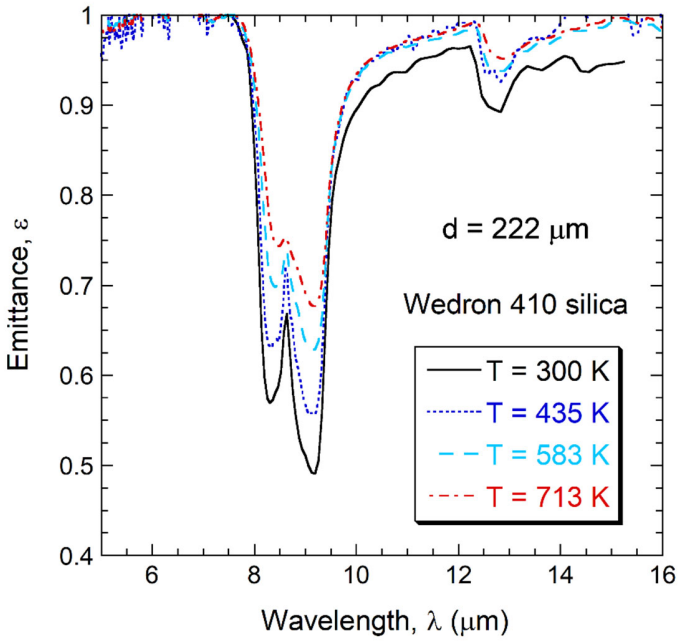

Figure 5.6. Measured temperature-dependent emittance of the silica particle bed (d = 222 μm) for T = 300, 435, 583, and 713 K.

Crystalline silica (often referred to as quartz) is anisotropic with different phonon structures for ordinary and extraordinary rays [135-137]. It is reasonable to expect that the dielectric function of polycrystalline particles is described by the effective medium theory based on the ordinary and extraordinary dielectric functions [95]. Using the model dielectric function, Chen et al. [30] predicted the reflectance of a polycrystalline silica plate. From the room-temperature result, the Christiansen wavelength was determined to be λ_{Ch} = 7.35 μm. The particle bed exhibits a lower reflectance or higher emittance than the quartz plate in the phonon absorption region for $8\ \mu m < \lambda < 10\ \mu m$. As shown in Figure 5.6, the measured emittance of the particle bed in the 8–10 μm region increases as the temperature goes up and the emittance peak at 8.7 μm diminishes towards high temperatures. The observed trend agrees well with the previous studies of α–quartz for ordinary rays [136,

137]. It has been shown that the phonon mode at 1154 cm^{-1} (~8.7 μm) is not observable above 846 K, when quartz changes from α−phase to β−phase.

At λ > 9.5 μm, the measured emittance at elevated temperatures almost overlaps with each other, suggesting weak temperature effects on the emittance in this spectral region. The room-temperature emittance is about 0.03 lower for 9.5 μm < λ < 12.5 μm and 0.05 lower at λ > 13 μm when compared with the average emittance at the three elevated temperatures. The indirect measurement at room temperature used the windowed method is subject to some uncertainties due to the contact conditions between the particles and the window. The difference between room-temperature and high-temperature emittance at longer wavelengths is potentially due to measurement errors from both methods. From a theoretical point of view, a second emittance peak is present at 12.3 μm with ε = 0.98 according to the effective medium theory. This feature is well captured by the high-temperature emittance. The silica bed results provide further evidence that the high-temperature emissometer setup and data processing method are capable of accurately measuring the infrared emittance of particle beds.

5.2.3 Emittance of Bauxite Ceramic Particle Beds

The measured emittance spectra of packed beds are shown in Figures 5.7 and Figures 5.8 for selected CP and HSP particles, respectively, with different sizes.

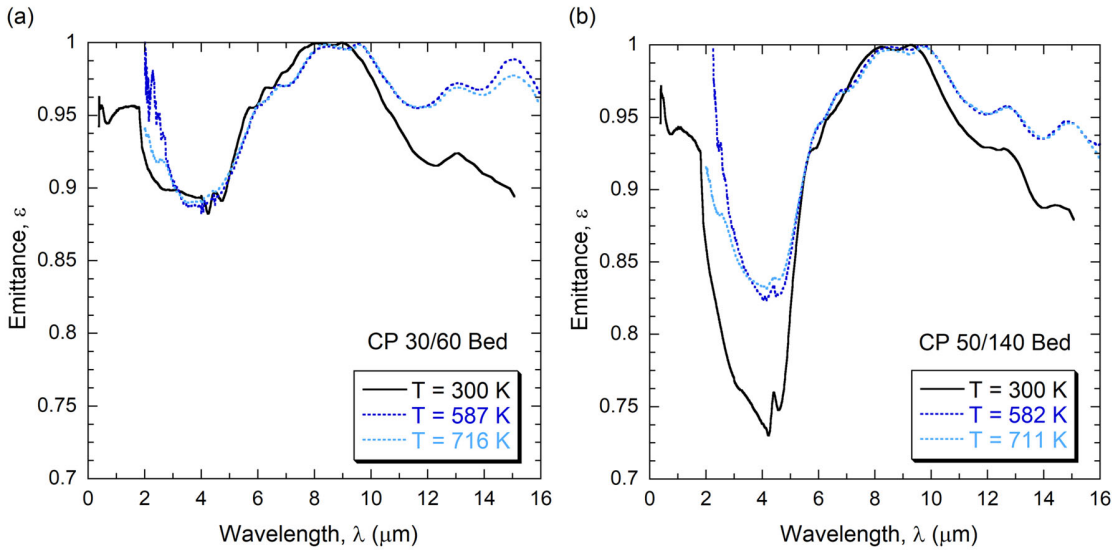

Figure 5.7. Measured temperature-dependent emittance of bauxite particle beds for Carbobead CP particles at various temperatures and sizes. (a) CP 30/60 (d = 453 μm) for T = 300, 587, and 716 K; (b) CP 50/140 (d = 194 μm) for T = 300, 582, and 711 K.

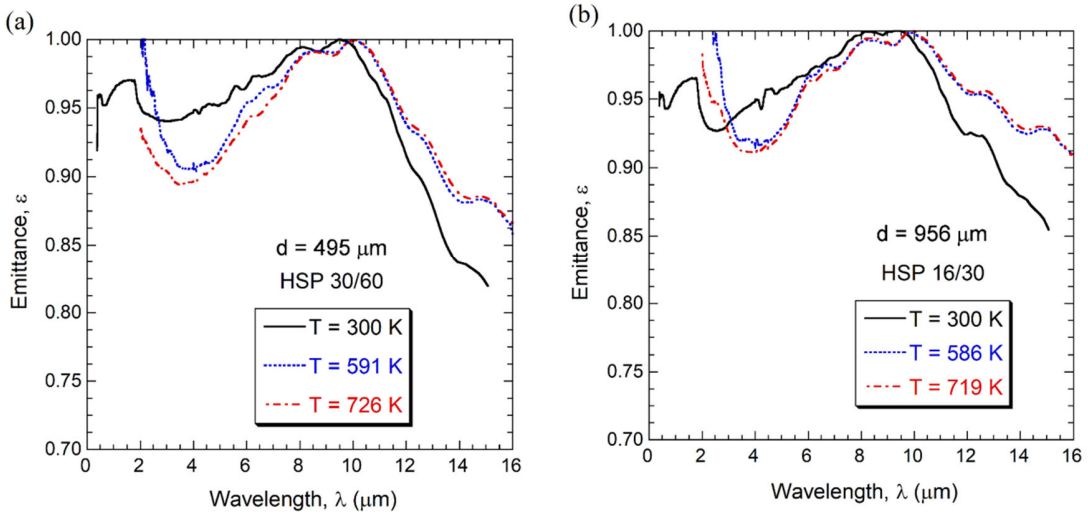

Figure 5.8. Measured temperature-dependent emittance of bauxite particle beds for Carbobead HSP particles at various temperatures and sizes. (a) HSP 30/60 (d = 495 μm) for T = 300, 591, and 726 K; (b) HSP 16/30 (d = 956 μm) for T = 300, 586, and 719 K.

The 300 K results are calculated from the directional-hemispherical reflectance reported previously [95]. Due to the low signal-to-noise ratio in the spectral when $T_{\mathrm{cru}} = 473$ K, high-temperature emittance spectra are plotted only for $T_{\mathrm{cru}} = 673$ K and

873 K for all four packed beds. Similar to the silica particles, a large temperature difference between T_{cru} and T is observed. On the average, $\Delta T = T_{\mathrm{cru}} - T$ = 86.5 K when $T_{\mathrm{cru}} = 673$ K and $\Delta T = 155$ K when $T_{\mathrm{cru}} = 873$ K. Overall the emittance of Carbobeads particles is quite high, noting that the minimum of ordinate is 0.70. The measurements were validated through repeating measurements over a period of time, though all particle samples are as received. No notable changes were observed through repeating measurements of the same batch of particles after several heating cycles.

For the bed packed with CP 30/60 particles, as shown in Figures 5.7 (a), there is a shift of the Christiansen wavelength towards longer wavelength from 8.0 μm at room temperature to 8.5 μm at elevated temperatures. Due to multiple phonon features associated with the constituent materials, there is a broadband emittance peak from 8–10 μm, which enables the determination of T and F_{C}. There is another peak near 9.5 μm. Even at T = 587 K, the spectrum at $\lambda < 3$ μm is very noisy and exceeds 1 towards shorter wavelengths. The short wavelength cutoff wavelength for the high-temperature emittance spectrum is set to $\lambda = 2$ μm. A valley in the region $2\ \mu\mathrm{m} < \lambda < 6\ \mu\mathrm{m}$ is present with a minimum about 4 μm at all temperatures for both CP 30/60 and CP 50/140. The large dip in the emittance for CP 50/140 has been discussed in the previous work [95], presumably due to the longer penetration depth and enhanced scattering by small particles. The measured emittance around λ = 4 μm for CP 50/140 increases by about 0.1 from room temperature to high temperatures. This was presumably a result of the temperature nonuniformity within the particle bed and the relatively large penetration depth with small particles. Additional emission from lower particle layers at higher temperatures may produce a relatively large emission signal. The exact reason requires further investigation. Similar to those with the

silica particles at wavelengths longer than 9.5 μm, the emittance at elevated temperatures is always higher than that at room temperature. The difference is less than 0.03 for 9.5 μm $< \lambda <$ 13 μm and about 0.05 beyond 13 μm. It may be caused by the temperature-dependent phonon structures or measurement uncertainties. It is unlikely that free carriers have any impact on the high-temperature emittance since Carbobead particles are made of refractory materials with very large band gaps.

For HSP particle beds, as shown in Figure 5.8, the long-wavelength trend is similar to that of CP particle beds, with a broadband peak that is slightly shifted towards longer wavelengths at elevated temperatures. The peak emittance occurs about $\lambda = 10$ μm at high temperatures. At $\lambda > 9.5$ μm, the emittance is similar at the two elevated temperatures and higher than that at room temperature by similar magnitude as for CP and silica particle beds. What is surprising is that there appears to be a reduction of emittance for $3\ \mu m < \lambda < 6\ \mu m$ for both HSP 30/60 and HSP 16/30 at high temperatures, resulting in a shift of the emittance minimum from near 2.5 μm to near 4 μm. The feature of this valley becomes similar to those with CP 30/60 particles. The mechanisms for causing such a strong temperature dependence in HSP particle beds are not yet clear and worth further investigation. Possible reasons are the change of chemical composition, porosity, as well as sintering and thermal stress effect. There are limited work reporting the effect of thermal stress and degradation of radiative properties due to thermal cycling. Siegal et al. [14] observed that thermal cycling Carbobead HSP particles over 500 hours at 1000 °C causes reduction in the absorptance for $\lambda < 2.5$ μm, especially towards 2.5 μm. Bush et al characterized the Fe_2O_3/Fe_3O_4 redox reactions in a two-step thermochemical cycle [138].

In the present study, the particle temperatures are much lower and the heating duration is much shorter, although the emittance was measured directly at elevated temperatures.

5.2.4 Total Emittance of Bauxite Particle Beds

The total normal emittance at a given temperature is calculated by weighting over the Planck distribution such that [106]

$$\varepsilon(T) = \frac{I(T)}{I_{\mathrm{b}}(T)} = \frac{\pi}{\sigma T^4} \int_0^\infty \varepsilon(\lambda, T) I_{\mathrm{b},\lambda}\left(\lambda, T\right) d\lambda \tag{5.4}$$

where I is total intensity of the sample, $I_{\mathrm{b}} = \sigma T^4 / \pi$ is the blackbody intensity in a vacuum, and σ is the Stefan-Boltzmann constant. For the Carbobead particle bed, the hemispherical emittance is expected to be close the normal emittance due to the topographic arrangement and surface roughness. The measured spectral range covers approximately 2.5 μm < λ < 16 μm with the high-temperature emissometer and 0.4 μm < λ < 15 μm at 300 K. In order to facilitate reasonable calculations of the total emittance, the room-temperature spectral emittance for λ < 1.8 μm is used to extend the high-temperature emittance toward shorter wavelengths and a constant value is assumed for λ > 16 μm (same as the emittance at λ = 16 μm). The transition region is linearly interpolated between λ = 1.8 μm (from T = 300 K) and λ = 3.0 μm (from high-temperature results) to further reduce the effect of low signal-to-noise ratio towards λ = 2.0 μm in the high-temperature data.

The calculated total emittance at each temperature is tabulated in Table 5.2 for packed beds with the four types of Carbobead particles. The total emittance is not evaluated for the silica particle bed due to semitransparency. For the same crucible temperature, the

particle bed may have different effective sample temperatures as indicated in parentheses. The sample temperature T is used when integrating the total emittance using Eq. (5.4).

Table 5.2. Total emittance of the bauxite particle beds. The sample temperature is in parentheses.

	CP		HSP	
	30/60	50/140	30/60	16/30
Ambient (300 K)	0.927	0.917	0.911	0.890
T_{cru} = 673 K	0.955 (587 K)	0.933 (582 K)	0.942 (591 K)	0.958 (586 K)
T_{cru} = 873 K	0.939 (716 K)	0.912 (711 K)	0.927 (726 K)	0.944 (719 K)

As T_{cru} increases from 300 K to 673 K and 873 K, $\varepsilon(T)$ is shown to increase and then decrease slightly. The increase is due to the higher spectral emittance at high temperatures compared to that of the room temperature, especially at longer wavelength. The decrease of the total emittance when T_{cru} increases from 673 K to 873 K is due to the shift of the Planck's blackbody emission peak towards short wavelength, coupled to a reduced spectral emittance towards 4 μm. The change, however, is not as significant. Except for HSP 16/30 whose emittance increases from 0.890 at 300 K to 0.958 at 586 K, and then reduces to 0.944 at 719 K. The emittance of other packed beds increases by 0.03 (for T_{cru} from 300 K to 673 K) and decreases by less than 0.02 (for T_{cru} from 673 K to 873 K). Overall, the total emittance varies from 0.89 to 0.96.

The maximum achievable sample temperature (T = 726 K) for the bauxite particle bed is limited by experiment setup in this work due to the limitations of the heater and the ambient pressure condition. Nevertheless, this work offers the first quantitative direct measurements of the spectral emittance of bauxite particle beds. The quantitative results may help refine the heat transfer modeling of the particle-to-particle and particle-to-wall radiation transfer processes.

CHAPTER 6

MODELING THE SPECTRAL RADIATIVE PROPERTIES OF PACKED BED WITH MIXED BAUXITE AND SILICA PARTICLES

This chapter provides a theoretical investigation on the radiative properties of particle beds with mixed bauxite and silica particles. A Monte Carlo ray-tracing algorithm is developed to simulate for the spectral reflectance, transmittance, and absorptance. By applying IAD method on the simulated radiative properties, the effective absorption and reduced scattering coefficients of the particle beds are determined. The effects of particle mixing ratio, and the particle volume fraction are quantified. By applying independent scattering assumption on individual particles, the effective absorption and reduced scattering coefficients are also modeled and compared with IAD to access the impact of particle mixture on scattering assumptions.

6.1 Modeling Condition and Assumptions

6.1.1 Spatial Relations

The Monte Carlo algorithm introduced in Sec. 2.4 allows for ray-tracing simulation performed on a variety of combinations of modeling parameters. While repeating-unit representation of the particle bed extends to infinity in x and y directions, the thickness in the z direction is characterized by the number of particle layers, K. The inter-layer distance is half of the unit cell side length, ξ, which is related to particle volume fraction, ϕ_v, and the particle diameter, d. The spatial relationship is described by Eq. (2.14). The thickness of the particle bed can be described as

$$L = \frac{\xi}{2}(K-1) + d \tag{6.1}$$

The relative thickness, commonly referred to as the specific thickness, L^*, can be calculated from $L^* = L/d$. A spatial correlation between aforementioned physical parameters can be illustrated in Figure 6.1.

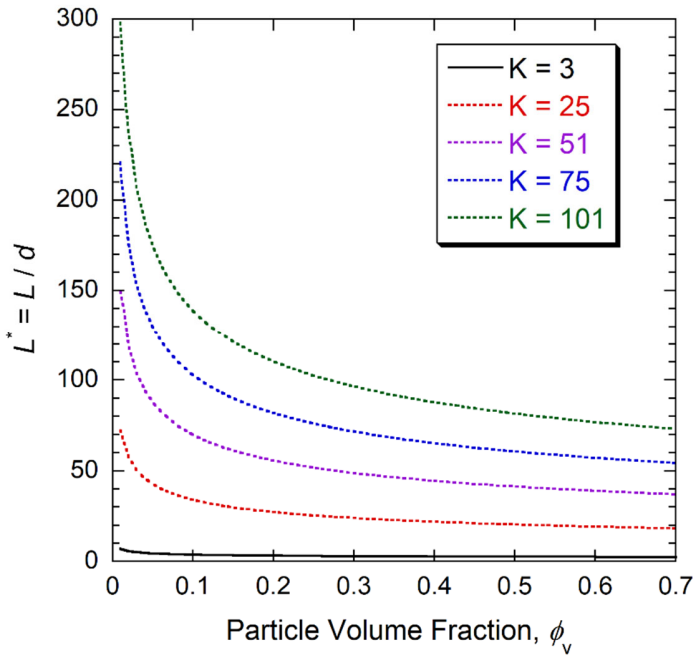

Figure 6.1. Spatial correlation between the particle volume fraction, specific thickness, and the number of layers of particles in a particle bed prescribed by FCC.

L^* is expected to change in a nonlinear relationship with ϕ_v, due to the 3rd order relationship between d and ϕ_v shown in Eq. (2.14). For ϕ_v that decreases to below 0.05, L^* has the tendency to approach infinity as ξ becomes increasingly large. Large L^* are likely to result in opaque particle bed regardless of the radiative properties of particles. For a particle receiver utilizing Bauxite particles, the curtain thickness is tens of millimeters, while the particle diameter is usually 0.1-1 mm to produce optically thick media [22], leading to $L^* \approx 100$. There are also particle receivers that utilizes silica, which is

semitransparent and require a higher L^* to produce the same opacity. The effective a_λ and σ_λ can be obtained by applying IAD analysis to the reflectance and transmittance of the particle beds. While it accounts for the effect of dependent scattering, an optically thick particle bed does not have sufficient light transmission. Hence, a thinner particle bed is preferred. Further, since L^* is a function of both the function of ϕ_v and d, it is simpler to represent the thickness with K. For this reason, the number of layers in the simulation is set to $K = 15$, assuming that a_λ and σ_λ are independent of particle bed thickness (validated). The particle diameter is set to $d = 200$ μm, and the simulation uses 10^5 photon bundles per combination of ϕ_v and r, where $r = m / n$ is the mixing ratio described in Eqs. (2.6) and (2.7). The particles are assumed to be spherical and the surface is smooth with specular reflection ($S = 1$).

6.1.2 Refractive Index of Bauxite and Silica

The complex refractive index, $\tilde{n} = n + \mathrm{i}\kappa$, for bauxite is previously modeled with effective medium theory in Chapter 3 (Sec. 3.5) considering contribution from individual constituents (metal oxides) and pores. The results are plotted together with the refractive index of silica, shown in Figure 6.2.

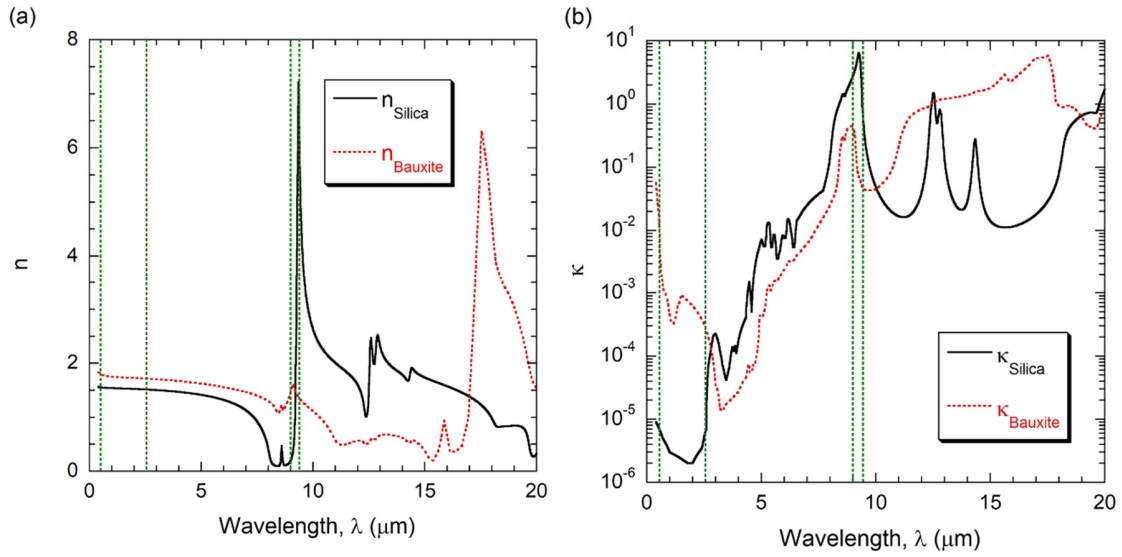

Figure 6.2. Complex refractive index of particles with green dotted line indicating λ = 0.50, 2.60, 9.00, and 9.35 μm, respectively. (a) n (b) κ.

Due to each of the materials have spectrally dependent refractive index, four representative wavelengths are selected for the investigation on the radiative properties of particle mixture, the corresponding values for n and κ are shown in Table 6.1.

Table 6.1. Complex refractive index for bauxite and silica.

	λ	0.50	2.60	9.00	6.35
Bauxite	n	1.82	1.71	1.46	1.37
	κ	2.17E-02	2.56E-04	4.28E-01	5.43E-02
Silica	n	1.55	1.51	0.19	7.21
	κ	7.67E-06	7.00E-06	2.75E-00	3.05E-00

At $\lambda = 0.50$ μm, bauxite particles are opaque due to high absorption index, while silica is semitransparent with little absorption. At $\lambda = 2.60$ μm, both particles become semitransparent. The absorption coefficient for bauxite is $a = 4\pi\kappa / \lambda = 0.0012$ μm^{-1}, or a

penetration depth of 808.21 μm. At $\lambda = 9.00$ μm , $n < 1$ for silica while κ is large, similar to the situation of a metal surface that can cause high surface reflection. At $\lambda = 9.35$ μm , there is a very high peak for n resulted from the optical phonon band structure.

6.2 Modeling Results

For each of the selected wavelength, the radiative properties are first simulated from the Monte Carlo ray tracing simulation. Then, the results are inputted to the IAD model assuming isotropic scattering and zero effective refractive index. The results from IAD are effective absorption and reduced scattering coefficients that includes dependent scattering effect (volume scattering). As it was shown in Ch. 4, the asymmetry factor is close to 0 for particles in the particle beds when modeled with Monte Carlo method. The reduced scattering coefficient is close to the true scattering coefficient. Full lists of simulation results and IAD results can be found in Appendix A1.

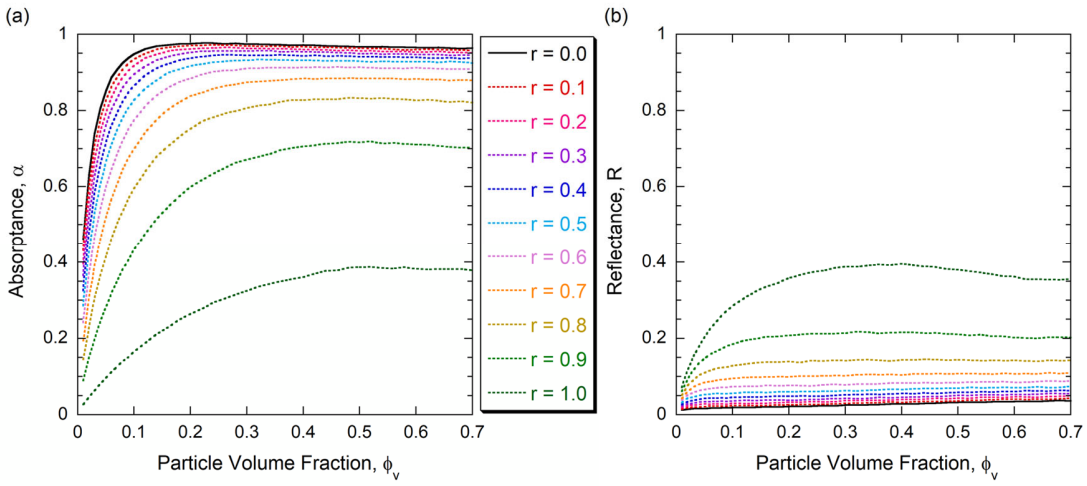

Figure 6.3. Monte Carlo ray tracing simulation of radiative properties of particle bed mixture at $\lambda = 0.50$ μm . (a) absorptance (b) reflectance.

Figure 6.3 shows the simulated absorptance and reflectance for the particle bed mixture at $\lambda = 0.50$ μm. The change in radiative properties is nonlinear with the change in mixing ratio. At $r = 1.0$ and $\phi_v = 0.7$ (dense silica particle bed), the absorptance and reflectance are $\alpha = 0.38$ and $R = 0.35$, reflectively. When 10% of silica particles are replaced with bauxite particles, $r = 0.9$, there is a significant increase in absorptance, $\alpha = 0.70$ ($\Delta\alpha = +0.32$), and decrease in reflectance, $R = 0.20$ ($\Delta R = -0.15$). For $r = 0.8$, $\alpha = 0.82$ ($\Delta\alpha = +0.12$) and $R = 0.15$ ($\Delta R = -0.05$) comparing to $r = 0.9$. As the change in r is kept constant ($|\Delta r| = 0.1$), the change in radiative properties decreases. This trend is also seen in Figure 6.4 (a) for absorption coefficients. However, σ_λ are relatively less dependent on the mixing effect and has an overall magnitude less than the absorption coefficients. Similar properties can also be found in Figure A1.3 (e) in the Appendix, for $\lambda = 2.60$ μm. There exists a crossover of σ_λ for $\lambda > 0.50$ μm, as shown in Figure 6.4 (b), which is attributed to the dependent scattering effect at higher volume fractions and will be discussed further in Sec. 6.3.

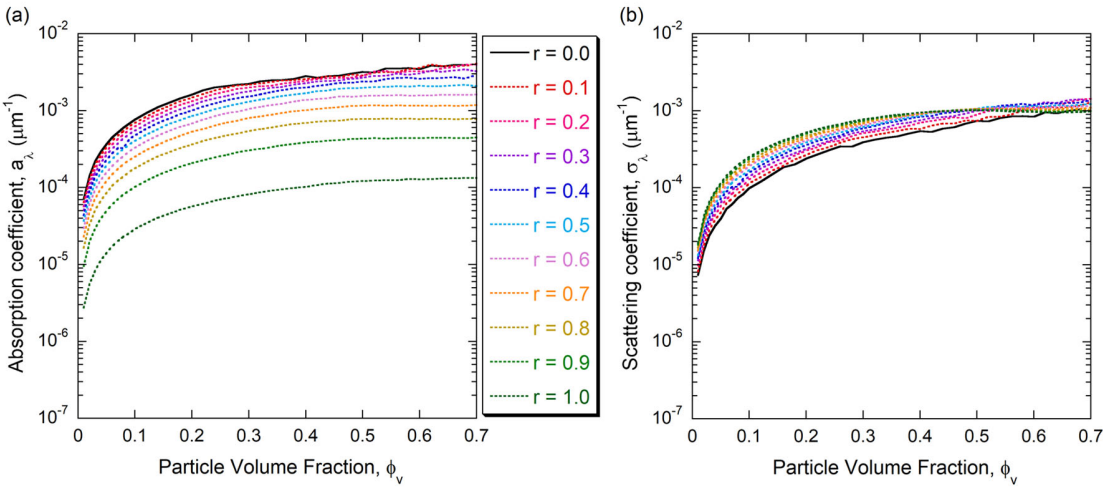

Figure 6.4. IAD results for particle bed mixture at $\lambda = 0.50$ μm. (a) absorption coefficients (b) reduced scattering coefficients.

For the case of $r = 1.0$, there is a reflectance peak associated with $\phi_v \approx 0.4$ as seen in Figure 6.3 (b). The scattering by particles consists of both reflection and refraction. Because interparticle distance reduces for densely packed particle beds, as ϕ_v increases, light transmission through a particle layer is mostly refraction. For dilute particle beds, there is both refraction and transmission without interception by particles. The combined effect results in little change of reflectance for in a wide range of ϕ_v ($0.1 < \phi_v < 0.7$).

When the particle bed has only bauxite particles ($r = 0.0$), the radiative properties show negligible change for $\phi_v > 0.1$, as there is no more transmitted light and the reflection only take place in top layers of the particle bed.

The volume fraction of a particle mixture with mixing ratio r can be expressed as

$$\phi_v = \frac{(m+l)V_{\mathrm{p}}}{V} \tag{6.2}$$

where V_{p} is the volume of a single particle, and $n = m + l$ is the total number of particles. *m* and *l* are the number of silica and bauxite particles, respectively. The volume fraction of bauxite particles in a mixture bed can be expressed as

$$\phi_{v,\mathrm{bauxite}} = \frac{lV_{\mathrm{p}}}{V} = \frac{n(1-r)V_{\mathrm{p}}}{V} = \phi_v(1-r) \tag{6.3}$$

For $r = 0.9$, and a dense particle bed at $\phi_v = 0.7$, $\alpha = 0.7$ and $R = 0.20$. The bauxite particle has a volume fraction of $\phi_{v,\mathrm{bauxite}} = \phi_v(1-r) = 0.07$. On the other hand, when there are only bauxite particles ($r = 0.0$) at $\phi_v = 0.07$, $\alpha = 0.9$ and $R = 0.02$. The comparison of the two cases shows that for the same particle volume fraction of bauxite particles, a dense mixture bed ($r = 0.9$, $\phi_v = 0.7$) produces lower absorptance and much higher reflectance than the dilute single-particle-type bed ($r = 0.0$, $\phi_v = 0.07$). This

feature is also observed in the absorption coefficients as shown in Figure 6.4 (a), as a_λ is lower in the mixture. Such phenomenon is due to the additional back scattering by silica particles so that the bed reflectance is increased.

At $\lambda = 2.60$ μm, both bauxite and silica particles are semitransparent with internal absorption. The penetration depths are 808 μm and 29,557 μm for bauxite and silica particles, respectively. The bauxite particles are more absorbing, resulting in an increase of the absorptance as r decreases, shown in Figure A1.1 (d) in the Appendix. Although the simulation is performed with $K = 15$, which results in particle bed thickness of 2~8 mm depending on ϕ_v, the transmittance decreases to nearly zero for $\phi_v > 0.4$ and $r = 0.0$. Hence, opacity in applications utilizing bauxite particle beds can easily be reached even at the spectral region where the particles are semitransparent, with few layers of particles and loosely packed condition. The overall trends in radiative properties and IAD results are similar to the case of $\lambda = 0.50$ μm. Because both particles are semitransparent, and the refractive index are similar, σ_λ are almost identical for all mixing ratios as shown in Figure A1.3 (e). The scattering albedo shown in Figure A1.3 (f) is mostly constant throughout ϕ_v.

At $\lambda = 9.00$ μm and $\lambda = 9.35$ μm, both bauxite and silica particles are opaque. The bauxite particles are highly absorbing due to low n. For silica particles at $\lambda = 9.00$ μm, $n < 1$ and $\kappa > 1$, making it highly reflective. At $\lambda = 9.35$ μm, silica has very high n and κ, resulting in lower surface reflectivity higher absorptivity than $\lambda = 9.00$ μm. The simulated absorptance and reflectance for $\lambda = 9.00$ μm is shown in Figure 6.5.

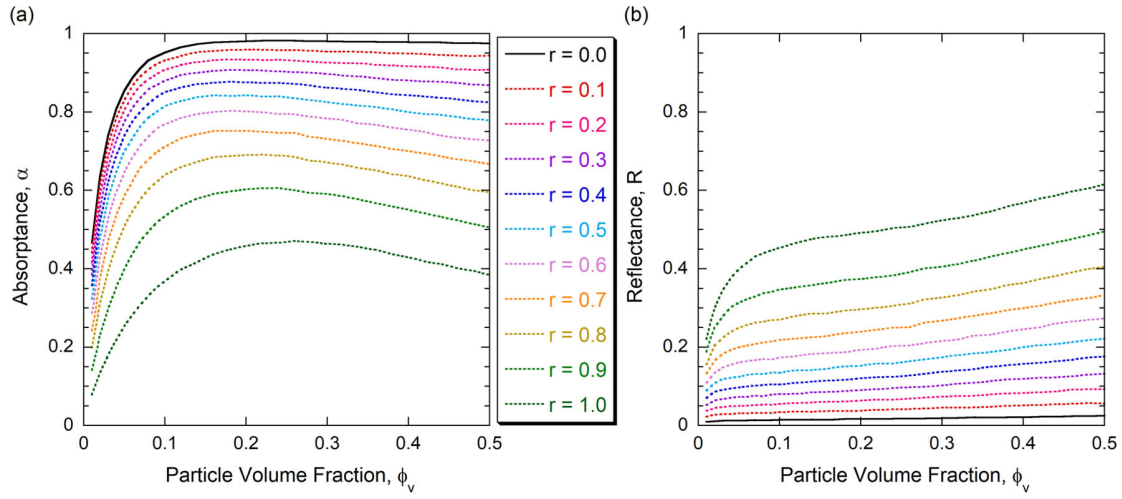

Figure 6.5. Monte Carlo ray tracing simulation of radiative properties of particle bed mixture at $\lambda = 9.00$ μm . (a) absorptance (b) reflectance.

Due to both particles are opaque, the $\alpha + R = 1$ for $\phi_v \approx 0.2$ (dependent of r), resulting in $T = 0$ for most of mixing conditions. Different from the cases of $\lambda = 0.50$ μm and $\lambda = 2.60$ μm , in the region $r = 0.1 - 1.0$, peak values for α are observed for different ϕ_v that increases with r. This property is directly related to the number of scattering events associated with each photon bundle before being terminated or exited from the bed. When ϕ_v is low, increasing ϕ_v dramatically increases the scattering (surface reflection) by particles as more bundles are intercepted instead of direct transmission through the bed. This results in α and R to increase sharply. Depending on the value of r, when the associated peak ϕ_v is reached, further increasing ϕ_v reduces α. The reason is that the bed becomes opaque beyond this point, and interparticle distances reduces, limiting light scattering to the top layers of the particle bed. As a result, α decreases. However, less scattering by particles indicate less attenuation upon each reflection, hence R monotonically increases with ϕ_v.

The IAD results for absorption and reduced scattering coefficients for $\lambda = 9.00$ μm are shown in Figure 6.6.

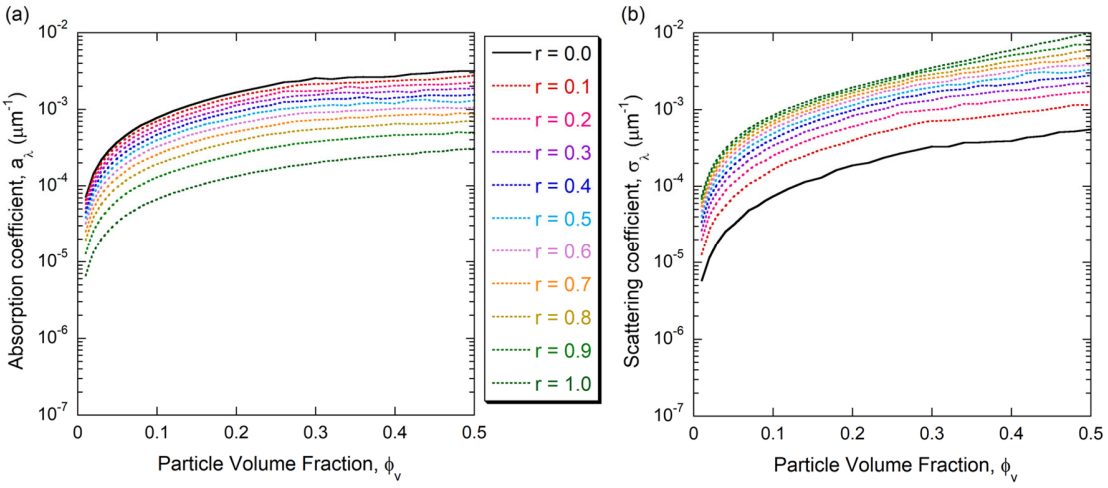

Figure 6.6. IAD results for particle bed mixture at $\lambda = 9.00$ μm . (a) absorption coefficients (b) reduced scattering coefficients.

The trends observed in the absorption coefficients are similar to the case of $\lambda = 0.50$ μm , with α change nonlinearly with r. It is interesting to note that for σ_λ shown in Figure 6.6 (b), the greatest change results from $r = 0.0$ to $r = 0.1$, which is opposite to the trend observed for the absorption coefficients and the case for $\lambda = 0.50$ μm shown in Figure 6.4 (a). This could be due to their specific phase functions (to be discussed in Table 6.2) in addition to their difference in the complex refractive index. For bauxite particles, there is significant forward scattering all investigated wavelengths. Silica particles scatter isotopically for $\lambda = 9.00$ μm and $\lambda = 9.35$ μm . Further discussion is combined with modeling from independent scattering theory elucidated in Sec. 6.3. The dependent scattering affects the scattering albedo, which is observed to increase with ϕ_v, detailed in Figure A1.4 (e).

6.3 Effect of Dependent Scattering

The absorption and reduced scattering coefficients are also modeled from independent scattering theory. The single-particle absorption and scattering cross sections and the scattering phase function are determined from Monte Carlo ray tracing simulations of a single particle. Using Eqs. (2.6) and (2.7), the effective absorption and reduced scattering coefficients considering only independent scattering are modeled. The radiative properties are modeled with the AD method. Results are compared with those obtained from Monte Carlo simulation and the IAD method to illustrate the effect of dependent scattering.

The only unknown variables from Eqs. (2.6) and (2.7) are $C_{1,\mathrm{abs},\lambda}$, $C_{2,\mathrm{abs},\lambda}$, $C_{1,\mathrm{sca},\lambda}$, and $C_{2,\mathrm{sca},\lambda}$, which can be generally expressed, respectively, as

$$C_{\mathrm{abs},\lambda} = Q_{\mathrm{abs},\lambda} C \tag{6.4}$$

$$C_{\mathrm{sca},\lambda} = Q_{\mathrm{sca},\lambda} C \tag{6.5}$$

where $Q_{\mathrm{abs},\lambda}$ and $Q_{\mathrm{sca},\lambda}$ are the absorption and scattering efficiency factors, and C is the cross-sectional area of the particles. In order to obtain the radiative properties of particle beds using AD method, the asymmetry factor, g, is obtained from fitting the simulated scattering phase function of the particle with HG function. Note that a_λ and σ_λ obtained from IAD calculation assumed isotropic scattering ($g = 0$), in which case the reduced scattering coefficient is the same as the true scattering coefficient: $\sigma_\lambda = \sigma_{\lambda,\,\mathrm{true}}\left(1-g\right)$. To model from independent scattering theory, it is important to recognize that g is different for bauxite and silica particles. Since rqs2.7) is applicable for both the σ_λ and $\sigma_{\lambda,\mathrm{true}}$,

$C_{\text{sca},\lambda}$ can be multiplied by $(1-g)$ to ensure the reduced scattering coefficient σ_λ is inputted to the AD calculation. It has also been tested that for AD calculation, the results obtained from inputting a_λ and σ_λ to the model are very close to the case of only a_λ, $\sigma_{\lambda,\text{true}}$, and g. To be consistent with Ch. 4, the scattering albedo, ω, is calculated from $\sigma_\lambda / (a_\lambda + \sigma_\lambda)$. All key parameters pertinent to the independent scattering calculation are tabulated in Table 6.2.

Table 6.2. Parameters used for independent scattering calculation of absorption and reduced scattering coefficients and radiative properties.

	λ	0.50	2.60	9.00	9.35
Bauxite	$Q_{\text{abs},\lambda}$	0.86	0.20	0.88	0.93
	$Q_{\text{sca},\lambda}$	0.14	0.80	0.12	0.07
	g	0.46	0.50	0.50	0.61
Silica	$Q_{\text{abs},\lambda}$	0.03	0.01	0.09	0.40
	$Q_{\text{sca},\lambda}$	0.97	0.99	0.91	0.60
	g	0.57	0.59	0	-0.02

For $\lambda = 0.50$ μm and $\lambda = 2.60$ μm, both bauxite and silica particles are forward scattering due to specular reflecting assumption and the semitransparent particle. For $\lambda = 9.00$ μm, the bauxite particle has the same g as $\lambda = 2.60$ μm, however, the magnitude for $Q_{\text{abs},\lambda}$ and $Q_{\text{sca},\lambda}$ are almost switched. For silica particles, $n < 1$ with high κ cause isotropic scattering, with a very high $Q_{\text{sca},\lambda}$. At $\lambda = 9.35$ μm, silica particles are

slightly backward scattering but mostly isotropic, while bauxite particles are forward scattering. The results for $Q_{\text{abs},\lambda}$, $Q_{\text{sca},\lambda}$, and g are inputted to Eqs. (6.4) and (6.5), and then Eqs. (2.6) and (2.7) to model for a_λ and σ_λ considering independent scattering. The results are then applied with AD method to obtain the corresponding radiative properties. Full lists of modeling results for radiative properties, absorption and reduced scattering coefficients, and the scattering albedo can be found in Appendix A2.

Modeled absorptance and reflectance for is shown in Figure 6.7 and compared with the simulation results by Monte Carlo.

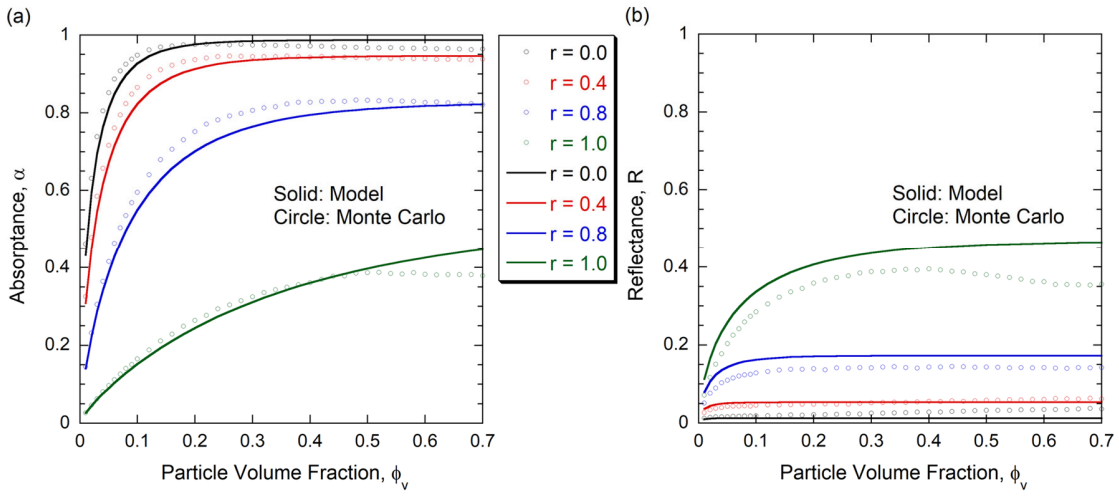

Figure 6.7. Comparison between independent scattering model and Monte Carlo simulation for particle bed mixture at $\lambda = 0.50$ μm . (a) absorptance (b) reflectance.

At $\lambda = 0.50$ μm , the prediction by the independent scattering theory model qualitatively captures the trend observed in Figure 6.3. The similar nonlinear relationship between the change of radiative properties and the change of r is captured, as well as the overall trend as ϕ_v increases. The independent predicted results tend to have asymptotic behavior. Large deviations are observed for densely packed silica beds ($r = 1.0$) when the

model overpredicts reflectance, as shown in Figure 6.7 (b). When $r = 0.0$, the model tends to underpredict reflectance. However, the deviation is small due to low reflectance. The comparison in the absorption and reduced scattering coefficients are shown in Figure 6.8.

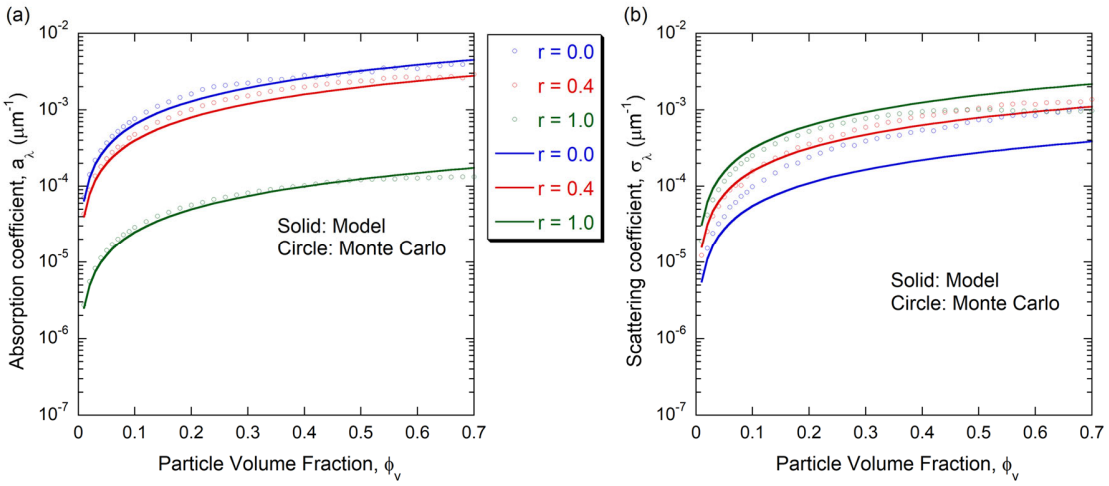

Figure 6.8. Comparison between independent scattering model and Monte Carlo simulation for particle bed mixture at $\lambda = 0.50$ μm. (a) absorption coefficient (b) reduced scattering coefficient.

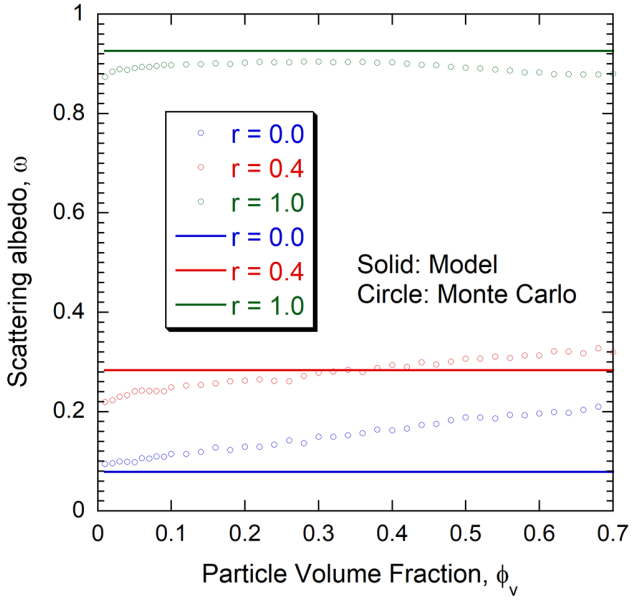

Figure 6.9. Comparison of scattering albedo between independent scattering model prediction and Monte Carlo simulation for particle bed mixture at $\lambda = 0.50$ μm.

The Monte Carlo simulation and model prediction match well in a_λ. However, there are significant deviations in σ_λ that is related to both r and ϕ_v. The model underpredicts σ_λ for $r = 0.0$ and overpredicts for $r = 1.0$. The deviation also becomes larger at higher ϕ_v. For $0.0 < r < 1.0$, competing effect of r and ϕ_v result in the crossover observed in Figure 6.4 (b). Larger deviation associated with low r is consistent with the observation in [51], as opaque particles tend to induce more dependent scattering. The scattering albedo is shown in Figure 6.9. The comparison confirms the previous observation that the ϕ_v independence is only observed for beds of semitransparent particles. For a particle bed of bauxite particles ($r = 1.0$), ω increase with ϕ_v. The mixing of the two types of particles produces the transition between the two extreme examples and shows that independent scattering model prediction is still qualitatively valid when $r = 0.4$.

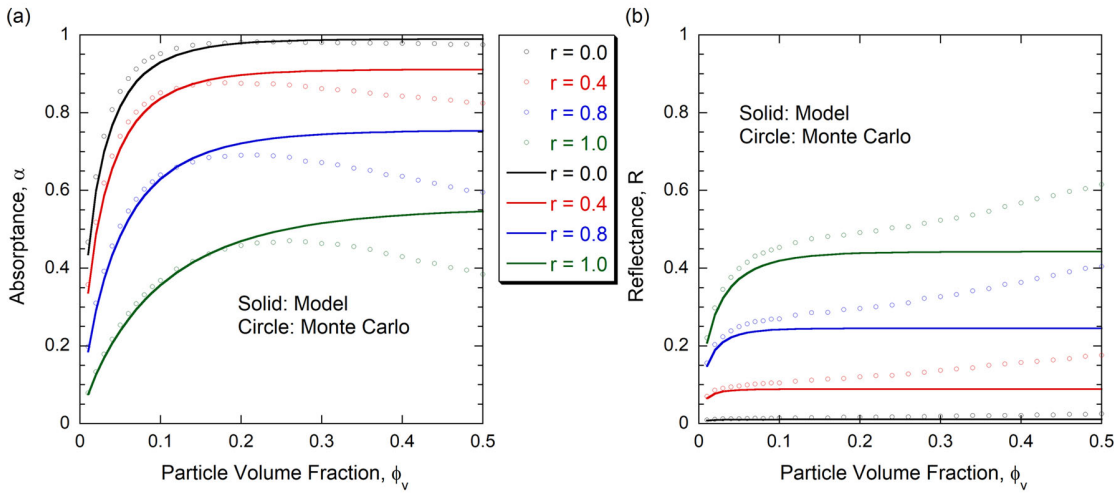

Figure 6.10. Comparison between independent scattering model and Monte Carlo simulation for particle bed mixture at $\lambda = 9.00$ μm. (a) absorptance (b) reflectance.

For $\lambda = 2.60$ μm, the model prediction accuracy is similar to the case of $\lambda = 0.50$ μm. However, due to both particles are semitransparent, the reduced scattering

coefficients match almost perfectly, as shown in the Figure A1.3 (e) and Figure A2.3 (e), respectively. The fitted values for g (using HG function), and a_λ and σ_λ are similar for the two particles, resulting in overlapped results predicted by the independent scattering model. Due to these reasons, the comparisons are not shown here and are placed in the Appendix.

Figure 6.10 shows the comparison of the radiative properties predicted by the model and from the Monte Carlo simulation for $\lambda = 9.00$ μm. When dependent scattering is expected for beds of opaque particles, the model prediction qualitatively matches the simulation for low ϕ_v (<0.1). While the simulation results indicate local peak α that is dependent of r, the model prediction suggests asymptotic increase of both α and R with ϕ_v, similar to the situation of Figure 6.7 (a). Deviations are observed and increase with ϕ_v for $\phi_v > 0.1$ and with increasing r. Note that $Q_{\text{sca},\lambda} = 0.91$, $g = 0$ for silica particles, and $Q_{\text{abs},\lambda} = 0.88$, $g = 0.50$ for bauxite particles. Replacing bauxite particles with silica particles significantly increases σ_λ when r is low, as shown in Figure 6.11 (b). The deviation between the model and simulation is relatively consistent for different r. The absorption coefficients, on the other hand, are perfectly modeled by the independent scattering theory despite the differences in $Q_{\text{abs},\lambda}$, $Q_{\text{sca},\lambda}$, and g. Finally, the dependent scattering effect is also demonstrated in ω, shown in Figure 6.12. The dependence on ϕ_v is only present in the simulation results. It is interesting to note that for $r = 0.0$ and $r = 1.0$, the corresponding deviations are smaller than for $r = 0.4$. While the reason is unclear, the mixing effect could potentially enhance dependent scattering for opaque particles.

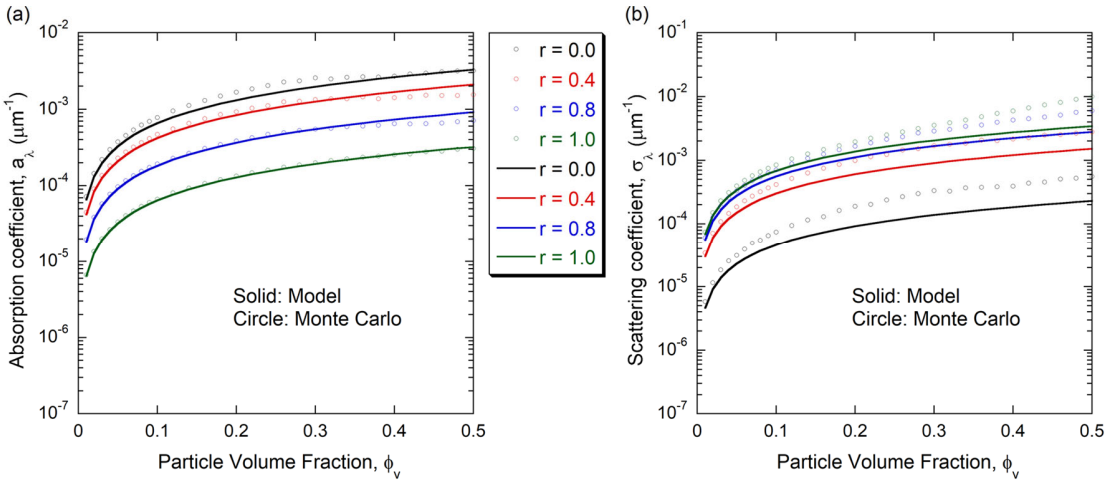

Figure 6.11. Comparison between independent scattering model and Monte Carlo simulation for particle bed mixture at $\lambda = 9.00$ μm . (a) absorption coefficient (b) reduced scattering coefficient.

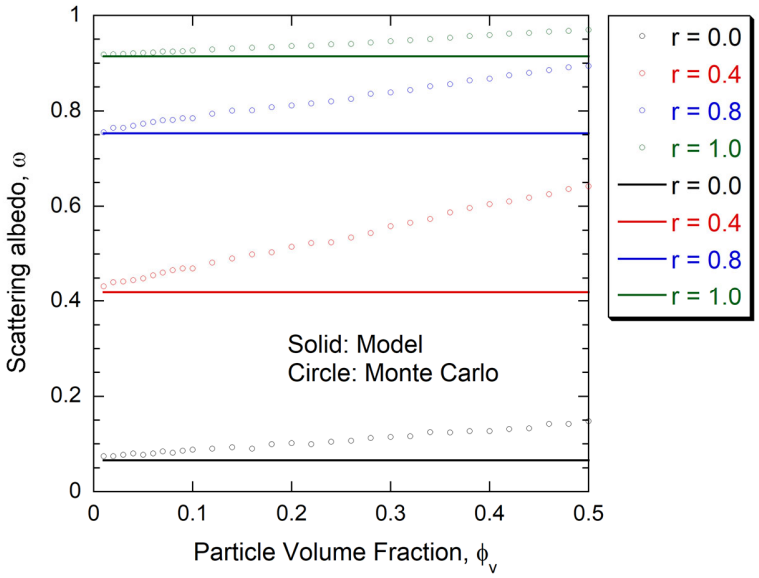

Figure 6.12. Comparison of scattering albedo between independent scattering model prediction and Monte Carlo simulation for particle bed mixture at $\lambda = 9.00$ μm .

CHAPTER 7

CONCLUSIONS AND FUTURE WORK

7.1 Conclusions

This dissertation investigates the thermal radiative properties and radiation heat transfer of bauxite and SiO_2 particles for solar thermal applications via both experimental and theoretical characterization.

7.1.1 Radiative Properties of Bauxite Particle Beds

Spectral radiative properties of bauxite particle beds are investigated in Chapter 3. A measurement technique using windowed sample holder is developed and the directional-hemispherical reflectance of packed particle beds is obtained for six different bauxite ceramic particles over wavelengths from 0.38 μm to 15 μm. By analyzing the optical properties of individual oxides, it can be inferred that Fe_2O_3 is responsible for the high solar absorptance (0.94–0.96) of all particle beds. High MIR absorptance at wavelengths from 8–10 μm is attributed to multiple phonon resonances from constituents especially Al_2O_3 and SiO_2. The total emittance of the HSP particle is high (0.94-0.95 at 1000 K), while a size effect is observed on the emittance for the CP particles (changing from 0.92 to 0.84 as the median diameter is reduced from 450 μm to 200 μm). Surface roughness and cavity effects may also enhance the absorptance of particle beds. Using effective medium approaches, the optical constants of the particles are obtained and used to explain the absorption dip and size dependence in CP particles between λ = 2 μm and 5 μm. The calculated absorptance of particle surfaces (assuming that the particle is a homogeneous

effective medium with a smooth surface) outlines the general trend of the measured absorptance for particle beds.

7.1.2 Radiative Properties of Silica Particle Beds

Spectral radiative properties of polydisperse silica particle beds are investigated in Chapter 4. The directional–hemispherical reflectance and transmittance of packed beds of polydispersed and irregular-shaped SiO_2 particles with different average diameters and bed thicknesses are measured and analyzed using both continuous-scale and discrete-scale modeling. The effective absorption and reduced scattering coefficients obtained for different sized particles from IAD in the visible and near-infrared may be applied for solution of RTE under similar conditions. The absorption by impurities of SiO_2 in the particle beds becomes significant at wavelengths from 0.4 μm to 1.8 μm, even though it is often negligible in bulk materials. The scattering albedo is shown over 98% for all particles in the wavelength region between 1.0 μm and 1.8 μm. A discrete-scale Monte Carlo method is developed to model the radiative properties by assuming monodispersed spherical particles using a specularity parameter. The model generally agrees with the measurement at wavelengths from 0.4 μm to 1.8 μm, except when the transmittance is very low. The trend in the reflectance up to 15 μm is also predicted. Cavity effects increase the absorption in the phonon resonance band from 8 μm to 10 μm, especially with smaller sized particles. Using independent scattering theory, the absorption and reduced scattering coefficients are obtained and compared with IAD to demonstrate dependent scattering effect in Type B and C particles. It is shown that for Type A particles with an average diameter of 222 μm that is relatively round with small size variation, the independent

scattering theory is appropriate for modeling the hemispherical radiative properties of particle beds. Since the packed bed is already dense, this conclusion should also be applicable when the bed is not densely packed.

7.1.3 Temperature-Dependent Emittance of Particle Beds

Temperature-dependent emittance of bauxite and silica particle beds are investigated in Chapter 5. The characterization of temperature-dependent radiative properties of particles helps further fulfill the knowledge gap to accurately model radiation heat transfer in particle beds for TES applications. The spectral normal emittance of bauxite and silica particle beds of different sizes were measured for 2 μm < λ < 16 μm at effective bed temperatures up to ~730 K. A noncontact temperature determination technique was used to calculate effective sample temperature and the associated blackbody reference signal. Validations of the setup was performed using a homogenous fused silica disc. The increase of the emittance in the infrared region (8 μm < λ < 10 μm) at higher temperatures was attributed to increases in the damping coefficients. Similar temperature dependent features were also observed for silica particle beds. For bauxite particle beds, over wavelengths of 3 μm < λ < 7 μm, the emittance increases at elevated temperatures for CP particle beds, whereas the emittance decreases for HSP particle beds. Both CP and HSP particle beds have an increase emittance at longer wavelengths of λ > 9.5 μm. The total emittance for CP and HSP particle beds at different temperatures was calculated with an average over 0.90.

7.1.4 Radiative Properties of Mixing Bauxite and Silica Particles

Particle mixtures of bauxite and silica particles are investigated to determine radiative properties as a function of particle bed configurations such as the particle volume fraction, and the mixing ratio. The radiative properties of various mixture beds at four representative wavelengths are numerically studied from the Monte Carlo ray-tracing simulation. The results demonstrate the addition of bauxite particles into the silica particle bed significantly increases the absorptance while decreasing the transmittance. The change of radiative properties shows a nonlinear relationship to the change of mixing ratio. Localized absorptance maxima are observed for beds of opaque particle mixture as a function of particle volume fraction and mixing ratio, while reflectance maximum is observed for mixture containing semitransparent particles. The simulation results inputted to the IAD method to obtain the effective absorption and reduced scattering coefficients, and the scattering albedo that are useful in a continuous-scale radiation transfer modeling. These coefficients are also modeled from the independent scattering theory for particle mixture to demonstrate the effect of dependent scattering. For mixture of semitransparent particles, the independent theory is largely valid for particle volume fraction smaller than 0.50. For mixtures of opaque particles, the deviations are the largest as also observed by earlier works and increase towards higher particle volume fractions [51]. The absorption coefficients are predicted by the independent scattering theory with better accuracy, while the reduced scattering coefficients are underpredicted. Another feature of dependent scattering that the scattering albedo shows a dependence on the volume fraction, which is not observed in the independent scattering model. This dependence is also a function of mixing ratio. Mixing the semitransparent and opaque particles (bauxite and silica particles

at $\lambda = 0.50\ \mu m$) has less dependent scattering effect than mixing opaque particles with different radiative properties.

7.2 Future Work

Further investigations are needed to enable more robust characterization of the absorption and scattering mechanisms in particulate media through advancements in the experimental, theoretical, and numerical methods. Complex physical phenomenon needs to be considered to obtain more accurate model predictions. Recommendations for specific tasks appropriate for making the improvements are elucidated below:

- Investigations of the internal scattering mechanisms of bauxite particles. The effective dielectric function obtained in Chapter 3 can be used for calculating the absorption coefficient but cannot be used to predict the effective scattering coefficients. Large semitransparent plate samples sharing the same chemical content, weight fractions, and pore sizes need to be fabricated and measured for directional-hemispherical reflectance and transmittance. Using the inverse adding-doubling method, the effective absorption and scattering coefficients can be obtained.
- Characterization of the thermal cycling effect on the radiative properties of bauxite particles. In practical applications, the particles are often under continuous thermal stress due to heating and the cooling effects that may result in thermal expansion, surface wear, and even chemical (or the associated weight fraction) change. All may result in the change of the radiative properties due the internal scattering within the particles that are sensitive to the size of grain and air pores. Room-temperature

radiative properties can be measured using the windowed sampling technique developed in Chapter 3 for several patches of particles each placed under a different thermal cycling period.

- Improvements on the instrumentation and measurement techniques for the temperature-dependent emittance so that push the effective emission temperature over 800 °C. This will facilitate better understanding of the temperature-dependent phonon structure for different metal oxides and better align with the current operation temperatures of particle receivers. Ring-shaped thermal insulation over the top surface of the particle bed could be used to minimize convective, conductive, and radiative heat loss. The ring-shape design is necessary to allow the thermal emission signal been collected by the optical layout. An evacuated sample chamber can be used to reduce convective heat loss. However, numerical model that accounts for temperature gradient across the bed needs to be developed that facilitates thermal contact resistance and light scattering by particles.
- Investigation of the radiative properties of more complex configurations of particulate media. The discrete-scale Monte Carlo ray-tracing algorithm can be improved to include poly-dispersion effect by inputting measured particle size distribution models or by developing the equivalent algorithm. Consequently, wave effect associated with smaller-sized particles needs to be accounted by individually altering the single-particle absorption or scattering coefficients or the scattering phase function. The algorithm for the mixing effect can be further improved for mixtures of multiple types of particles by modifying the probabilistic particle-type determination scheme in the code.

- Integration of the dependent-scattering-included absorption and scattering coefficients in conjugate heat transfer models. The effective absorption and scattering coefficients of particulate media with different particle volume fractions can be experimentally determined and compared with the ray tracing model. This can inform model validity and calibrate the model by fine tuning for appropriate secularity and particle size distribution (for the improved algorithm in the previous recommendation). Interpolation can be made using the model prediction on the absorption and scattering coefficients with several representative particle volume fractions, particle sizes, mixing ratios, and bed thicknesses. The results are then inputted to a conjugated heat transfer model considering radiative heat transfer processes.

APPENDIX

A1: Monte Carlo Ray Tracing Simulation Results and IAD Results for Mixing Particles

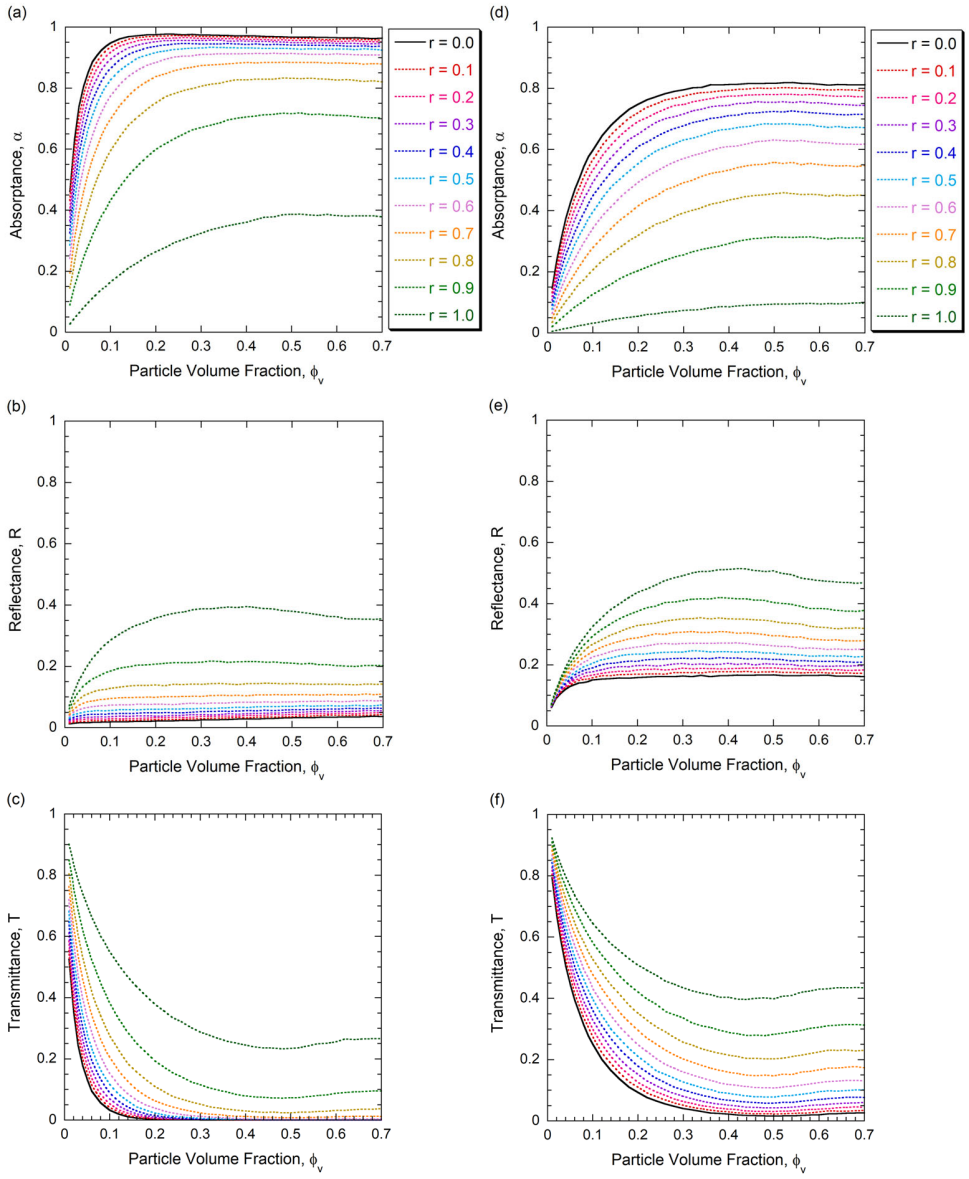

Figure A1.1. Radiative properties of particle bed with mixing bauxite and silica particles at λ = 0.50 μm: (a) absorptance (b) reflectance (c) transmittance. At λ = 2.60 μm: (d) absorptance (e) reflectance (f) transmittance.

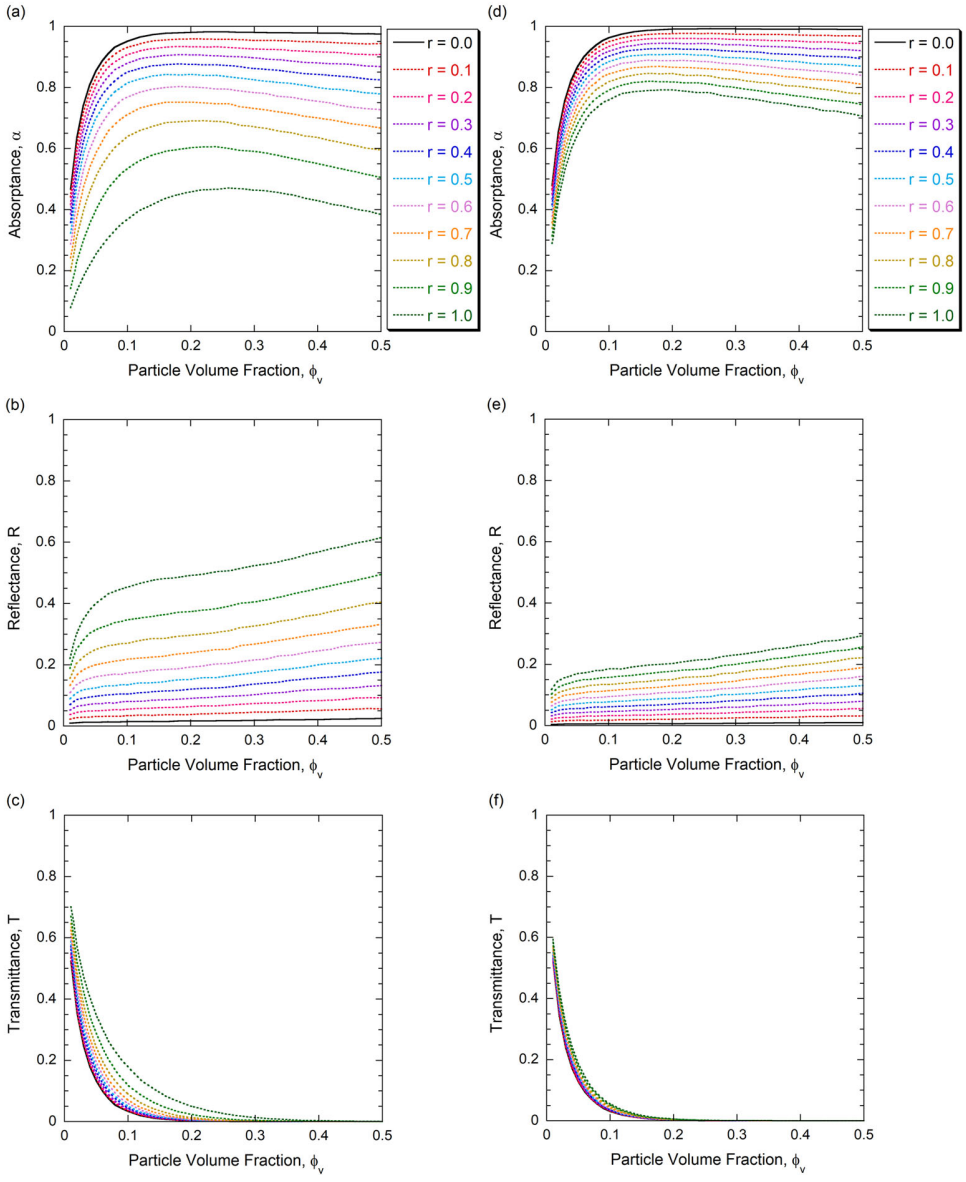

Figure A1.2. Radiative properties of particle bed with mixing bauxite and silica particles at λ = 9.00 μm: (a) absorptance (b) reflectance (c) transmittance. At λ = 9.35 μm: (d) absorptance (e) reflectance (f) transmittance.

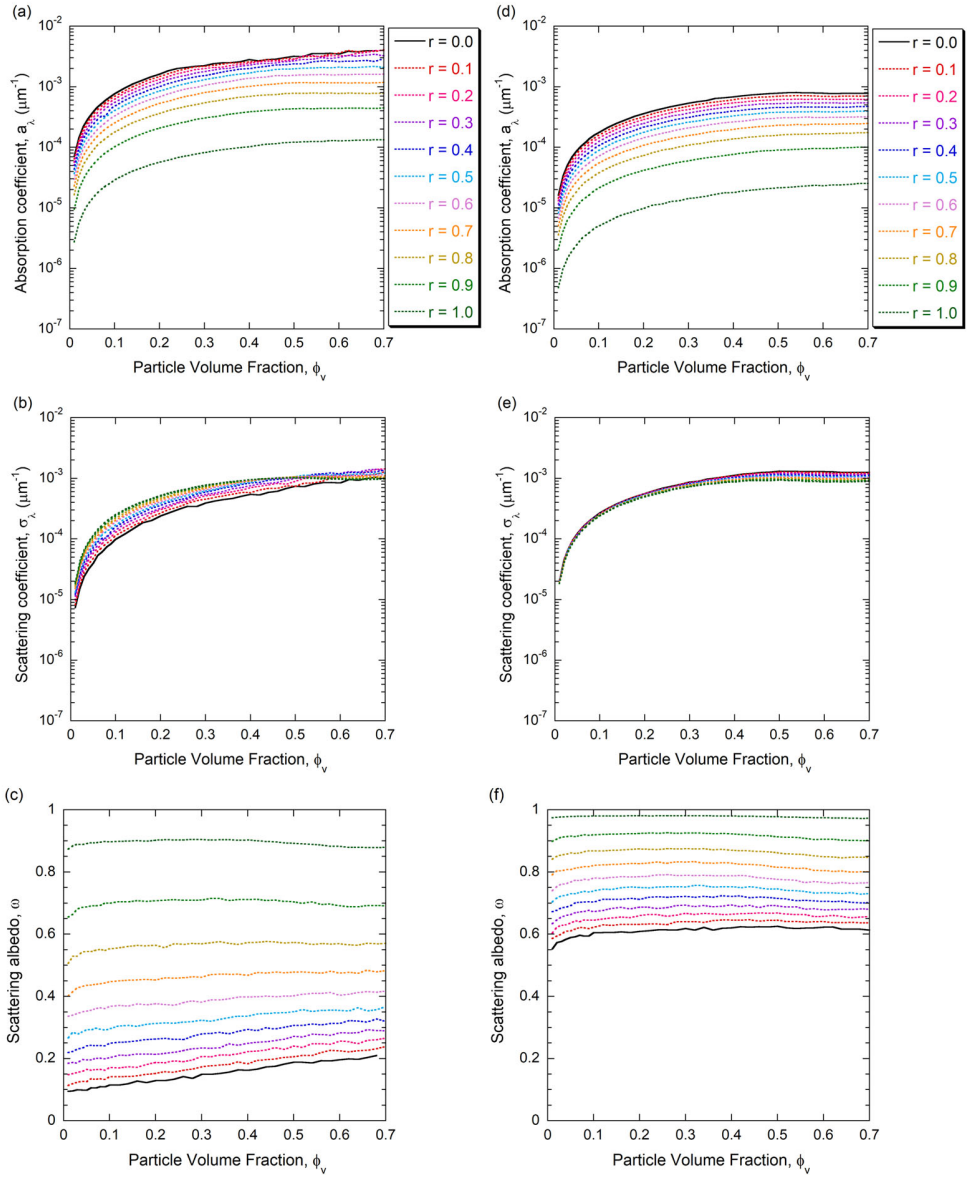

Figure A1.3. IAD retrieved absorption and scattering properties of particle bed with mixing bauxite and silica particles at λ = 0.50 μm: (a) absorption coefficient (b) reduced scattering coefficient (c) scattering albedo. At λ = 2.60 μm: (d) absorption coefficient (e) reduced scattering coefficient (f) scattering albedo.

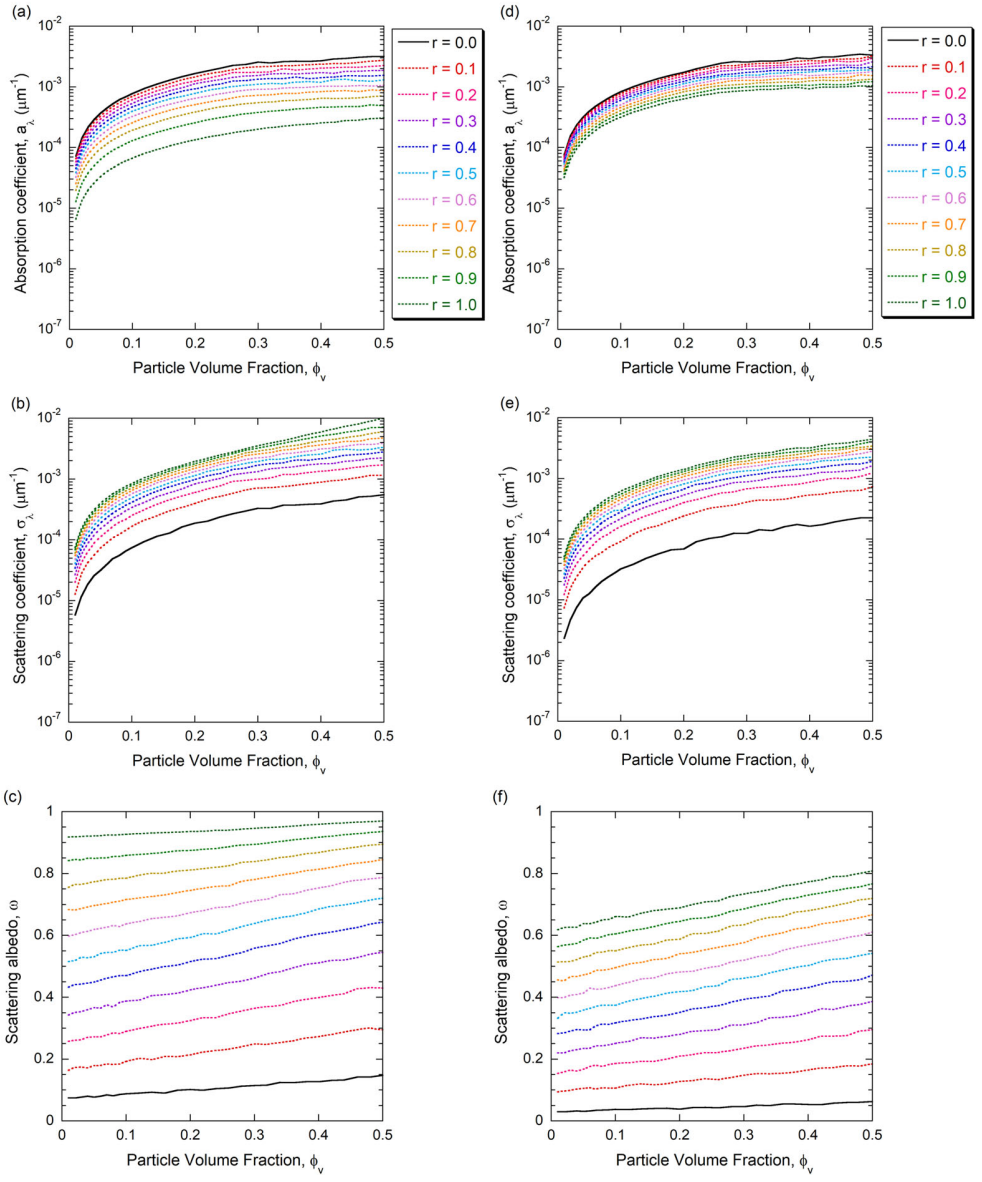

Figure A1.4. IAD retrieved absorption and scattering properties of particle bed with mixing bauxite and silica particles at λ = 9.00 μm: (a) absorption coefficient (b) reduced scattering coefficient (c) scattering albedo. At λ = 9.35 μm: (d) absorption coefficient (e) reduced scattering coefficient (f) scattering albedo.

A2: Independent Scattering Prediction of Radiative Properties, Absorption Coefficients, Reduced Scattering Coefficients, and Scattering Albedo of Mixing Particles

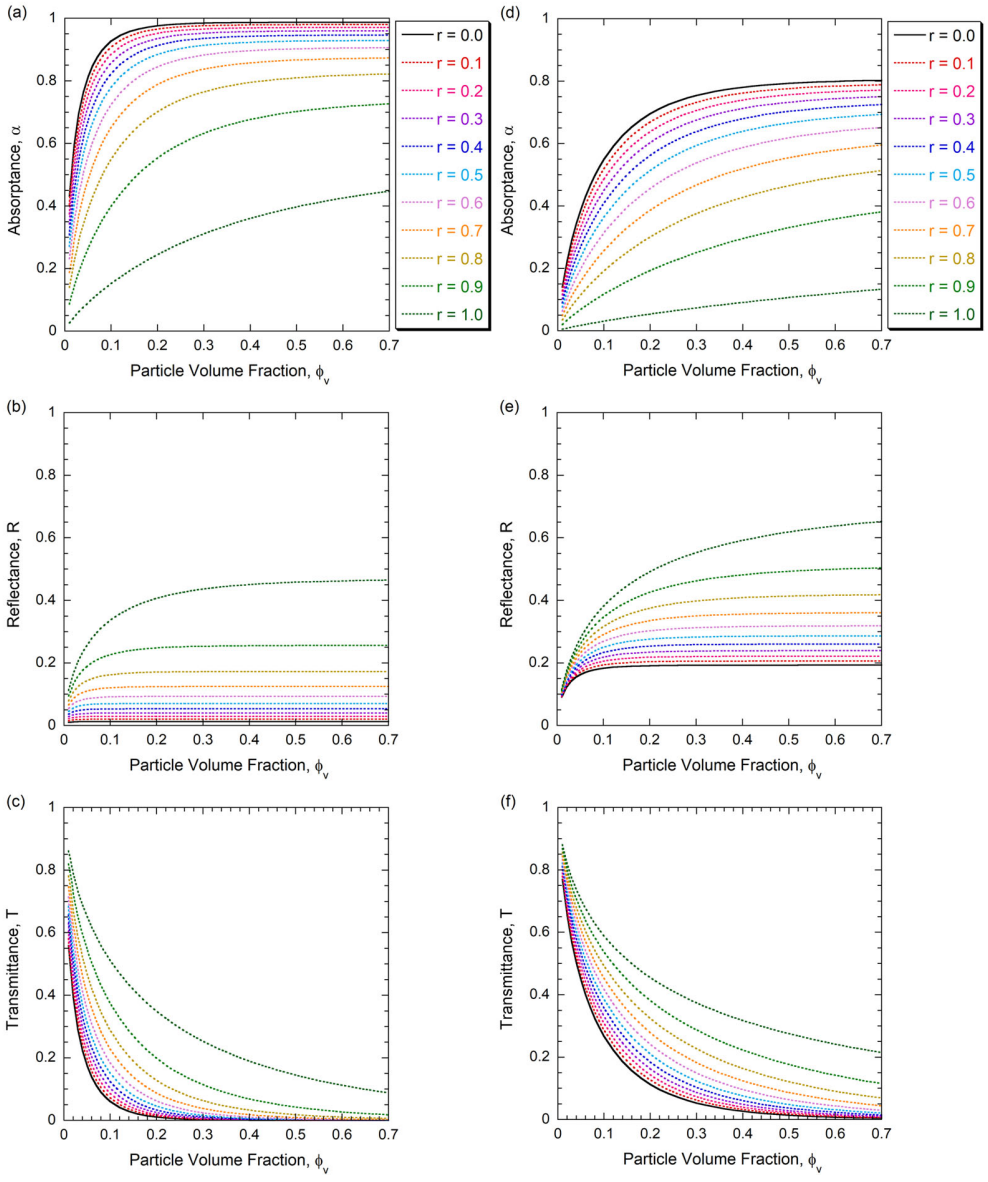

Figure A2.1. Independent scattering prediction of radiative properties of particle bed with mixing bauxite and silica particles at λ = 0.50 μm: (a) absorptance (b) reflectance (c) transmittance. At λ = 2.60 μm: (d) absorptance (e) reflectance (f) transmittance.

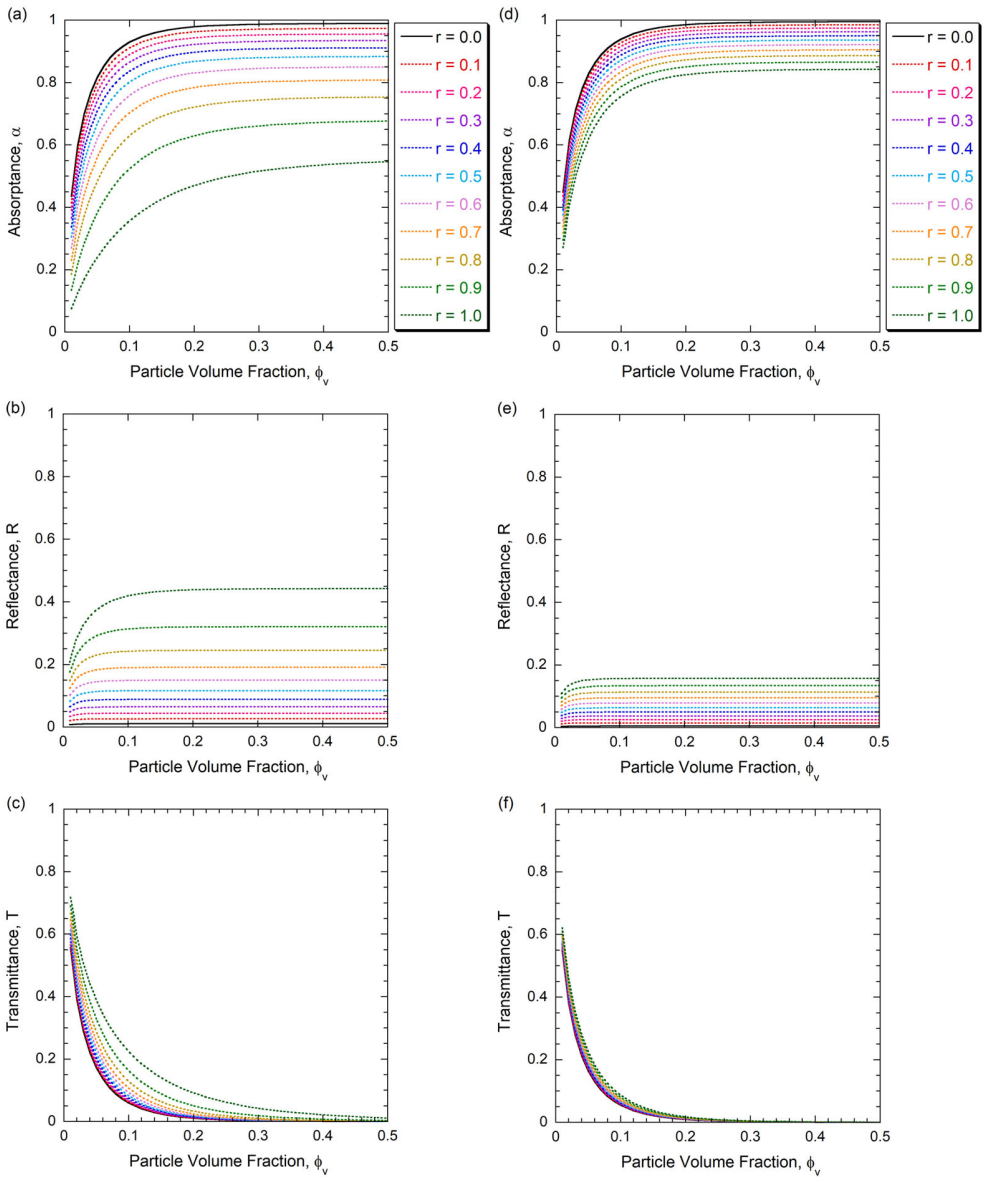

Figure A2.2. Independent scattering prediction of radiative properties of particle bed with mixing bauxite and silica particles at λ = 9.00 μm: (a) absorptance (b) reflectance (c) transmittance. At λ = 9.35 μm: (d) absorptance (e) reflectance (f) transmittance.

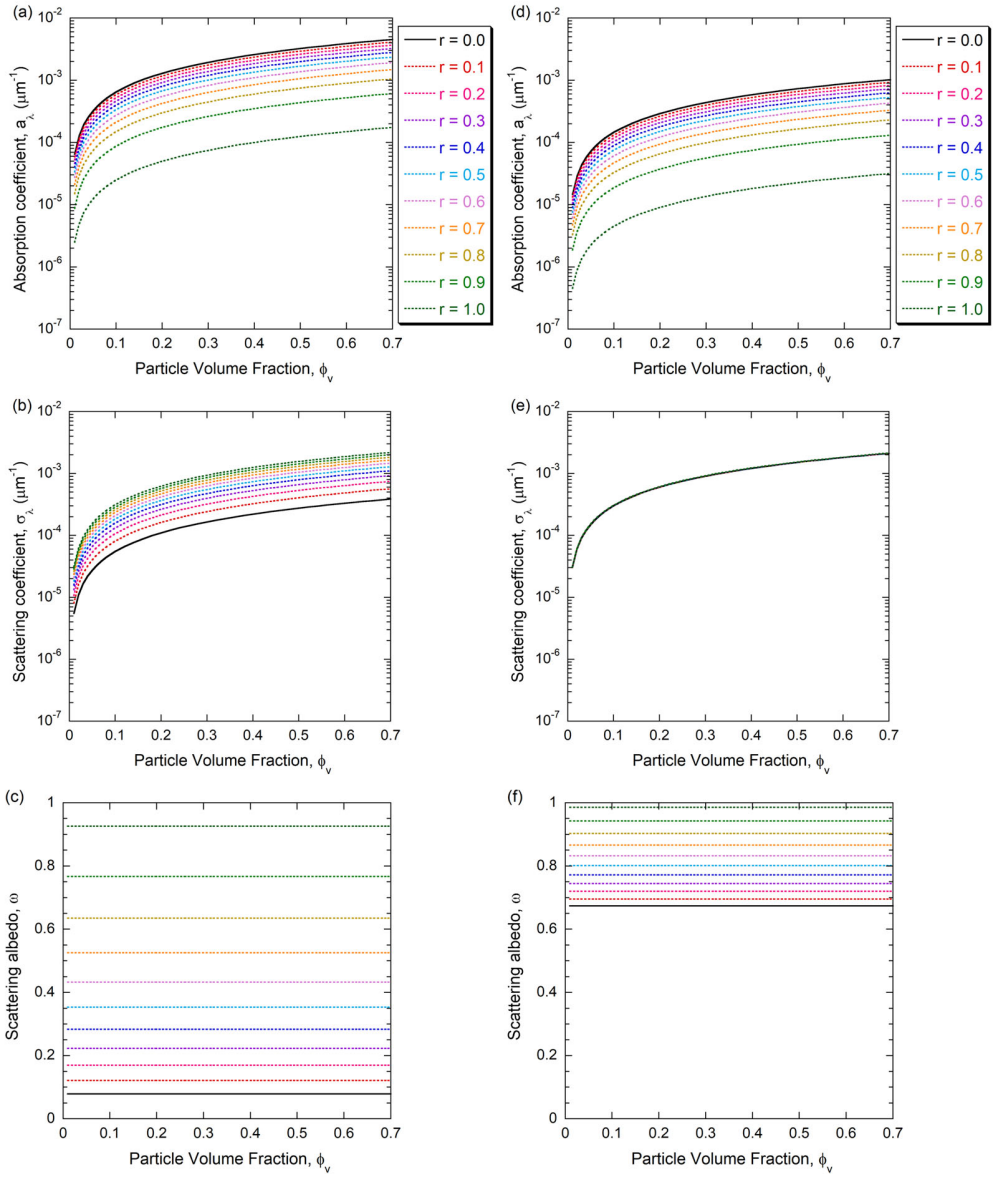

Figure A2.3. Independent scattering prediction of absorption and scattering properties of particle bed with mixing bauxite and silica particles at λ = 0.50 μm: (a) absorption coefficient (b) reduced scattering coefficient (c) scattering albedo. At λ = 2.60 μm: (d) absorption coefficient (e) reduced scattering coefficient (f) scattering albedo.

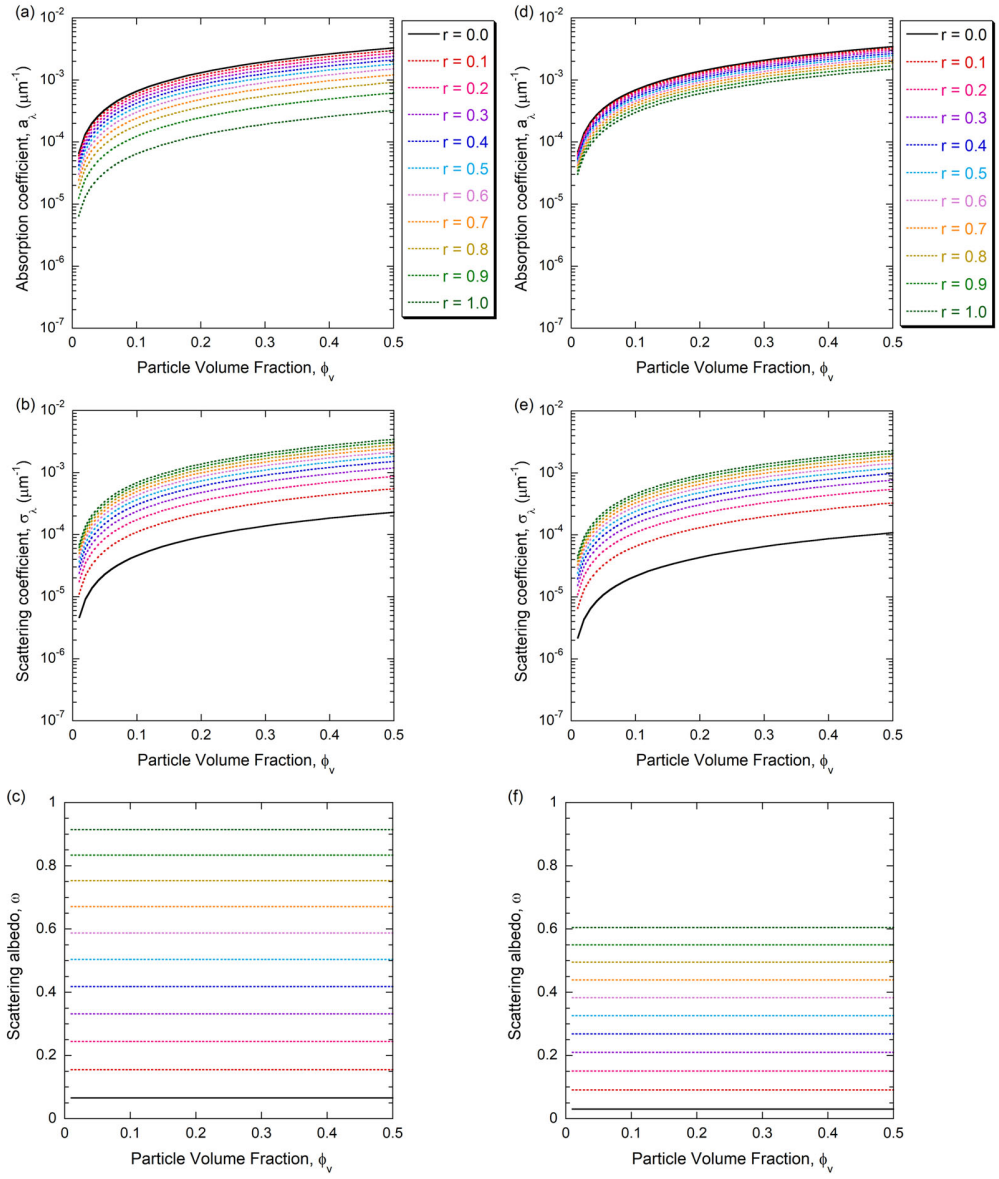

Figure A2.4. Independent scattering prediction of absorption and scattering properties of particle bed with mixing bauxite and silica particles at λ = 9.00 μm: (a) absorption coefficient (b) reduced scattering coefficient (c) scattering albedo. At λ = 9.35 μm: (d) absorption coefficient (e) reduced scattering coefficient (f) scattering albedo.

REFERENCES

[1] J. Rockström, O. Gaffney, J. Rogelj, M. Meinshausen, N. Nakicenovic, H. J. Schellnhuber, A Roadmap for Rapid Decarbonization, Science, Vol. 355, No. 6331, 2017, pp. 1269-1271.

[2] B. Parida, S. Iniyan, R. Goic, A Review of Solar Photovoltaic Technologies, Renewable and sustainable energy reviews, Vol. 15, No. 3, 2011, pp. 1625-1636.

[3] A. Gil, M. Medrano, I. Martorell, A. Lázaro, P. Dolado, B. Zalba, L. F. Cabeza, State of the Art on High Temperature Thermal Energy Storage for Power Generation. Part 1—Concepts, Materials and Modellization, Renewable and Sustainable Energy Reviews, Vol. 14, No. 1, 2010, pp. 31-55.

[4] S. Kuravi, J. Trahan, D. Y. Goswami, M. M. Rahman, E. K. Stefanakos, Thermal Energy Storage Technologies and Systems for Concentrating Solar Power Plants, Progress in Energy and Combustion Science, Vol. 39, No. 4, 2013, pp. 285-319.

[5] M. Liu, N. S. Tay, S. Bell, M. Belusko, R. Jacob, G. Will, W. Saman, F. Bruno, Review on Concentrating Solar Power Plants and New Developments in High Temperature Thermal Energy Storage Technologies, Renewable and Sustainable Energy Reviews, Vol. 53, 2016, pp. 1411-1432.

[6] M. T. Islam, N. Huda, A. Abdullah, R. Saidur, A Comprehensive Review of State-of-the-Art Concentrating Solar Power (CSP) Technologies: Current Status and Research Trends, Renewable and Sustainable Energy Reviews, Vol. 91, 2018, pp. 987-1018.

[7] A. G. Fernández, J. Gomez-Vidal, E. Oró, A. Kruizenga, A. Solé, L. F. Cabeza, Mainstreaming Commercial CSP Systems: A Technology Review, Renewable Energy, Vol. 140, 2019, pp. 152-176.

[8] D. Barlev, R. Vidu, P. Stroeve, Innovation in Concentrated Solar Power, Solar Energy Materials and Solar Cells, Vol. 95, No. 10, 2011, pp. 2703-2725.

[9] W. Lipiński, J. H. Davidson, S. Haussener, J. F. Klausner, A. M. Mehdizadeh, J. Petrasch, A. Steinfeld, L. Venstrom, Review of Heat Transfer Research for Solar Thermochemical Applications, Journal of Thermal Science and Engineering Applications, Vol. 5, No. 2, 2013, paper 021005.

[10] T. Baumann, S. Zunft, Properties of Granular Materials as Heat Transfer and Storage Medium in CSP Application, Solar Energy Materials and Solar Cells, Vol. 143, 2015, pp. 38-47.

[11] C. K. Ho, A Review of High-Temperature Particle Receivers for Concentrating Solar Power, Applied Thermal Engineering, Vol. 109, Part B, 2016, pp. 958-969.

[12] C. K. Ho, Advances in Central Receivers for Concentrating Solar Applications, Solar Energy, Vol. 152, 2017, pp. 38-56.

[13] A. J. Schrader, H. E. Bush, D. Ranjan, P. G. Loutzenhiser, Aluminum-Doped Calcium Manganite Particles for Solar Thermochemical Energy Storage: Reactor Design, Particle Characterization, and Heat and Mass Transfer Modeling, International Journal of Heat and Mass Transfer, Vol. 152, 2020, Paper 119461.

[14] N. P. Siegel, M. D. Gross, R. Coury, The Development of Direct Absorption and Storage Media for Falling Particle Solar Central Receivers, Journal of Solar Energy Engineering, Vol. 137, No. 4, 2015, Paper 041003.

[15] C. K. Ho, J. M. Christian, J. E Yellowhair, K. Armijo, W. J. Kolb, S. Jeter, M. Golob, C. Nguyen, On-Sun Performance Evaluation of Alternative High-Temperature Falling Particle Receiver Designs, Journal of Solar Energy Engineering, Vol. 141, No. 1, 2019, Paper 011009.

[16] H. Al-Ansary, A. El-Leathy, S. Jeter, M. Golob, C. Nguyen, E. Djajadiwinata, S. Alaqel, R. Saeed, S. Abdel-Khalik, Z. Al-Suhaibani, Design Features of the World's First Commercial Concentrating Solar Power Plant Using the Particle Heating Receiver Concept, Proc. ASME 2019 13th Int. Conf. Ener. Sust., 2019, Paper ES2019-3856.

[17] H. Hottel, A. Sarofim, W. Dalzell, I. Vasalos, Optical Properties of Coatings. Effect of Pigment Concentration, AIAA Journal, Vol. 9, No. 10, 1971, pp. 1895-1898.

[18] C. Tien, Thermal Radiation in Packed and Fluidized Beds, Journal of Heat Transfer, Vol. 110, No. 4b, 1988, pp. 1230-1242.

[19] D. Baillis, J.-F. Sacadura, Thermal Radiation Properties of Dispersed Media: Theoretical Prediction and Experimental Characterization, Journal of Quantitative Spectroscopy and Radiative Transfer, Vol. 67, No. 5, 2000, pp. 327-363.

[20] B. Wang, C. Zhao, Modeling Radiative Properties of Air Plasma Sprayed Thermal Barrier Coatings in the Dependent Scattering Regime, International Journal of Heat and Mass Transfer, Vol. 89, 2015, pp. 920-928.

[21] T. Fu, J. Tang, K. Chen, F. Zhang, Determination of Scattering and Absorption Coefficients of Porous Silica Aerogel Composites, Journal of Heat Transfer, Vol. 138, No. 3, 2016, Paper 032702.

[22] C. K. Ho, J. M. Christian, D. Romano, J. Yellowhair, N. Siegel, L. Savoldi, R. Zanino, Characterization of Particle Flow in a Free-Falling Solar Particle Receiver, Journal of Solar Energy Engineering, Vol. 139, No. 2, 2017, Paper 021011.

[23] J. Chen, V. M. Wheeler, B. Liu, A. Kumar, J. Coventry, W. Lipiński, Optical Characterisation of Alumina–Mullite Materials for Solar Particle Receiver Applications, Solar Energy Materials and Solar Cells, Vol. 230, 2021, Paper 111170.

[24] K. M. Chung, J. Zeng, S. R. Adapa, T. Feng, M. V. Bagepalli, P. G. Loutzenhiser, K. J. Albrecht, C. K. Ho, R. Chen, Measurement and Analysis of Thermal Conductivity of Ceramic Particle Beds for Solar Thermal Energy Storage, Solar Energy Materials and Solar Cells, Vol. 230, 2021, Paper 111271.

[25] N. P. Siegel, M. D. Gross, C. K. Ho, T. Phan, J. Yuan, Physical Properties of Solid Particle Thermal Energy Storage Media for Concentrating Solar Power Applications, Energy Procedia, Vol. 49, 2014, pp. 1015-1023.

[26] G. Evans, W. Houf, R. Greif, C. Crowe, Gas-Particle Flow within a High Temperature Solar Cavity Receiver Including Radiation Heat Transfer, Journal of Solar Energy Engineering, Vol. 109, No. 2, 1987, pp. 134-142.

[27] A. Kumar, J.-S. Kim, W. Lipiński, Radiation Absorption in a Particle Curtain Exposed to Direct High-Flux Solar Irradiation, Journal of Solar Energy Engineering, Vol. 140, No. 6, 2018, Paper 061007.

[28] J. R. Howell, M. P. Menguc, R. Siegel, Thermal Radiation Heat Transfer, 7th ed., CRC Press, New York, 2021.

[29] J. Roop, S. Jeter, S. I. Abdel-Khalik, C. K. Ho, Optical Properties of Select Particulates after High-Temperature Exposure, ASME 8th Inernaltional Conference on Energy Sustainability, Oct. 2014,

[30] C. Chen, Y. Chiyu, D. Ranjan, G. P. Loutzenhiser, Z. M. Zhang, Spectral Radiative Properties of Polydispersed Sio_2 Particle Beds, Journal of Thermophysics and Heat Transfer, (In press),

[31] J. Martinek, Z. Ma, Granular Flow and Heat-Transfer Study in a near-Blackbody Enclosed Particle Receiver, Journal of Solar Energy Engineering, Vol. 137, No. 5, 2015, Paper 051008.

[32] E. F. Johnson, İ. Tarı, D. Baker, Modeling Heat Exchangers with an Open Source Dem-Based Code for Granular Flows, Solar Energy, Vol. 228, 2021, pp. 374-386.

[33] W. Wang, Y. Shuai, B. G. Lougou, B. Jiang, Thermal Performance Analysis of Free-Falling Solar Particle Receiver and Heat Transfer Modelling of Multiple Particles, Applied Thermal Engineering, Vol. 187, 2021, Paper 116567.

[34] O. Rozenbaum, D. D. S. Meneses, Y. Auger, S. Chermanne, P. Echegut, A Spectroscopic Method to Measure the Spectral Emissivity of Semi-Transparent Materials up to High Temperature, Review of Scientific Instruments, Vol. 70, No. 10, 1999, pp. 4020-4025.

[35] L. d. Campo, R. B. Pérez-Sáez, X. Esquisabel, I. Fernández, M. J. Tello, New Experimental Device for Infrared Spectral Directional Emissivity Measurements in a Controlled Environment, Review of Scientific Instruments, Vol. 77, No. 11, 2006, Paper 113111.

[36] C. P. Cagran, L. M. Hanssen, M. Noorma, A. V. Gura, S. N. Mekhontsev, Temperature-Resolved Infrared Spectral Emissivity of SiC and Pt–10Rh for Temperatures up to 900° C, International Journal of Thermophysics, Vol. 28, No. 2, 2007, pp. 581-597.

[37] L. Wang, S. Basu, Z. Zhang, Direct Measurement of Thermal Emission from a Fabry–Perot Cavity Resonator, Journal of Heat Transfer, Vol. 134, No. 7, 2012, Paper 072701.

[38] I. Setién-Fernández, T. Echániz, L. González-Fernández, R. Pérez-Sáez, E. Céspedes, J. Sánchez-García, L. Álvarez-Fraga, R. E. Galindo, J. Albella, C. Prieto, First Spectral Emissivity Study of a Solar Selective Coating in the 150–600° C Temperature Range, Solar Energy Materials and Solar Cells, Vol. 117, 2013, pp. 390-395.

[39] S. Shan, C. Chen, P. G. Loutzenhiser, D. Ranjan, Z. Zhou, Z. M. Zhang, Spectral Emittance Measurements of Micro/Nanostructures in Energy Conversion: A Review, Frontiers in Energy, Vol. 14, No. 3, 2020, pp. 482-509.

[40] G. Flamant, Theoretical and Experimental Study of Radiant Heat Transfer in a Solar Fluidized‐Bed Receiver, AIChE Journal, Vol. 28, No. 4, 1982, pp. 529-535.

[41] K. Stahl, J. Griffin, R. Pettit, Optical Properties of Solid Particle Receiver Materials: II. Diffuse Reflectance of Norton Masterbeads® at Elevated Temperatures, Solar Energy Materials, Vol. 14, No. 3-5, 1986, pp. 417-425.

[42] J. Yamada, Y. Kurosaki, Estimation of a Radiative Property of Scattering and Absorbing Media, International Journal of Thermophysics, Vol. 18, No. 2, 1997, pp. 547-556.

[43] A. Sielaff, M. Gowik, C. Völzel, G. Rosengarten, N. Rajic, P. Stephan, Temperature Measurement Using Infrared Thermometry within Semi-Transparent Media, Experimental Heat Transfer, Vol. 32, No. 6, 2019, pp. 545-565.

[44] P. Jones, D. McLeod, D. Dorai-Raj, Correlation of Measured and Computed Radiation Intensity Exiting a Packed Bed, Journal of Heat Transfer, vol. 118, no. 1, Feb. 1996, pp. 94-102.

[45] D. Baillis, J.-F. Sacadura, Directional Spectral Emittance of a Packed Bed: Influence of the Temperature Gradient in the Medium, Journal of Heat Transfer, vol. 124, no. 5, Oct. 2002, pp. 904-911.

[46] R. Lopes, L. M. Moura, D. Baillis, J.-F. o. Sacadura, Directional Spectral Emittance of a Packed Bed: Correlation between Theoretical Prediction and Experimental Data, Journal of Heat Transfer, Vol. 123, No. 2, 2001, pp. 240-248.

[47] A. E. Wald, J. W. Salisbury, Thermal Infrared Directional Emissivity of Powdered Quartz, Journal of Geophysical Research: Solid Earth, Vol. 100, No. B12, 1995, pp. 24665-24675.

[48] D. D. S. Meneses, P. Melin, L. del Campo, O. Rozenbaum, L. Cosson, Probing High Temperature Thermal Emissive Properties of Energy Materials and Coatings with Emission Spectroscopy Augmented by in Situ Reflection, Infrared Physics & Technology, Vol. 108, 2020, Paper 103329.

[49] W. Zhao, Z. Sun, Z. T. Alwahabi, Emissivity and Absorption Function Measurements of Al_2O_3 and SiC Particles at Elevated Temperature for the Utilization in Concentrated Solar Receivers, Solar Energy, Vol. 207, 2020, pp. 183-191.

[50] S. Haussener, W. Lipiński, J. Petrasch, P. Wyss, A. Steinfeld, Tomographic Characterization of a Semitransparent-Particle Packed Bed and Determination of Its Thermal Radiative Properties, Journal of Heat Transfer, Vol. 131, No. 7, 2009, Paper 072701.

[51] B. Singh, M. Kaviany, Independent Theory Versus Direct Simulation of Radiation Heat Transfer in Packed Beds, International Journal of Heat and Mass Transfer, Vol. 34, No. 11, 1991, pp. 2869-2882.

[52] R. Coquard, D. Baillis, Radiative Characteristics of Beds of Spheres Containing an Absorbing and Scattering Medium, Journal of Thermophysics and Heat Transfer, Vol. 19, No. 2, 2005, pp. 226-234.

[53] J. Randrianalisoa, D. Baillis, Radiative Properties of Densely Packed Spheres in Semitransparent Media: A New Geometric Optics Approach, Journal of Quantitative Spectroscopy and Radiative Transfer, Vol. 111, No. 10, 2010, pp. 1372-1388.

[54] J. Randrianalisoa, D. Baillis, Radiative Transfer in Dispersed Media: Comparison between Homogeneous Phase and Multiphase Approaches, Journal of Heat Transfer, Vol. 132, No. 2, 2010, Paper 023405.

[55] J. Petrasch, S. Haussener, W. Lipiński, Discrete Vs. Continuum-Scale Simulation of Radiative Transfer in Semitransparent Two-Phase Media, Journal of Quantitative Spectroscopy and Radiative Transfer, Vol. 112, No. 9, 2011, pp. 1450-1459.

[56] M. Q. Brewster, C. Tien, Radiative Transfer in Packed Fluidized Beds: Dependent Versus Independent Scattering, Journal of Heat Transfer, Vol. 104, No. 4, 1982, pp. 573-579.

[57] Y. Yamada, J. Cartigny, C. Tien, Radiative Transfer with Dependent Scattering by Particles: Part 2—Experimental Investigation, Journal of Heat Transfer, Vol. 108, No. 3, 1986, pp. 614-618.

[58] B. M. Agarwal, M. P. Mengüç, Forward and Inverse Analysis of Single and Multiple Scattering of Collimated Radiation in an Axisymmetric System, International Journal of Heat and Mass Transfer, Vol. 34, No. 3, 1991, pp. 633-647.

[59] K. Kamiuto, M. Iwamoto, T. Nishimura, M. Sato, Albedos and Asymmetry Factors of the Phase Functions for Packed-Sphere Systems, Journal of Quantitative Spectroscopy and Radiative Transfer, Vol. 46, No. 4, 1991, pp. 309-316.

[60] K. Kamiuto, M. Iwamoto, M. Sato, T. Nishimura, Radiation-Extinction Coefficients of Packed-Sphere Systems, Journal of Quantitative Spectroscopy and Radiative Transfer, Vol. 45, No. 2, 1991, pp. 93-96.

[61] T. Hendricks, J. Howell, Absorption/Scattering Coefficients and Scattering Phase Functions in Reticulated Porous Ceramics, Journal of Heat Transfer, Vol. 118, No. 1, 1996, pp. 79-87.

[62] J. Sacadura, D. Baillis, Experimental Characterization of Thermal Radiation Properties of Dispersed Media, International Journal of Thermal Sciences, Vol. 41, No. 7, 2002, pp. 699-707.

[63] K. Ganesan, W. Lipiński, Experimental Determination of Spectral Transmittance of Porous Cerium Dioxide in the Range 900–1700 nm, Journal of Heat Transfer, Vol. 133, No. 10, 2011, Paper 104501.

[64] P. Yang, Q. Cheng, Z. Zhang, Radiative Properties of Ceramic Al_2O_3, AlN and Si_3N_4—II: Modeling, International Journal of Thermophysics, Vol. 38, 2017, Paper 124.

[65] D. Baillis, M. Raynaud, J. Sacadura, Spectral Radiative Properties of Open-Cell Foam Insulation, Journal of Thermophysics and Heat Transfer, Vol. 13, No. 3, 1999, pp. 292-298.

[66] C. Zhao, T. Lu, H. Hodson, Thermal Radiation in Ultralight Metal Foams with Open Cells, International Journal of Heat and Mass Transfer, Vol. 47, Nos. 14-16, 2004, pp. 2927-2939.

[67] L. Dombrovsky, J. Randrianalisoa, D. Baillis, L. Pilon, Use of Mie Theory to Analyze Experimental Data to Identify Infrared Properties of Fused Quartz Containing Bubbles, Applied Optics, Vol. 44, No. 33, 2005, pp. 7021-7031.

[68] Q. Li, B.-J. Lee, Z. M. Zhang, D. W. Allen, Light Scattering of Semitransparent Sintered Polytetrafluoroethylene Films, Journal of Biomedical Optics, Vol. 13, No. 5, 2008, Paper 054064.

[69] P. Yang, C. Chen, Z. M. Zhang, A Dual-Layer Structure with Record-High Solar Reflectance for Daytime Radiative Cooling, Solar Energy, Vol. 169, 2018, pp. 316-324.

[70] S. A. Prahl, M. J. van Gemert, A. J. Welch, Determining the Optical Properties of Turbid Media by Using the Adding–Doubling Method, Applied Optics, Vol. 32, No. 4, 1993, pp. 559-568.

[71] A. N. Bashkatov, E. Genina, V. Kochubey, V. Tuchin, Optical Properties of Human Skin, Subcutaneous and Mucous Tissues in the Wavelength Range from 400 to 2000 nm, Journal of Physics D: Applied Physics, Vol. 38, No. 15, 2005, pp. 2543-2555.

[72] B. Drolen, C. Tien, Independent and Dependent Scattering in Packed-Sphere Systems, Journal of Thermophysics and Heat Transfer, Vol. 1, No. 1, 1987, pp. 63-68.

[73] L. Dombrovsky, D. Baillis, Thermal Radiation in Disperse System: An Engineering Approach, Begell House, New York, 2010.

[74] L. Hespel, S. Mainguy, J.-J. Greffet, Radiative Properties of Scattering and Absorbing Dense Media: Theory and Experimental Study, Journal of Quantitative Spectroscopy and Radiative Transfer, Vol. 77, No. 2, 2003, pp. 193-210.

[75] P. Yang, Z. M. Zhang, Bidirectional Reflection of Semitransparent Polytetrafluoroethylene (PTFE) Sheets on a Silver Film, International Journal of Heat and Mass Transfer, Vol. 148, 2020, Paper 118992.

[76] S. Y. Jeong, C. Chen, D. Ranjan, P. G. Loutzenhiser, Z. M. Zhang, Measurements of Scattering and Absorption Properties of Submillimeter Bauxite and Silica

Particles, Journal of Quantitative Spectroscopy and Radiative Transfer, Vol. 276, 2021, Paper 107923.

[77] W. Lipiński, E. Guillot, G. Olalde, A. Steinfeld, Transmittance Enhancement of Packed-Bed Particulate Media, Experimental Heat Transfer, Vol. 21, No. 1, 2008, pp. 73-82.

[78] K. Jäger, W. Lipiński, H. G. Katzgraber, A. Steinfeld, Determination of Thermal Radiative Properties of Packed-Bed Media Containing a Mixture of Polydispersed Particles, International Journal of Thermal Sciences, Vol. 48, No. 8, 2009, pp. 1510-1516.

[79] P. Coray, W. Lipiński, A. Steinfeld, Experimental and Numerical Determination of Thermal Radiative Properties of Zno Particulate Media, Journal of Heat Transfer, Vol. 132, No. 1, 2010, Paper 012701.

[80] J. Marti, M. Roesle, A. Steinfeld, Experimental Determination of the Radiative Properties of Particle Suspensions for High-Temperature Solar Receiver Applications, Heat Transfer Engineering, Vol. 35, No. 3, 2014, pp. 272-280.

[81] A. Ishimaru, Diffusion of Light in Turbid Material, Applied Optics, Vol. 28, No. 12, 1989, pp. 2210-2215.

[82] A. Schuster, Radiation through a Foggy Atmosphere, The Astrophysical Journal, Vol. 21, 1905, pp. 1.

[83] P. Kubelka, New Contributions to the Optics of Intensely Light-Scattering Materials. Part I, Journal of Optical Society of America, Vol. 38, No. 5, 1948, pp. 448-457.

[84] Q. Li, Light Scattering of Semitransparent Media, Georgia Institute of Technology, 2008,

[85] M. F. Modest, S. Mazumder, Radiative Heat Transfer, 4th ed., Academic Press, Amsterdam, 2021.

[86] H. C. Van de Hulst, Multiple Light Scattering: Tables, Formulas, and Applications, 1st ed., Academic Press, New York, 1980.

[87] S. A. Prahl, Optical-Thermal Response of Laser-Irradiated Tissue, Springer US, Boston, 1995.

[88] Y. S. Yang, J. Howell, D. Klein, Radiative Heat Transfer through a Randomly Packed Bed of Spheres by the Monte Carlo Method, Journal of Heat Transfer, Vol. 105, No. 2, 1983, pp. 325-332.

[89] C. A. Wang, L. X. Ma, J. Y. Tan, L. H. Liu, Study of Radiative Transfer in 1d Densely Packed Bed Layer Containing Absorbing–Scattering Spherical Particles, International Journal of Heat and Mass Transfer, Vol. 102, 2016, pp. 669-678.

[90] S. Kumar, C. Tien, Dependent Absorption and Extinction of Radiation by Small Particles, Journal of Heat Transfer, Vol. 112, No. 1, 1990, pp. 178-185.

[91] L. Pilon, R. Viskanta, Radiation Characteristics of Glass Containing Gas Bubbles, Journal of the American Ceramic Society, Vol. 86, No. 8, 2003, pp. 1313-1320.

[92] L. Ma, F. Wang, C. Wang, C. Wang, J. Tan, Investigation of the Spectral Reflectance and Bidirectional Reflectance Distribution Function of Sea Foam Layer by the Monte Carlo Method, Applied Optics, Vol. 54, No. 33, 2015, pp. 9863-9874.

[93] J. Zhou, Y. Zhang, J. Chen, Numerical Simulation of Laser Irradiation to a Randomly Packed Bimodal Powder Bed, International Journal of Heat and Mass Transfer, Vol. 52, No. 13-14, 2009, pp. 3137-3146.

[94] L. F. González-Portillo, R. Abbas, K. Albrecht, C. Ho, Analysis of Optical Properties in Particle Curtains, Solar Energy, Vol. 213, 2021, pp. 211-224.

[95] C. Chen, C. Yang, D. Ranjan, P. G. Loutzenhiser, Z. M. Zhang, Spectral Radiative Properties of Ceramic Particles for Concentrated Solar Thermal Energy Storage Applications, International Journal of Thermophysics, Vol. 41, 2020, Paper 152.

[96] J. R. Howell, The Monte Carlo Method in Radiative Heat Transfer, Journal of Heat Transfer, Vol. 120, No. 3, 1998, pp. 547-560.

[97] R. Coquard, D. Baillis, Radiative Characteristics of Opaque Spherical Particles Beds: A New Method of Prediction, Journal of Thermophysics and Heat Transfer, Vol. 18, No. 2, 2004, pp. 178-186.

[98] R. Coquard, D. Baillis, Radiative Characteristics of Beds Made of Large Spheres Containing an Absorbing and Scattering Medium, International Journal of Thermal Sciences, Vol. 44, No. 10, 2005, pp. 926-932.

[99] K. Kamiuto, Correlated Radiative Transfer in Packed-Sphere Systems, Journal of Quantitative Spectroscopy and Radiative Transfer, Vol. 43, No. 1, 1990, pp. 39-43.

[100] B. Singh, M. Kaviany, Modelling Radiative Heat Transfer in Packed Beds, International Journal of Heat and Mass Transfer, Vol. 35, No. 6, 1992, pp. 1397-1405.

[101] Q. Brewster, Volume Scattering of Radiation in Packed Beds of Large, Opaque Spheres, J. Heat Transfer, Vol. 126, No. 6, 2004, pp. 1048-1050.

[102] M. Tancrez, J. Taine, Direct Identification of Absorption and Scattering Coefficients and Phase Function of a Porous Medium by a Monte Carlo Technique, International Journal of Heat and Mass Transfer, Vol. 47, No. 2, 2004, pp. 373-383.

[103] B. Zeghondy, E. Iacona, J. Taine, Determination of the Anisotropic Radiative Properties of a Porous Material by Radiative Distribution Function Identification (Rdfi), International Journal of Heat and Mass Transfer, Vol. 49, No. 17-18, 2006, pp. 2810-2819.

[104] M. Zarrouati, F. Enguehard, J. Taine, Radiative Transfer within Strongly Non Homogeneous Porous Media: Application to a Slab of Packed Particles, International Journal of Heat and Mass Transfer, Vol. 91, 2015, pp. 936-947.

[105] W. Lipiński, J. Petrasch, S. Haussener, Application of the Spatial Averaging Theorem to Radiative Heat Transfer in Two-Phase Media, Journal of Quantitative Spectroscopy and Radiative Transfer, Vol. 111, No. 1, 2010, pp. 253-258.

[106] Z. M. Zhang, Nano/Microscale Heat Transfer, 2nd ed., Springer Nature, Switzerland AG, 2020.

[107] Z. Zhang, B. Choi, M. Flik, A. C. Anderson, Infrared Refractive Indices of $LaAlO_3$, $LaGaO_3$, and $NdGaO_3$, Journal of Optical Society of America B, Vol. 11, No. 11, 1994, pp. 2252-2257.

[108] T. J. Bright, J. I. Watjen, Z. Zhang, C. Muratore, A. A. Voevodin, Optical Properties of HfO_2 Thin Films Deposited by Magnetron Sputtering: From the Visible to the Far-Infrared, Thin Solid Films, Vol. 520, No. 22, 2012, pp. 6793-6802.

[109] J. M. Garnett, XII. Colours in Metal Glasses and in Metallic Films, Philosophical Transactions of the Royal Society of London. Series A, Containing Papers of a Mathematical or Physical Character, Vol. 203, No. 359-371, 1904, pp. 385-420.

[110] O. Levy, D. Stroud, Maxwell Garnett Theory for Mixtures of Anisotropic Inclusions: Application to Conducting Polymers, Physical Review B, Vol. 56, No. 13, 1997, pp. 8035-8046.

[111] D. E. Aspnes, J. Theeten, F. Hottier, Investigation of Effective-Medium Models of Microscopic Surface Roughness by Spectroscopic Ellipsometry, Physical Review B, Vol. 20, No. 8, 1979, pp. 3292-3302.

[112] C. Pecharromán, J. Iglesias, Effective Dielectric Properties of Packed Mixtures of Insulator Particles, Physical Review B, Vol. 49, No. 11, 1994, pp. 7137-7147.

[113] D. A. G. Bruggeman, Calculation of Different Physical Constants of Heterogen Substances I Dielectric Constants and Conductibility of Mixtures from Isotrop Substances (English Translation from German), Annalen der Physik, Vol. 416, No. 7, 1935, pp. 636-664.

[114] G. L. Carr, S. Perkowitz, D. B. Tanner, Far-Infrared Properties of Inhomogeneous Materials, Infrared and Millimeter Waves, Vol. 13, 1985, pp. 171-263.

[115] M. V. Bagepalli, J. D. Yarrington, A. J. Schrader, Z. M. Zhang, D. Ranjan, P. G. Loutzenhiser, Measurement of Flow Properties Coupled to Experimental and Numerical Analyses of Dense, Granular Flows for Solar Thermal Energy Storage, Solar Energy, Vol. 207, 2020, pp. 77-90.

[116] J. D. Yarrington, M. V. Bagepalli, G. Pathikonda, A. J. Schrader, Z. M. Zhang, D. Ranjan, P. G. Loutzenhiser, Numerical Analyses of High Temperature Dense, Granular Flows Coupled to High Temperature Flow Property Measurements for Solar Thermal Energy Storage, Solar Energy, Vol. 213, 2021, pp. 350-360.

[117] H. Lee, A. Bryson, Z. Zhang, Measurement and Modeling of the Emittance of Silicon Wafers with Anisotropic Roughness, International Journal of Thermophysics, Vol. 28, No. 3, 2007, pp. 918-933.

[118] Q. Cheng, P. Yang, Z. Zhang, Radiative Properties of Ceramic Al_2O_3, AlN, and Si_3N_4: I. Experiments, International Journal of Thermophysics, Vol. 37, 2016, Paper 62.

[119] V. R. Weidner, J. J. Hsia, Reflection Properties of Pressed Polytetrafluoroethylene Powder, Journal of Optical Society of America, Vol. 71, No. 7, 1981, pp. 856-861.

[120] ASTM G173-03, "Standard Tables for Reference Solar Spectral Irradiances: Direct Normal and Hemispherical on 37° Tilted Surface," 2012.

[121] H. Wang, X. Liu, L. Wang, Z. Zhang, Anisotropic Optical Properties of Silicon Nanowire Arrays Based on the Effective Medium Approximation, International Journal of Thermal Sciences, Vol. 65, 2013, pp. 62-69.

[122] D. D. S. Meneses, M. Balat-Pichelin, O. Rozenbaum, L. Del Campo, P. Echegut, Optical Indices and Transport Scattering Coefficient of Pyrolytic Boron Nitride: A Natural Thermal Barrier Coating for Solar Shields, Journal of Materials Science, Vol. 51, 2016, pp. 4660-4669.

[123] E. D. Palik, Handbook of Optical Constants of Solids, Academic Press, New York, 1998.

[124] D. Wood, Infrared Absorption of Defects in Quartz, Journal of Physics and Chemistry of Solids, Vol. 13, No. 3-4, 1960, pp. 326-336.

[125] J. Glasscock, P. Barnes, I. Plumb, A. Bendavid, P. Martin, Structural, Optical and Electrical Properties of Undoped Polycrystalline Hematite Thin Films Produced Using Filtered Arc Deposition, Thin Solid Films, Vol. 516, No. 8, 2008, pp. 1716-1724.

[126] S. Onari, T. Arai, K. Kudo, Infrared Lattice Vibrations and Dielectric Dispersion in α−Fe_2O_3, Physical Review B, Vol. 16, No. 4, 1977, pp. 1717-1721.

[127] K. Ganesan, J. Randrianalisoa, W. Lipiński, Effect of Morphology on Spectral Radiative Properties of Three-Dimensionally Ordered Macroporous Ceria Packed Bed, Journal of Heat Transfer, Vol. 135, No. 12, 2013, Paper 122701.

[128] H. R. Philipp, Handbook of Optical Constants of Solids, Cambridge, Academic Press, 1998, pp. 749-763.

[129] C. Tan, Optical Interference in Overtones and Combination Bands in α-Quartz, Journal of Physics and Chemistry of Solids, Vol. 64, No. 1, 2003, pp. 121-125.

[130] R. Kitamura, L. Pilon, M. Jonasz, Optical Constants of Silica Glass from Extreme Ultraviolet to Far Infrared at near Room Temperature, Applied Optics, vol. 46, No. 33, Nov. 2007, pp. 8118-8133.

[131] S. Atiganyanun, J. B. Plumley, S. J. Han, K. Hsu, J. Cytrynbaum, T. L. Peng, S. M. Han, S. E. Han, Effective Radiative Cooling by Paint-Format Microsphere-Based Photonic Random Media, ACS Photonics, Vol. 5, No. 4, 2018, pp. 1181-1187.

[132] J. Chen, A. Kumar, J. Coventry, J.-S. Kim, W. Lipiński, Numerical Modelling of Radiative Heat Transfer in a Polydispersion of Ceramic Particles under Direct

High-Flux Solar Irradiation, Journal of Quantitative Spectroscopy and Radiative Transfer, Vol. 278, 2022, Paper 108008.

[133] S. Basu, B. J. Lee, Z. Zhang, Infrared Radiative Properties of Heavily Doped Silicon at Room Temperature, Journal of Heat Transfer, vol. 132, no. 2, Feb. 2010, pp. 023301.

[134] D.-Z. A. Chen, R. Hamam, M. Soljačić, J. D. Joannopoulos, G. Chen, Extraordinary Optical Transmission through Subwavelength Holes in a Polaritonic Silicon Dioxide Film, Applied Physics Letters, Vol. 90, No. 18, 2007, Paper 181921.

[135] H. R. Philipp, Handbook of Optical Constants of Solids, Cambridge, Academic Press, 1998, pp. 719-747.

[136] S. Zeidler, T. Posch, H. Mutschke, Optical Constants of Refractory Oxides at High Temperatures-Mid-Infrared Properties of Corundum, Spinel, and A-Quartz, Potential Carriers of the 13 Mm Feature, Astronomy & Astrophysics, Vol. 553, 2013, pp. A81.

[137] F. Gervais, B. Piriou, Temperature Dependence of Transverse and Longitudinal Optic Modes in the A and B Phases of Quartz, Physical Review B, Vol. 11, No. 10, 1975, pp. 3944-3950.

[138] H. E. Bush, P. G. Loutzenhiser, Solar Electricity Via an Air Brayton Cycle with an Integrated Two-Step Thermochemical Cycle for Heat Storage Based on Fe_2O_3/Fe_3O_4 Redox Reactions: Thermodynamic and Kinetic Analyses, Solar Energy, Vol. 174, 2018, pp. 617-627.